TOWARD A MINIATURIZED WIRELESS FLUORESCENCE-BASED DIAGNOSTIC IMAGING SYSTEM

TOWARD A MINIATURIZED WIRELESS FLUORESCENCE-BASED DIAGNOSTIC IMAGING SYSTEM

By

Moussa Sami Kfouri

Bachelor of Engineering

McMaster University

June 2005

A THESIS
SUBMITTED TO THE SCHOOL OF GRADUATE
STUDIES IN PARTIAL FULFILLMENT OF THE
REQUIREMENTS FOR THE DEGREE OF
MASTER OF APPLIED SCIENCE

McMaster University
Hamilton, Ontario, Canada

MASTER OF APPLIED SCIENCE (2008) McMaster University
(Electrical and Computer Engineering) Hamilton, Ontario

TITLE: Toward a Miniaturized Wireless Fluorescence-Based Diagnostic Imaging System

AUTHOR: Moussa S. Kfouri, B. Eng. (McMaster University)

SUPERVISOR: Prof. M. Jamal Deen

CO-SUPERVISOR: Prof. Qiyin Fang

NUMBER OF PAGES: XII, 122

Abstract

Fluorescence based spectroscopy and imaging techniques provide qualitative and quantitative diagnostic information about biological systems. Some tissue cells have inherent fluorescence characteristics, and when excited with light at a certain frequency, they can emit light of a slightly longer wavelength; a phenomenon known as autofluorescence. Differences in the autofluorescence emission spectra between healthy and diseased tissue may be used as a non-invasive diagnostic tool for the detection of diseases.

In this thesis, I describe the design, fabrication, and testing of a miniaturized fluorescence imaging device for non-invasive clinical diagnosis in the gastrointestinal tract. The device is designed such that it can be turned completely wireless. The system includes three sub-modules: optical imaging, electronics control and image acquisition, and information processing and transmission.

These modules were individually developed and tested before being integrated into a complete, externally powered device. The final integrated system is small in size (diameter: ~ 2.5 cm; length: ~ 11 cm). The performance of each individual module and the overall integrated system has been evaluated using fluorescent phantoms. It has been demonstrated that the miniaturized device can acquire spectrally-resolved fluorescence images. It has also been separately demonstrated that the image stream can be transmitted wirelessly. An important outcome of this feasibility study is the identification of important technological issues and pathways for future prototype development.

Acknowledgments

This section is dedicated to acknowledge the help and support of many individuals who contributed to the success of this work and made this final result possible.

First of all I would like to thank my supervisor, Prof. M. Jamal Deen for giving me the opportunity to work on this interesting project, and for providing me with dedicated support and guidance throughout my two years in graduate school. Prof. Deen's innovative and groundbreaking research has helped me develop my academic research abilities as well as my practical engineering skills. To him I consider myself forever in debt.

I would also like to thank Prof. Qiyin Fang whose expertise in the area of biophotonics and biomedical engineering has contributed greatly to the growth of this thesis. He has always provided me with influential advice and support as well as significant hands-on help in the lab.

I also feel honored to have Prof. Ravi Selvaganapathy and Prof. Mohamed Bakr on my committee. I would like to thank them both for taking the time to review my thesis.

Special thanks to Dr. Ognian Marinov, whom I owe many hours of late night help and support in the lab, as well as plenty of exciting discussions and conversations.

I would also like to express my sincere gratitude towards Mr. Munir El-Desouki, Mr. Waleed Shinwari, and Mr. Hamed Mazhab-Jafari, whom I consider three of the most intelligent students I have ever had the chance to work with. Their friendship, mentoring, and support throughout my graduate studies have only made it easier for me to get through the hard times.

Also, many thanks to my colleagues Dr. Faiçal Saffih, James Mondry, Paul Quevedo, Augusto Ximenes, Fernando Campos, Naser Faramarzpour, Darek Palubiak, Charles Sarkis, Awad Dabbo, Farseem Mohammedy, Mohamed A. Naser, Saman

Asgharan, Mike Kociolek, and Jennifer Russell for their various contributions to this work.

Next, I would like to take this opportunity to thank my dearest friends, Tamim Haroun, Robert Karam, Pardie Hamboyan, Tala Al-Ramahi, Kristy Coleman, Alana Rikabi Sukkari, Maggie Donec, Elias Haddad, Noora Dabbagh, Tareck Abu-Fadel, Ivett Nsair, Youssef Abi-Haidar, Jess LD, Rajiv Kariman, Simon Loane, Silvia Pagoada, Ali Abu-el-Magd, and Adib Ternawly for being very supportive and loyal to me for many years.

Last but not least, I would like to thank my parents, Mr. Sami Kfouri and Mrs. Helene Kfouri, whose unconditional and unlimited love and support have made it possible for me to be where I am now, and my sisters Youmna Kfouri, and Youssra Kfouri Abi-Haidar, whom I look up to, and from whom I get my inspiration to always work hard and aim high. Finally, I thank my youngest sister, May Kfouri, for being the amazing person she is, and I wish her all the luck in her future endeavors.

Table of Contents

List of Figures

List of Tables

Chapter 1

INTRODUCTION

1.1 Motivation and Goals

Gastrointestinal (GI) tract cancer has been found to be one of the most common cases of cancer. As estimated by The National Cancer Institute [1], GI tract cancer makes up to 25% of all cancers, with the majority of these occurring in the colon and rectum (colorectal cancers), and taking the lives of more than 50,000 thousand people in the U.S. and Canada every year. Other types of gastrointestinal (GI) cancer include the esophagus, stomach, small intestine, liver, gallbladder, and pancreas.

Catheter-based video endoscopy, in which a ~2 cm diameter tube containing fiber optic cables carrying visible light is inserted into the gastrointestinal tract of a patient, similar to the one in Figure 1.1 (left) below, is becoming one of the most widely used methods for GI cancer diagnosis and screening. Although catheter-based endoscopy provides useful diagnostic information, it has been documented that the procedure is relatively invasive and costly due to the need of specialized equipments, operating suites, as well as the presence of an endoscopist to administer the procedure [2].

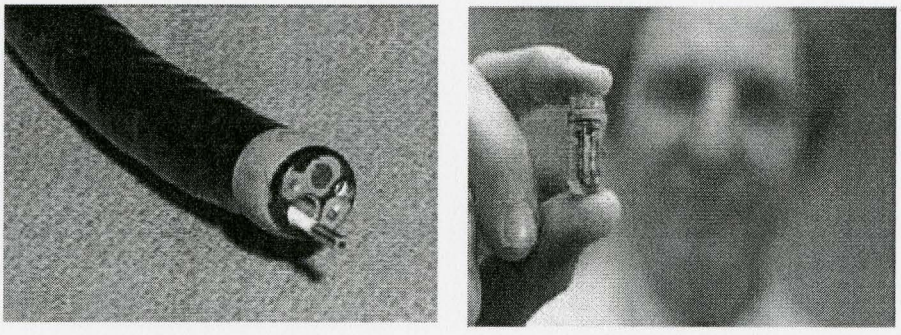

Figure 1.1: A Fiber optic catheter-based system (left) [3] and a capsule-based system (right) [4] used for diagnosis in the GI tract

Alternatives that do not require the use of a catheter have recently been investigated and developed. These techniques use ingestible capsule-size cameras, typically the size of a large vitamin pill, to provide visible illumination and to acquire the reflected/scattered images/video of the GI tract. The most publicized capsule is the PillCam™ (previously marketed as M2A™) capsule by Given Imaging Ltd. [5]. The PillCam™ capsule was developed to challenge push enteroscopy and radiology in diagnosing several diseases such as obscure bleeding, irritable bowel syndrome, Crohn's disease, and chronic diarrhea that are usually found in the GI tract [6].

Typical wireless imaging capsules are about 11 mm (diameter) by 30 mm (length) and contain an optical dome, a short focal length lens, white LED's (light-emitting diodes) for illumination, 2 batteries, a transmitter, an antenna, and a CMOS (complementary metal-oxide-semiconductor) imager. The images are captured over a 7 to 8 hour period inside the GI tract, and are transmitted using ultra high frequency (UHF) band radio-telemetry to aerials attached to the patient's body and stored using a module on the waist belt of the patient. Propelled by peristalsis, the pill travels through the GI tract with no sensation of discomfort, and no air inflation is required [6-8]. The capsule's ability to visualize most of the small bowel mucosa in the small intestine in a convenient and safe manner highlights it as an appealing diagnostic method.

When compared to push enteroscopy, the wireless imaging pill demonstrated 71% superior diagnostic yield [5], and the procedure is non-invasive. However, conventional visible light images are not always sufficient for detecting cancer at early stages [9-11], when treatment is usually more successful. Additionally, a gastroenterologist is required to interpret and evaluate the whole 7-8 hours of video in order to identify potential sites of malignancies, which is lengthy and costly for screening applications.

When biological tissue is illuminated by UV (ultra-violet) light, endogenous tissue fluorescence (also known as autofluorescence) may be observed in the 380 nm - 600 nm range. The observed autofluorescence can be used to distinguish between healthy and cancerous tissues based on the differences in their emission spectroscopic features.

Additional contrast may be achieved by administering exogenous fluorophores prior to tissue-examination [12].

Diagnostic techniques based on fluorescence spectroscopy and imaging have been extensively investigated over the past 20 years. These techniques usually require complex high-sensitivity photodetection systems, as well as novel low-power, highly-integrated electronic systems for control, data processing and communication [13, 14].

Irradiation of the GI tract tissue with ultra-violet light and the detection of emitted fluorescence have been reported to provide better information for earlier detection of cancer [10, 11]. A clinical instrument (LIFE-GI: Light Induced Fluorescence Endoscopy - Gastrointestinal Tract) has been subsequently developed to demonstrate the effectiveness of this approach [15]. This instrument provides real-time video images of tissue autofluorescence using a filtered mercury arc lamp light source, two intensified charge-coupled device (CCD) cameras, a fiber optic endoscope and a computer control console. Conventional color reflectance/scattering images from a broadband visible source (or white light lamp) are also acquired in a different imaging channel. Two camera modes are used (RGB/white light and dual channel fluorescence camera) and the fluorescence images are superimposed on the white light image in pseudo-color. Studies showed that abnormal tissue displayed significant decrease in fluorescence intensity along with an increase in the ratio of red/green fluorescence [16]. Dysplastic or neoplastic areas appear reddish due to a higher red/green ratio [16].

The decrease in auto-fluorescence in pre-invasive tissue is believed to be for three different reasons: a) the decrease in fluorophore amount or quantum yield within the tissue, b) the changes in tissue architecture, and c) the increase in blood volume due to the increase in the micro-vascular density [16]. These quantitative features may enable a "smart" diagnostic method that allows an artificial intelligent system to prescreen the images, which may significantly reduce the diagnosis time required by a gastroenterologist. However, the invasiveness of catheter-based systems requires the design of a non-invasive, more convenient system similar to the PillCam™ capsule that can combine the advantages of both systems (PillCam™ and LIFE) in one device.

In this thesis, the design, implementation, and performance evaluation of a proof-of-concept miniaturized fluorescence imaging system are described, as a first step towards a fully-integrated wireless, non-invasive imaging system for the detection of cancer in the GI tract. Figure 1.2 illustrates the conceptual design we initially had in mind.

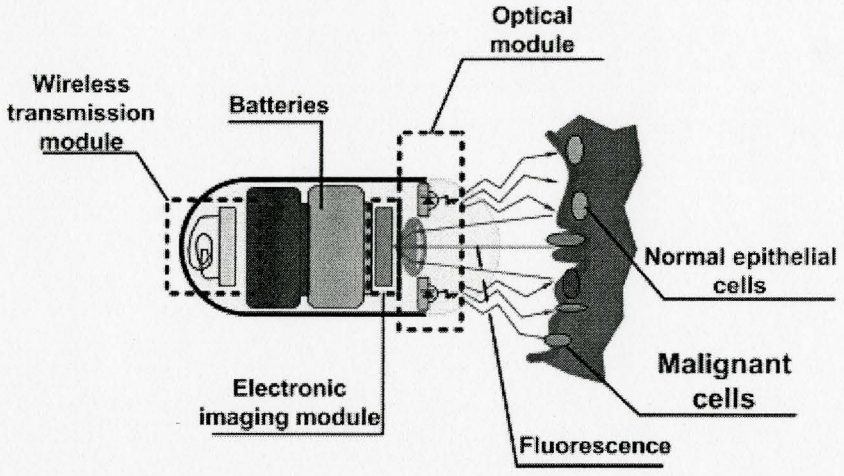

Figure 1.2: Conceptual design of the wireless fluorescence imaging system for non-invasive clinical diagnosis

1.2 GI Cancer Literature Review

The human GI tract (Figure 1.3) [17] that starts from the oral cavity (mouth) is about nine meters long. It consists of four main sections, each having a distinct function. The first section is the esophagus which is specialized for the transfer of food to the rest of the GI tract. Then the stomach follows, and it is specialized for the secretion of digestive material, and the mechanical processing and digestion of food. The small intestine comes afterwards, and its function is to finalize the digestion, and absorb the nutrients. Finally, the processed food goes into the large intestine (colon and rectum), which is specialized for water resorption, lubrication and

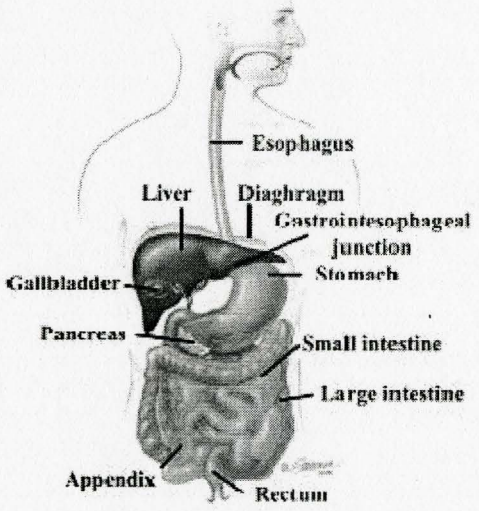

Figure 1.3: The human GI tract [17]

elimination through the anus [17]. Table 1.1 summarizes the types of tumors that can develop in the different parts of the GI tract.

Table 1.1: Different types of GI cancer [17]

Cancer	Types
Esophageal cancer	Squamous cell carcinoma, Adenocarcinoma
Stomach cancer	Adenocarcinoma
Liver cancer	Angiosarcoma, Hepatoblastoma, Cholangiocarcinoma, Hepatocellular carcinoma (hepatoma)
Gallbladder cancer	Adenocarcinoma, Squamous cell carcinoma, Carcinosarcoma, Small cell (oat cell) carcinoma
Pancreatic cancer	Adenocarcinoma, Insulinoma, Gastrinoma, Glucagonoma, Vipoma, Somatostinoma, Acinar cell carcinoma, Cystic tumors, Papillary tumors, Pancreatoblastoma
Colorectal cancer	Adenocarcinoma, Carcinoid tumors, Gastroinstestinal stromal tumors, Lymphomas
Anal cancer	Squamous cell carcinoma, Basal cell carcinoma, elanoma, Adenocarcinoma

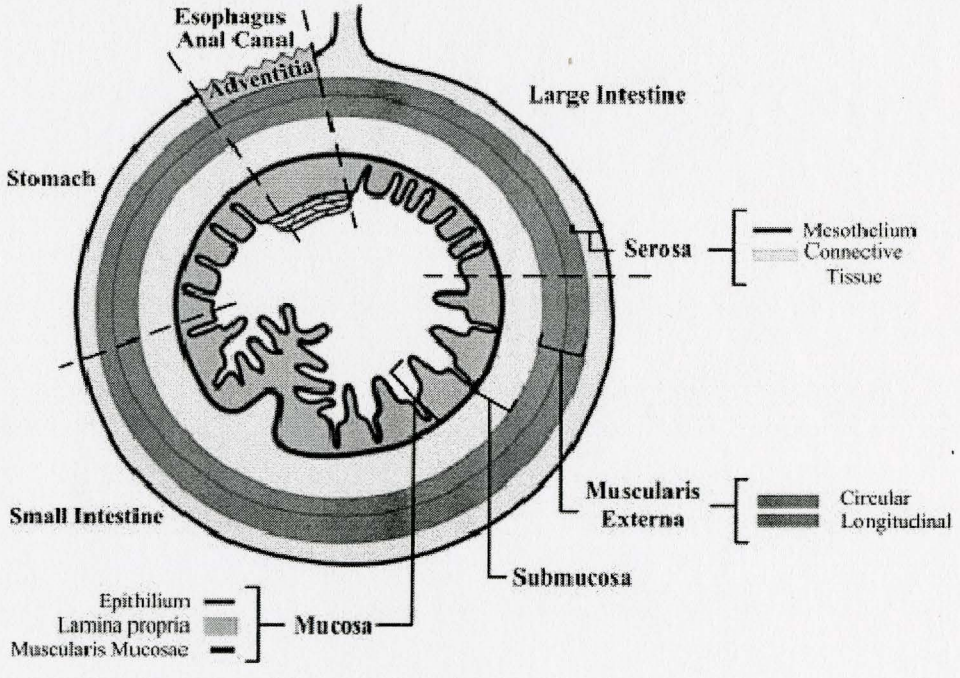

Figure 1.4: The different layers of the GI tract [18]

Tumors can be split into two major categories, benign and malignant. Benign tumors push the surrounding tissue out of their way as they grow, but the tumor does not invade nearby tissue. Malignant tumors on the other hand eat into and damage the normal tissue surrounding them as they increase in size. Therefore, benign tumors can grow quite large without damaging the tissue around them whereas a malignant one starts causing damage as soon as it starts growing. Also, benign tumors do not spread, but malignant tumors do. The rate at which a malignant tumor spreads is different for different tumors, some spread when they are still very small, and some spread later when they are larger in size. Only when the tumor becomes malignant, we call it a cancerous tissue. Benign tumors are not considered cancerous. The number of tumors that can appear and grow in a GI organ is also independent of whether it is benign or malignant [88].

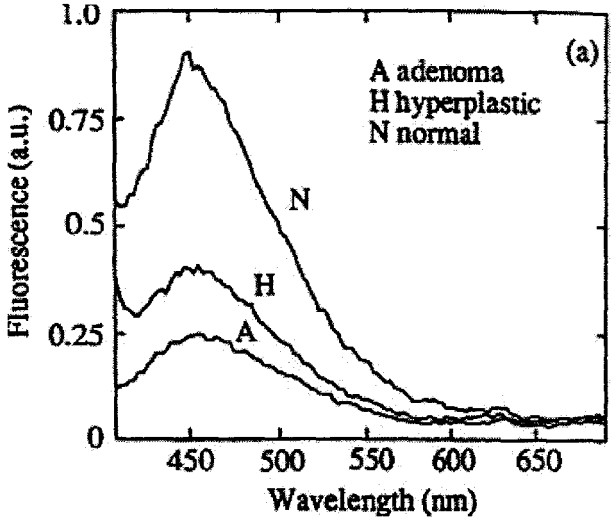

Figure 1.5: The fluorescence spectra of normal mucosa (N), hyperplastic polyps (H), and adenomatous polyps (A) [89]

Figure 1.5 shows the emission spectra of colon tissue, obtained upon excitation at 370 nm [89]. The curves A, H, and N, represent the spectra obtained from healthy mucosa, hyperplastic (benign) polyp, and adenomatous polyp from a typical patient respectively. All curves show a fluorescence peak at 460 nm, and relatively low fluorescence below 400 nm and above 600 nm. The figure shows the typical trend, in

which the peak fluorescence intensity of normal mucosa is generally greater than that of hyperplastic polyps, which in turn is greater than the fluorescence intensity of adenomatous polyps. [89].

To be able to understand how cancer can develop in the GI tract, as well as how it can be detected using optical techniques for minimal invasiveness, it is important to understand the histological structure of the different layers of the digestive tract, and how cancer can develop and spread within these layers. Shown in Figure 1.4 the different layers of the GI tract are presented next [18]. The corresponding thicknesses of these tissue layers are shown in Table 1.2 [90].

Table 1.2: The thicknesses of the different layers of the GI tract [90]

		Normal (n=18)	Hyperplastic (n=4)	Flat Adenoma (n=2)	Adenomatous Polyp (n=26)
Tissue Layer		**Thickness (μm)**	**Thickness (μm)**	**Thickness (μm)**	**Thickness (μm)**
Mucosa	**Superficial epithelia**	61 ± 7	71 ± 22	81 ± 35	106 ± 26
	Subepithelial collagen sheath (SECS)	8 ± 3	90 ± 15	**	**
	Lamina propria	446 ± 2	1,774 ± 180	546 ± 2	2,174 ± 161
Muscularis Mucosa		32 ± 6	28 ± 15	16 ± 7	35 ± 8
Submucosa		5,200 ± 224	5,920 ± 330	6,520 ± 500	5,420 ± 335
Muscularis Propria		7,600 ± 310	5,200 ± 412	6,200 ± 615	6,200 ± 399
Serosa/fat		16,000 ± 4,230	12,400 ± 2	15,400 ± 865	14,400 ± 751

The innermost layer is called the mucosa. It consists of three parts, the epithelial lining, the lamina propria - a loose connective tissue that is vascular and is rich in lymphoid cells, and the muscularis mucosae - a thin smooth muscle layer allowing local movement of the mucosa relative to the surrounding layers. The second layer is the submucosa, which is a moderately dense connective tissue containing larger blood and lymphatic vessels and a network of enteric nerves that controls motility of the mucosa.

The third layer is the muscularis externa, which contains two orthogonal layers of smooth muscle - the inner is oriented circumferentially and the outer longitudinally. A network of enteric nerves between the layers coordinates the contraction needed for peristalsis. The serosa is the outermost layer and consists of an underlying connective tissue. Its smooth wet surface facilitates sliding of organs over one another. Serosa is replaced with adventitia in the esophagus and anal canal [18, 19].

In the esophagus, the mucosa is soft and highly folded, making it suitable for conducting food to the stomach. Lubrication is provided by glands found in the mucosal and submucosal layers, and the muscularis externa is made of skeletal muscle fibres for voluntary swallowing. At the gastroesophageal junction, the epithelial lining changes from stratified squamous to columnar cells as the function changes from simply conducting food to secretion of fluids and digestion of food.

As we go into the stomach, the mucosa is still reasonably smooth and is lined with columnar cells that secrete mucus for protection against highly acidic fluids. The inner lining of the stomach consists of longitudinal folds called rugae that flatten out when the stomach is filled with food. The muscularis externa in the stomach contains three (instead of two) smooth muscle layers that contract sequentially to support mechanical processing. The inner layer is oriented obliquely; the middle layer is continuous with the circular layer of the esophagus; and the outer layer is outer longitudinal and is continuous with the longitudinal layer of the esophagus. The circular layer is thickened at the pyloris to form the pyloric sphincter, controlling entry to the small intestine [18, 19].

The small intestine consists of three separate sections - the duodenum; where the partially digested food enters, the jejunum that makes up most of the central portion of the intestine, and the ileum; whose function is absorption rather than digestion. The surface of the intestine is full of villi; which are projections of the mucosa, and microvilli which are projections of the apical surface of the absorptive cells. These villi and microvilli, are only found in the small intestine. They provide extra surface area for terminal digestion and absorption. They are also covered with simple columnar epithelium lining, and their bases are surrounded by crypts, which extend inwards

towards the muscularis mucosae. The cells of the crypts release antibacterial products and hormones.

In the large intestine, the mucosa also has numerous crypts filled with absorptive cells, but has no villi. Lubrication of condensing fecal material is provided by goblet cells which release mucus. All layers found in the rest of the GI tract are also found in the large intestine. Other functions of the large intestine include absorbing water (90% of the water that goes through it). At the rectal-anal junctions, the simple columnar epithelium lining changes to stratified squamous epithelium [18, 19].

Being the most common type of GI cancer, colorectal cancer arises from adenomatous polyps or adenocarcinoma which is the most common type, and account for 95% of colon cancers. They arise from the glandular cells that line the inside of the colon. Figure 1.6 illustrates how cancer can develop in the innermost layers of the GI tract [91].

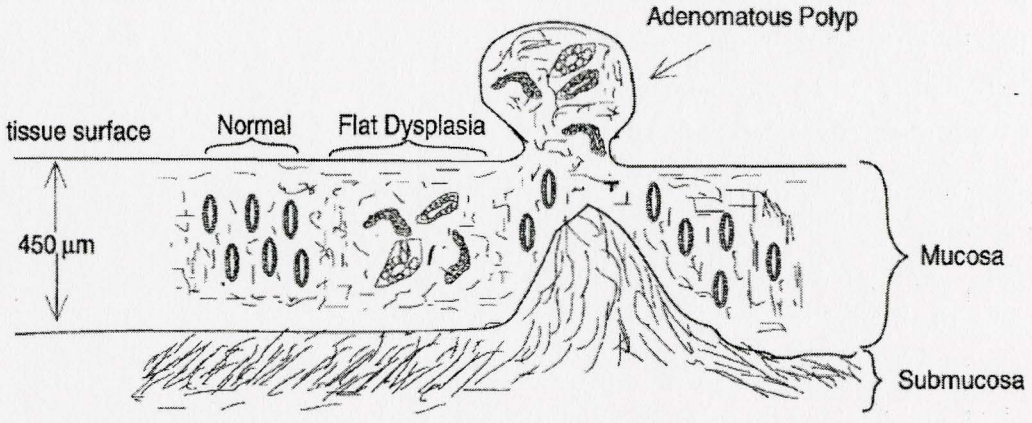

Figure 1.6: Layered structure and principal histological components of normal, dysplastic, and adenomatous colon tissue [91]

A number of genes become activated in a multi-step process to suppress the tumour and repair DNA (deoxyribonucleic acid) and the activation of oncogenes which comes as a result. This gives the colonic epithelial cells a growth advantage and drives the transformation from normal epithelium to adenomatous polyp to invasive colorectal cancer. The inherited type of colorectal cancer is caused mainly by germline mutations, whereas random cancers occur due to an accumulation of somatic genetic mutations. One

of the most common inherited syndromes is the familial adenomatous polyposis coli, which is a single germline mutation in the APC (adenomatosis polyposis coli) tumour suppressor gene. It is characterized by the development of hundreds to thousands of adenomatous polyps in the colon and the development of colorectal cancer and other cancers in the third and fourth decade of life [20].

The cancer first starts when the cells in the colon lining become malignant, and start growing locally and break through the wall into near organs or tissue. In the process, the tumor penetrates and invades the lymphatics or the capillaries locally and gains access to the circulatory system, spreading to further away parts of the body. The deposits that are left in different parts of the body are called metastases. If these metastases are found in distant areas of the body from the colon, then the cancer has spread, and is now known as systemic cancer. The malignancy from which cancer originates can be up to 0.4 inch in size by the time the cancer is detected, and can have over one million cells already, with the size growing twice as fast as the number of cells [20]. This process can take between three and seven years. Thus, like most cancers, the part that is identified clinically is later in the progression than would be desired and screening becomes a very important endeavor to aid in earlier detection of this disease.

As an example, out of every 150,000 Americans diagnosed with colorectal cancer every year, about 50,000 of them die from the disease, making colorectal cancer the fourth most common diagnosed cancer, and the second ranking cancer-related cause of death in the U.S.A [21]. Several risk factors are associated with increasing the chances of developing colon cancer. These risk factors may include factors that cannot be avoided or changed, such as age, or factors that are directly related to the patient's day-to-day habits and environment, such as the person's diet and exercise.

Age is a major risk factor, with people over 50 years old making up to 90% of all colon cancer patients. Another risk factor is dietary habits. Diets high in fat and protein, and low in fiber, are directly linked to increasing the chances of developing colon cancer. This on its own is a risk factor, but may also lead to another risk factor – weight. People who have higher body weight are more susceptible to colon cancer, whether due to

unhealthy diet, or lack of exercise. Studies have also shown that smoking and high alcohol consumption may increase the chance of developing colon cancer [92].

While dietary and exercise factors determine which out of all the people at risk are more likely to develop colon cancer, genetic factors determine which people are at risk. A strong family history in colon cancer or other diseases, especially in the immediate family (parents, siblings, children), makes the person more likely to develop the disease than others. This may be due to certain genetic mutations that can be specific to certain ethnic groups. These genetic changes can cause several conditions, such as familial adenomatous polyposis (FAP), attenuated familial adenomatous polyposis (AFAP) and hereditary non-polyposis colon cancer (HNPCC) [92]. All of these genetic conditions can develop into colon cancer, if left untreated. These conditions are rare and few of the people diagnosed with colon cancer actually have them. There are also certain diseases that can increase your risk of colon cancer, such as ulcerative colitis and Crohn's disease. Despite the fact that there are several 'risk factors' related to the development of colorectal cancer, the exact causes remain unknown. It is thus unknown why colorectal cancer is more common than other types of cancer in the GI tract [92].

Specific trends have also been noticed in regards to colorectal cancer incidents. The most distinguishable of which is that the incidence rate for African-American males is higher than that of white males, and the incidence rate for African-American females is higher than that of white females. However, the incidence rate for males is higher than that of females among both African-American and white citizens [21]. Much research and development has been done in the past 10 years on molecular pathways that govern the growth and differentiation of intestinal epithelial cells and identifying those that grow to initiate and develop a malignancy.

1.3 Fluorescence Imaging

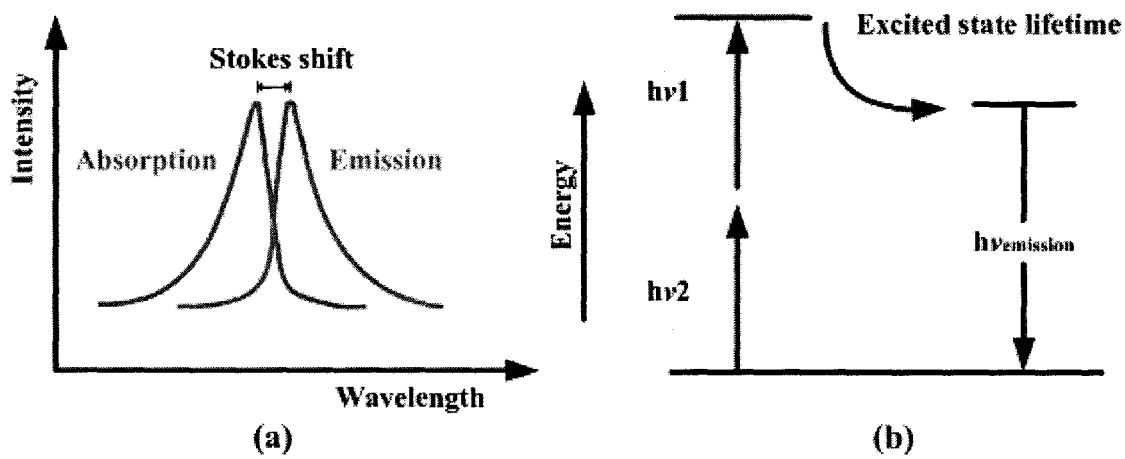

Figure 1.7: (a) Stokes shift [22], and (b) energy levels during fluorescence [23]

Fluorescence happens due to the emission of light from the fluorescing substance almost 10 ns after the substance is excited with light of a certain wavelength. The emitted light has a higher wavelength than that of the excitation light, and changes according to the 'Stokes shift' shown in Figure 1.7(a) [22]. Figure 1.7(b) [23] shows the energy transfer during the excitation and emission processes. It is usually associated with a lifetime τ_f which can also be utilized for cell and molecule analysis. This is a measurement of the rate of decay of the fluorescence emission once the excitation is removed, and it ranges between 1s and 1 ns.

Utilizing the fact that different fluorescing substances or different concentrations of the same fluorescing substance can be different; fluorescence imaging can be used as a non-invasive method to detect and monitor molecular or structural changes in cells with high sensitivity, which is the ratio between the number of patient cases that were successfully diagnosed with the disease by the system, to the total number of cases that have the disease. It is represented by:

$$Sensitivity = \frac{True\_positives}{True\_positives + False\_negatives}, \tag{1.1}$$

and good specificity, which is the ratio between the number of cases that were successfully determined to be healthy, to the total number of cases that are healthy. It is represented by:

$$Specificity = \frac{True\_negatives}{True\_negatives + False\_positives}. \quad (1.2)$$

This opened the path for fluorescence imaging to be used in medical diagnosis. Its non-invasive nature gives it the potential to provide reliable *in vivo* clinical test results, which can have a completely different physiological state than that of *in vitro* samples [24], provided that the most effective wavelengths are utilized. These wavelengths are discussed in the next section.

The biomedical use of fluorescence-based techniques is increasing, and the use of fluorescence endoscopy to detect early carcinomas and to differentiate between normal and neoplastic lesions has recently attracted considerable attention. Photodynamic diagnosis uses fluorescing substances called photosensitizers. Also, one can depend entirely on the inherent fluorescence characteristics of certain tissues; a phenomena known as autofluorescence. Previously hard to detect, autofluorescence has rapidly advanced in the past few years due to advances in developing high power light sources and sensitive imaging devices. Differences in the autofluorescence properties between normal and diseased tissues are believed to be mainly due to the Flavins, Collagen, and NADPH (nicotinamide adenine dinucleotide phosphate-oxidase) found in the tissues [25]. It is also important to mention that tissue autofluorescence properties are excitation wavelength dependent i.e. different wavelengths of light excite different natural fluorophores in the tissue [25]. Thus, early cancer sites can be viewed better under fluorescence imaging since cancerous cells are a few cell layers thick and up to a few millimeters in surface diameter. For example, the sensitivity of systems that use white light to detect early superficial esophageal cancer is only 35%. Also, boundaries of the lesions are often indistinct and nests of tumor cells may be found away from the clearly

visible tumor margin, making the survival rate of patients with advanced stage gastric cancer, for example, only 25% [26].

1.3.1 Tissue Autofluorescence

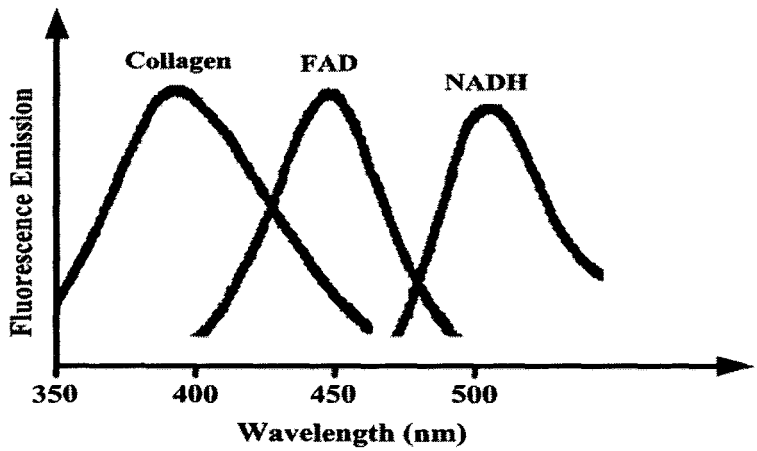

Figure 1.8: Emission spectra of Collagen, FAD (flavin adenine dinucleotide), and NADH [27]

Over the past 2 decades, autofluorescence has been widely investigated as a means for studying the biochemistry of epithelial surfaces for the detection of odd tissue behavior that is not easily detected by conventional white-light imaging. Its advantage is especially highlighted in areas such as Barrett's esophagus and ulcerative colitis where the detection of cancer in the very early stages is very critical due to its high cost and time consumption and significant sampling errors in the conventional biopsy procedures of these areas [27]. Moreover, the need for wide-area imaging methods rather than point-detection techniques in places with large areas such as the GI tract, stresses autofluorescence as an effective approach. It takes advantage of the changes in concentration of inherent fluorophores such as NAD (nicotinamide adenine dinucleotide), flavin, collagen etc. The fluorescence emission spectra of some of these fluorophores are shown in Figure 1.8 [27].

Table 1.3: Optimal excitation and emission wavelengths of fluorophores found in tissue cells [31]

Fluorophore	Origin	Optimal excitation wavelength (nm)	Peak fluorescence emission (nm)
Tryptophan	Protein	280	350
Tyrosine		275	300
Phenylalanine		260	280
Collagen	Connective tissue	330	390
Elastin		360	410
NADH	Respiratory chain	340	450
Flavins		450	520
Porphyrins		400 - 450	635, 690

Most of the autofluorescent species are associated with the structural matrix of tissues (collagen and elastin) or various cellular metabolic pathways (NAD, NADH) [28, 29]. The resulting fluorescence in such compounds is due to the cross linking of amino acids in their structures, which provides the conjugated systems that are generally found in most fluorescent molecules. The resulting fluorescence emission spectrum is very broad due to the various degrees of cross linking that can occur between these species, emitting light in the range 325 nm – 600 nm, and covering various spectral ranges in the ultraviolet and visible regions of the electromagnetic spectrum.

Cells in various disease states have different structures or undergo different rates of metabolism, and therefore, there are often distinct differences in their fluorescent emission spectra [25]. Differences in fluorophore emission generally depend on:

- Fluorophore distribution throughout the tissue
- Local micro-environment
- The tissue architecture being investigated
- Wavelength-dependent light attenuation due to differences in the amount of non-fluorescing chromophores

Therefore, exhaustive studies of the absorption and fluorescence properties of the different biochemical fluorophores give us a better understanding of the complex interactions that may be occurring in tissue samples.

In healthy colonic tissue, fluorescence signals that are measured are mainly correlated with connective tissue fibers in all layers of the bowel wall, and also with cytoplasmic granules between the crypts in the lamina propria of the mucosa. Compared to those from non-healthy tissue cytoplasms in which significant fluorescence emission was measured, fluorescence signals from crypts of normal cells are very faint [25]. In the lamina propria of colonic adenomas, a smaller fluorescence intensity compared to that of normal colon tissue was measured. This decrease is thought to be due to less fluorescent connective tissue fibers in adenomas. It was also found that a larger number of fluorescent eosinphils exist in adenomatous colonic tissue than in normal colon tissue.

When the efficacy of fluorescence spectroscopy was studied quantitatively to be used in classifying colonic tissue as adenoma, adenocarcinoma, or non-neoplastic, it was found that the spectral properties were significantly different in all three different classifications [25]. The optimal excitation wavelength for discrimination between normal and adenomatous colon tissues *in vitro* was determined to be 370 nm, while optimal emission wavelengths due to excitation at that wavelength fell in the range 404 nm – 680 nm [25].

Aside from colonic cancer, and in the case of gastric cancer, the measured fluorescence emission intensities between 395 nm – 440 nm were found to be very different between malignant, premalignant, or normal gastric tissues. Similarly, in the case of oral cancer, it was found that the optimal excitation wavelength for differentiating between normal and dysplastic tissue was 410 nm.

However, distinguishing autofluorescence differences in endoscopic images has been very difficult, as autofluorescence can be very faint to detect [31]. Another problem faced when dealing with tissue autofluorescence is its dependence on tissue optics due to the dependence of the diffusion and absorption processes on the wavelength, as well as its dependence on instrumental parameters, mainly the optical components, which are also highly dependent on the wavelength, both causing distortions to the actual spectra [31].

There are ongoing research efforts to develop and evaluate autofluorescence-based technologies of premalignant and early-stage malignant lesions in many organs, especially the GI tract. The challenge remains to identify optimal excitation and emission wavelengths and to develop spectral analysis methods for interpreting the data that can be obtained using autofluorescence imaging [31]. Figure 1.9 illustrates the principle of autofluorescence imaging [32]. The blue excitation band and the green and red autofluorescence emission wavelength bands that are used to form the autofluorescence image are shown. The spectra of normal and neoplastic GI tissue are superimposed.

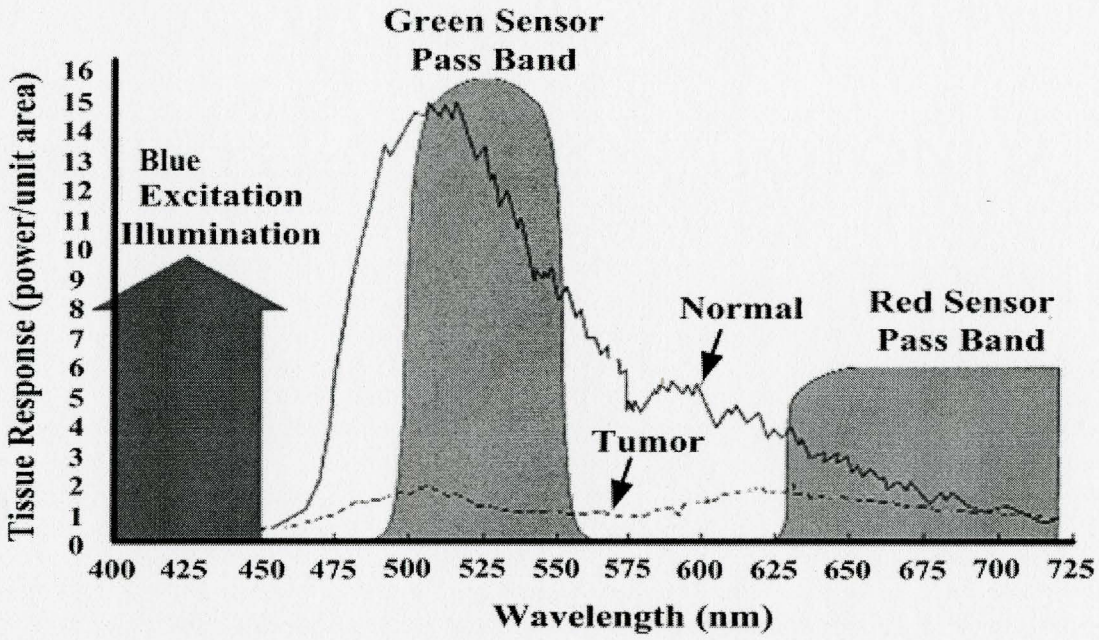

Figure 1.9: Typical fluorescence spectra of normal and neoplastic GI tissue [32]

Several techniques, such as fluorescence spectroscopy, flow cytometry, and cell sorting, have been developed over the years for visual observation of tissue using sophisticated spectroscopic imaging techniques and advanced equipment, driven by the developments in photodynamic therapy of malignant lesions with fluorescent photosensitizers. There are a number of issues to consider when deciding on the effectiveness of one technique as opposed to another. The most important ones that should be considered are the fluorescent molecule, the fluorophore, and marking lesions.

Determining whether the tissue itself has sufficient endogenous fluorescent characteristics or whether it needs external fluorophores is also important, as some fluorophores may have unwanted side-effects.

Also, the change in concentration of the fluorophore (inherent or not), alters the fluorescence of the bulk tissue, and that can be seen as a change in the fluorescence excitation or emission spectra, or in the fluorescence lifetime; but this should not be confused with the differences noticed due to changes in the micro-environment. In addition, the optical properties of the lesion such as absorption and scattering might be different from those of the normal tissue, let alone the differences in the optical geometries [33]. What is left is to extract useful diagnostic information using fluorescence, and that can be done using several methods as mentioned earlier. One can just perform fluorescence imaging at a single excitation wavelength, and a single emission wavelength; but to collect the maximum amount of information, utilizing all the differences in the fluorescence properties is required [33].

The most common observation in measurements involving autofluorescence patterns is a reduction in the emission intensity of a specific wavelength, and an increase in the emission intensity of another. Figure 1.10 shows a reduction in green fluorescence and an increase in red fluorescence with progression towards neoplasia in the esophagus [33]. This is mainly due to low collagen fluorescence and high NADH fluorescence in areas of high-grade dysplasia [33].

One can also perform fluorescence lifetime imaging measurements rather than intensity measurements. This is based on changes in the fluorescence decay characteristics of fluorescent substances. This characteristic makes it useful as an imaging technique in microscope systems.

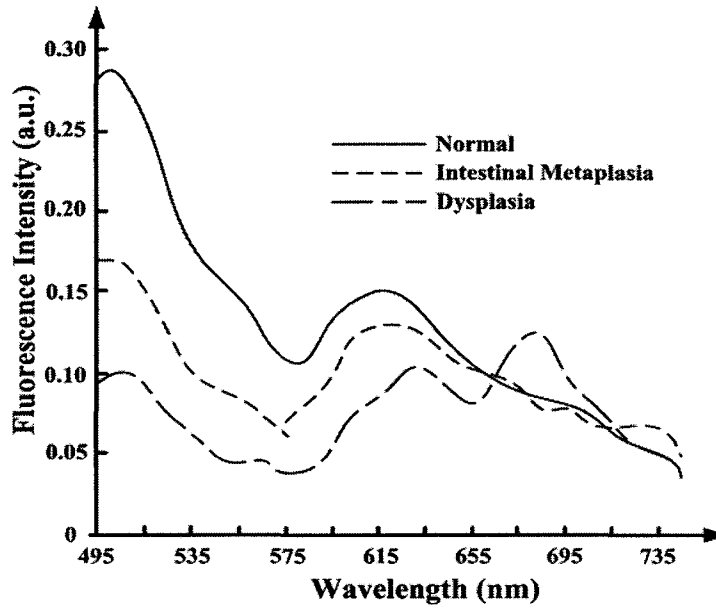

Figure 1.10: Normalized *in vivo* autofluorescence spectra of normal squamous esophagus, Barrett's metaplasia, and Barrett's with high-grade dysplasia. The spectral dip at around 580 nm is attributed to haemoglobin absorption [33].

The fluorophore's time-dependent signal, rather than its intensity, is used to create the image. This has the advantage of minimizing the effect of photon scattering in thick layers of tissue and makes it very useful for biomedical tissue imaging of large tissue depths better than conventional fluorescence imaging.

The simplest way to describe the fluorescence decay of a molecule from its initial value I_0 is given by the following expression,

$$I(t) = I_0 \exp\left(-\frac{t}{\tau_0}\right) + const., \tag{1.3}$$

where t is the total decay time and τ_0 is the fluorescence lifetime. However, it has been shown [34] that the fluorescence decays of collagen, elastin, and other tissue components do not fit a single-exponential decay profile, and that a double-exponential decay can provide a better fit. A more general expression than the equation above is one that can fit several decay constants, τ_i, according to the following equation:

$$I(t) = \sum_{i}^{n} I_i \exp\left(-\frac{t}{\tau_i}\right) + const., \quad n = 1,2,3,..... \tag{1.4}$$

But interactions between different fluorophores can also result in a continuous distribution of fluorescence lifetimes. This is only observable on a molecular scale and cannot be spatially resolved with conventional techniques [35]. In [35], a new approach that considers complex fluorescence decay images was proposed. This approach is best described by the following expression,

$$I(t) = I_0 \exp\left[-\left(\frac{t}{\tau_{kww}}\right)^{\frac{1}{h}}\right] + const., \tag{1.5}$$

where τ_{kww} is the decay constant and h is the heterogeneity parameter. This was triggered by the mathematical observation that the stretched exponential decay can be represented in terms of a continuous distribution of lifetimes [35],

$$I(t) = \int_0^{\infty} \exp\left(-\frac{t}{\tau}\right)\rho(\tau)d\tau, \tag{1.6}$$

1.3.2 Fluorescence Endoscopy

In recent years, the development of powerful, highly sensitive photodetectors, and the increasing capability of microcomputers have improved sensitivity, excitation-emission efficiency and the ability to apply the properties of autofluorescence spectra to biological systems [36]. They have also led to major advances in autofluorescence endoscopic imaging systems for the detection of early carcinomas, and the discrimination between normal and neoplastic lesions.

A typical light-induced fluorescence endoscope for the gastrointestinal tract is composed of a light source (mercury lamp, UV LED...etc.), excitation and emission filters, an excitation detection device, and a computer [37], and produces real-time

pseudo-color images or video images of the scanned tissue. According to a study of 50 patients with Barrett's esophagus [37], fluorescence endoscopy using fiber-optic endoscopes has proved to be almost as ineffective as white-light imaging in the detection of dysplasia or early cancer.

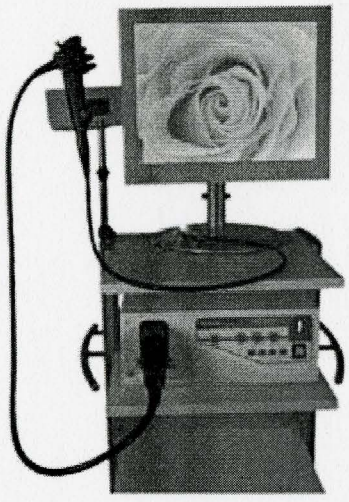

Figure 1.11: A video endoscopy system [38]

The low resolution that fiber bundles offer makes their white-light images inadequate for use, and the awkwardness of their endoscopes due to the size of the detector and associated electronics, make its manipulation inside the GI tract difficult. Therefore videoendoscopy is a big improvement in terms of resolution and portability. Table 1.4 below shows a comparison between fiber-optic endoscopes and video endoscopes [27]. But whether using video endoscopy or fiber-optic endoscopy, single wavelength spectroscopy limits the reliability of the imaging or measurement process, and several approaches have been taken to overcome this limitation, such as using a point-measuring device with spectral resolution into an imaging system, or taking a number of images sequentially under different excitation and emission wavelengths, and superimposing the different images onto each other.

Table 1.4: A comparison of imaging parameters between video and fiber-optic systems for performing autofluorescence imaging [27]

Image parameter	Video	Fiber-Optic
Resolution elements	~ 100, 000	~10, 000
Intensifier	No	Yes
Contrast	Higher	Lower
Registration	Complete	Incomplete
Spectral filtering	Fixed	Flexible

A more advanced approach utilizes combined multiple excitation and emission wavelengths such that the variations in tissue optical properties in the measurements are

compensated for, and thus signals that are merely dependent on specific dye concentrations, rather than structural variations can be obtained [39]. These spectroscopic techniques can be classified mainly into two methods: photodynamic diagnosis using fluorescence drugs called photosensitizers that react to various wavelengths of light, and autofluorescence diagnosis employing inherent tissue autofluorescence, without the use of additional photosensitizers [39].

1.3.3 Why Capsule Endoscopy?

The need for the development of miniature ingestible devices arose from the desire to access areas inside the GI tract that have been deemed difficult to reach using esophagogastroduodenoscopy (EGD), push enteroscopy, and ileonoscopy [40]. The first completely wireless ingestible capsule was approved by the FDA in August 2000, after which a few hundreds of thousands of pills were sold [41]. Not only can these capsules view the entire GI tract, they do so with no pain or sedation, and do not require the inflation of any part of the tract [42], neither do they require a pushing force to propel them through the bowel.

So far, their most successful application is their use in the detection and evaluation of gastrointestinal obscure bleeding. Several studies are also looking into their potential role in the detection of other disorders of the small intestine, even possibly the detection of cancer in its early stages. However, first they have to overcome their main and major risk – the intestinal obstruction of the intestine by the capsule [42, 43].

Another obstacle still hindering the development of such systems is the complexity of determining the position and orientation of the capsule while inside the GI tract, and thus missing important spots of interest [44]. However, despite these major impediments, capsule endoscopy is still believed to become the first-choice examination method in the GI tract, or the small intestine in particular. This, however, would have to be determined upon close and exhaustive evaluation of its added diagnostic value to the healthcare system, taking into account its range of uses, and cost [45].

Enabling these pills to capture fluorescent images, alongside the white light images, can open the door to major advances in detecting lesions in the GI tract. Our

design is a first step towards such a system. Table 1.5 summarizes a few capsule designs that were developed for various types of uses in the human body [8].

Table 1.5: Commercially available capsule-based medical systems [8]

Name of Manufacturer	Technology	Main Technical Specifications	Comparison
Mackay/Jacobson, Nature, 179, 1239-40 (1957)	Endoradiosonde	Battery, single channel (9x28 mm^2)	Temperature or pressure Wireless communication
HC Noiler, Telefunken, Germany (1965)	Heidelberg pH capsule	Battery, single pH sensor (8x20 mm^2)	Small, utilized in medical research
M2A, Given Imaging, Israel (2001)	Video Capsule CMOS camera	Battery, 2 frames/s, 6 hour lifetime (11x26 mm^2)	Video imaging (single channel)
Norika 3, RF System Lab , Japan (2002)	Video Capsule, CCD camera	Induction, 30 frames/s, drug, tracking, sampling (9x23 mm^2)	Video imaging, multiple function, excl. battery
IMP, IMC, KIST Korea (1999-2009)	Endoscopic Microcapsule	Battery, camera, drug release actuator, ultrasound (10x30 mm^2)	Evolutionary. Contract negotiation with GU

1.4 Thesis Organization

A brief review of existing systems is discussed in chapter 2, along with a detailed review of two commercially available diagnostic systems for the GI tract, the catheter-based LIFE (Light Induced Fluorescence Endoscopy) system and Given Imaging's M2A capsule.

Chapter 3 starts off with a general discussion about the design of our prototype on the system-level, then moves into discussing the separate module designs individually.

The choice of optical and electrical components and the circuit and PCB system designs are also outlined. Finally, a brief description of the wireless system is presented.

The experimental set-up is laid out in chapter 4, including the optical set-up and measurement set-up. It also contains all the test and characterization results obtained using the LEDs, the optical filters, and the two main prototypes that were designed, outlining the problem that was faced in the first prototype, and how it was solved in the second prototype. Also, detailed analysis of the images captured by the system is given.

Finally, chapter 5 concludes the thesis with a brief summary of the work that was done and main areas of contribution, areas of improvement, and recommendations for future research plans.

Chapter 2

BACKGROUND

2.1 Available Systems

In this section, the two systems briefly described in the introduction are explained in detail; these are the catheter-based light induced fluorescence endoscopy (LIFE) system, and the capsule based system by Given Imaging Ltd., the PillCam™.

2.1.1 Light Induced Fluorescence Endoscopy – The 'LIFE' System

In 1996, the design of a nitrogen dye laser system for measuring tissue autofluorescence in the GI tract was reported [46]. At the time, it had recently been found that tissue autofluorescence properties are wavelength dependent. This inspired researchers to incorporate a stepper motor for wavelength selection. A gated intensified detector was used for detection, and a fiber optic bundle was used to carry the excitation light and collected emission light. The system was connected to a computer for data acquisition and analysis [46].

This was one of the very first attempts to measure GI tissue autofluorescence *in vivo*. Different excitation wavelengths between 420 nm and 460 nm with 10 nm steps were used for excitation. The tests were simultaneously carried out on healthy colonic tissue and a tubular adenoma (mild dysplasia). All wavelengths showed a decrease in green fluorescence in the pre-cancerous lesions, and the excitations at 420 nm and 430 nm wavelengths showed a second peak at 635 nm, a peak that was not seen in the normal tissue, and was interpreted as extra emission due to the presence of excess porphyrin [46]. It was also shown that in areas of abnormal tissue, there was a decrease in fluorescence intensity, and an increase in the red/green fluorescence ratio. These results were observed

in tests that were carried out on several areas in the GI tract, including the esophagus (see Figure 2.1 (A)) and the colon (see Figure 2.1 (B)).

The system was later modified to include intensified CCD cameras, in an attempt to capture real-time video images under three different modes: Conventional white light imaging, light-induced fluorescence (LIF) imaging of two bands (green and red), and

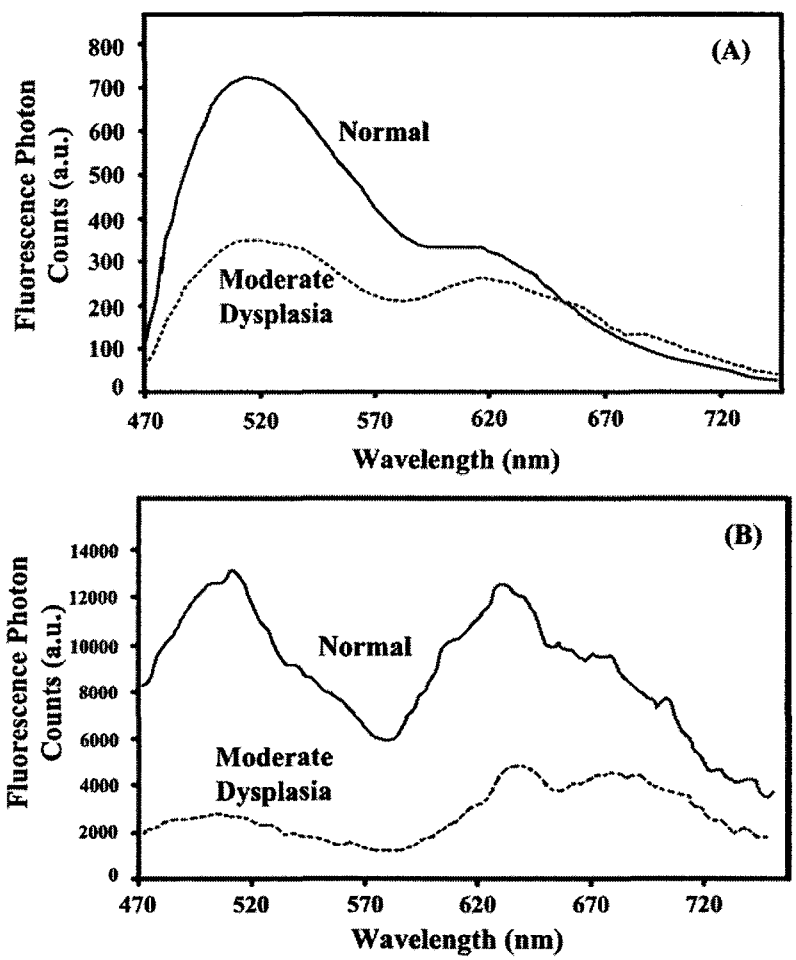

Figure 2.1: The decrease in fluorescence intensity as observed in (A) the esophagus and (B) the colon [16]

light induced fluorescence and reflectance (LIFR) imaging based on combining a green fluorescence image and a red reflectance image. For illumination, a 100 W small arc mercury lamp was used, and wavelength selection was implemented by switching between different band-pass filters. Figure 2.2 shows a schematic representation of the

system [47]. The fluorescence or reflected light is collected by the fiber bundle and an image is formed and converted into a video signal using a camera that outputs standard RGB (red, green, blue) signals. Since only the change in autofluorescence emission was being studied, and not changes due to non-uniform fluorescence collection off curved surfaces, the presence of a reference signal was necessary to serve as a reference signal, hence the use of a red fluorescence signal in LIF. However, since the red fluorescence signal is still significantly affected by the geometrical features of the tissue, the normalization it provides is not enough. In the LIFR system, a reflectance signal is used instead of the fluorescence signal, which does not change when moving between normal tissue and abnormal tissue [47]. This modification resulted in improved signal-to-noise ratio and image contrast.

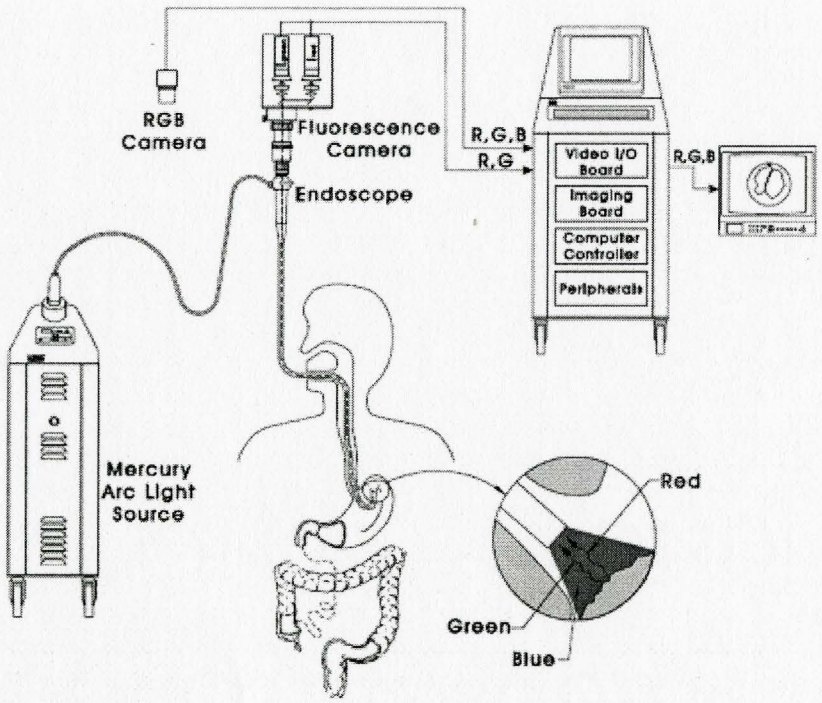

Figure 2.2: The endoscopic fluorescence imaging system for the GI cancer detection, showing the illumination, image acquisition, computer control, and display consoles [47]

Figure 2.3 shows the green and red signal profiles across the lesion and some of its peripheral normal tissue on both the LIF and LIFR images [16]. Figures 2.3 (a) and (b)

correspond to a plot of the green and red intensities measured using the LIF system, and a plot of their ratios respectively, while Figures 2.3 (c) 2.3 (d) correspond to a plot of the green and red intensities measured using the LIFR system, and a plot of their ratios respectively. As can be seen in the figures, in both cases, there was an increase in the green to red ratio, however, the increase in the LIF images was only two times whereas the same ration in the LIFR was over three times. Moreover, both LIFR plots demonstrate its advantage over LIF in terms of signal-to-noise ratio. These experiments proved that fluorescence imaging can provide similar biopsy information as white light imaging, but with much higher sensitivity [16].

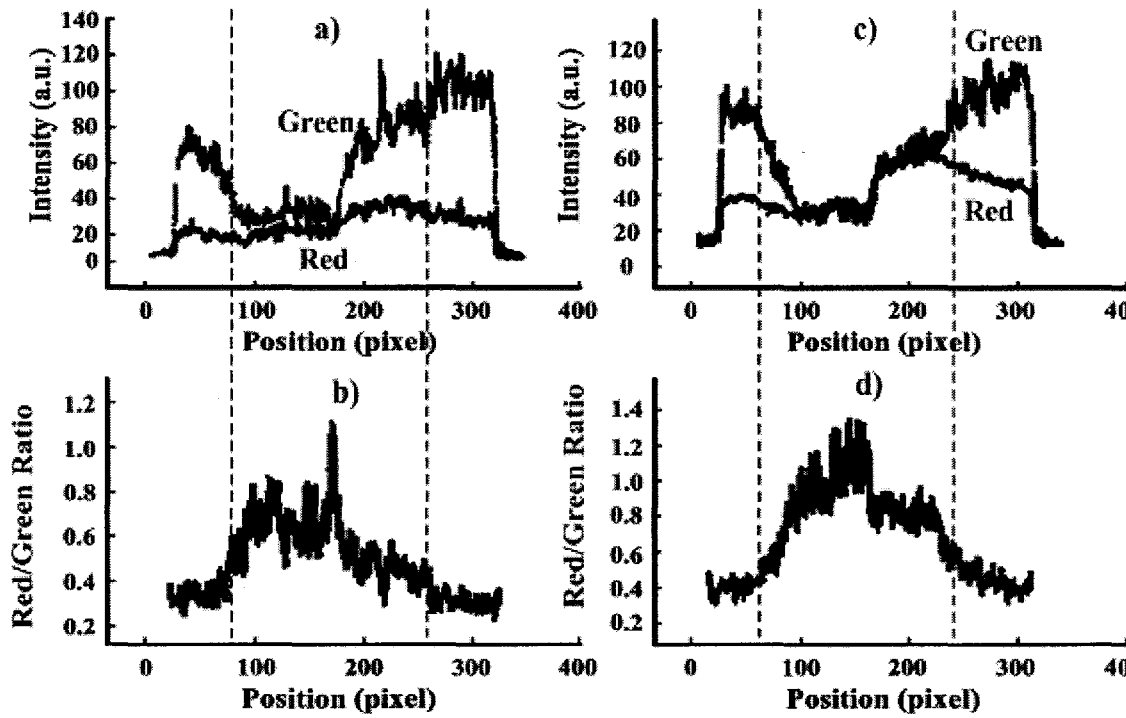

Figure 2.3: (a) A plot of the green and red intensities measured using the LIF system, and (b) a plot of their ratios respectively. (c) plot of the green and red intensities measured using the LIFR system, and (d) a plot of their ratios respectively [16]

A study also showed that the main source of fluorescence is the presence of submucosal collagen, and therefore the effect on the submucosal by the thickened mucosa in abnormal tissue causes the reduced fluorescence [29]. Also, it was concluded that the LIFE imaging system possesses the following capabilities: 1) differentiate

between hyperplastic and adenomatous polyps of the same size; 2) detect flat adenomas; 3) delineate the boundary of Barrett's esophagus; and 4) enable detection of dysplastic lesions in a Barrett's field [48]. Other similar systems have been studied and one such system is the AFI system. This video-scope system uses two CCD imagers, one for white light imaging and another for autofluorescence detection. The thickness of the video-scope is about 13.8 mm, and has variable stiffness [49]. Three excitation wavelengths were used in this video-scope system - red, green, and blue. The autofluorescence image and the reflected green and red images are captured with the RGB system, and the three images are used to form a pseudo-color image, with the autofluorescence signals being displayed as green, the green reflected signal as red, and the red reflected signal as blue. When images were taken using the system, normal tissue were found to provide pinkish images, while adenoma and cancerous tissue provide reddish-blue images, and inflammation provides blue images. The system is depicted in Figure 2.4 [49].

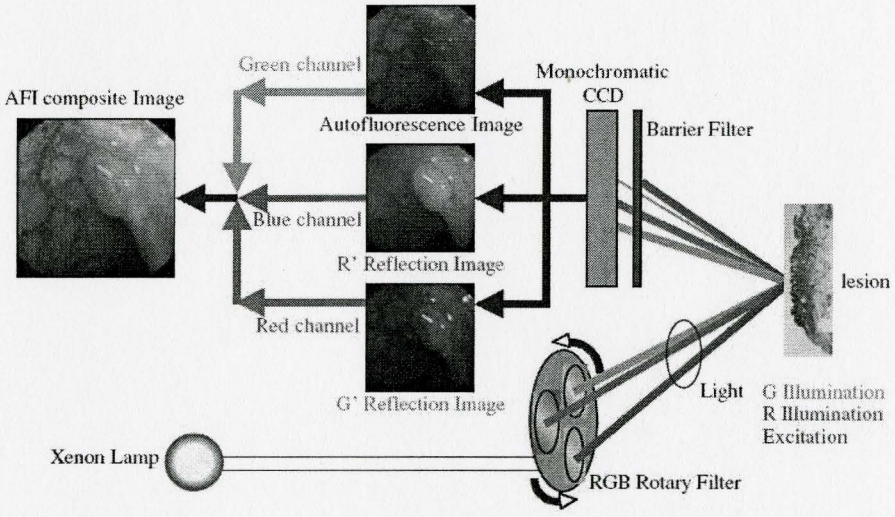

Figure 2.4: The AFI videoscope system [49]

Similar to the LIFE-GI system, the AFI system was able to distinguish between hyperplasia and adenoma (different color tones). Also, the sensitivities were comparable between LIFE-GI and AFI systems (87% and 89% respectively), however, AFI showed

higher specificity (81% compared to 71%). This showed that the AFI system is capable of differentiating between different colonic tumors, and of detecting small lesions without magnification. It also showed improved brightness and image clarity compared to LIFE-GI [49].

2.1.2 Wireless Capsule Endoscopy – The PillCam™ System

The idea of sending a capsule down the throat through the GI tract first emerged in the early 1990s by a mechanical engineer, Dr. Iddan, who had worked and participated in projects with different medical imaging companies and groups. In the meantime, breakthrough advances were being achieved by Dr. Paul Swain on wireless endoscopes, designed for more or less the same purpose. In 1998, Given Imaging Ltd. was established to produce the world's first ingestible wireless imaging capsule. Swain joined Given Imaging Ltd. in an attempt to unify the efforts and bring both teams' advances together. By the year 2000, successful trials on animals had been confirmed [50].

Later on in the year 2000, images of the human small bowel were being taken and transmitted wirelessly to the outside of the body. The capsule was 11 mm x 30 mm, and used a short focal length lens, and a transparent optical window, and propelled down the intestines by peristalsis without any air inflation [52]. The success of the capsule was believed to be due to a number of achievements, especially the advances in CMOS imaging devices which were already producing images comparable in quality to those of charge-coupled devices, but with much less power consumption. Moreover, advances in application specific integrated circuits made the integration of small transceivers into the capsule possible, transmitting signals with high enough output power. Light emitting diodes (LEDs) were also available for use as efficient, low power illumination sources [52].

By August 2001, the capsule received the FDA approval to be used at major medical centers throughout the United States and Europe [53]. Figure 2.5 shows the PillCam™ system with all its different parts. At a rate of 2 images per second, and sending over 50,000 images over a period of 8 hours, the capsule is capable of detecting objects as small 0.1 mm, magnifying them at a ratio of 1:8, with a 1-30 mm depth of view

[54]. The images are sent using UHF-band radio telemetry to sensor's wrapped around the patient's abdomen and stored on a recorder strapped to a belt around the patient's waist. The first GI problem that the PillCam™ tried to detect was obscure gastrointestinal bleeding, proving itself superior to push enteroscopy, yielding 50-67% detection rate compared to push enteroscopy's 25-30% rate [55-58]. The results are illustrated in Figure 2.6.

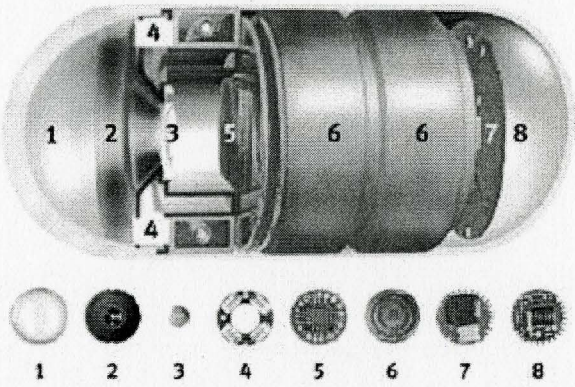

Figure 2.5: The PillCam™ system [51]

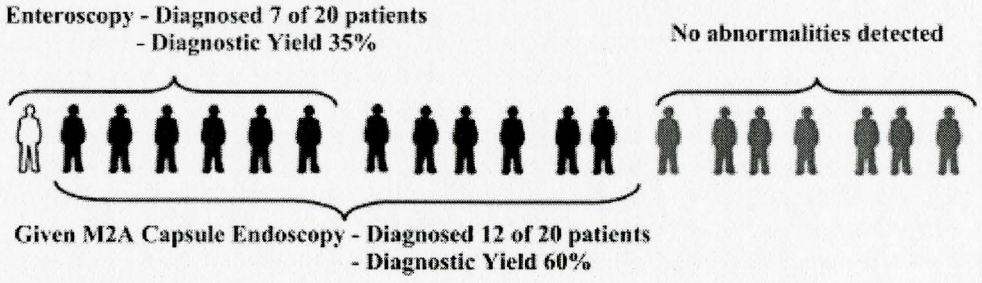

Figure 2.6: Detection rate of two rival diagnosis methods; enteroscopy, and capsule endoscopy [53]

The pill also demonstrated its effectiveness in detecting Crohn's disease, with a detection rate ranging between 43% and 71%, as compared to entero CT's 30% [58-60]. In a pilot study of the colon capsule (PillCam), the sensitivity of the capsule ranged between 56% and 76%, depending on the mode of capsule analysis, and the specificity ranged between 69% and 100%. These numbers excluded non-functioning capsules. A

large pilot trial of colon capsule endoscopy in three centers (n = 91) was conducted: compared with colonoscopy, and depending on the mode of capsule analysis (primary or adjudicated readings), the sensitivity ranged between 56% and 76% and the specificity between 69% and 100% (nonfunctioning capsules were excluded from the analysis [n = 7]) [93].

The main obstacle that the capsule faced, though, was a few cases of capsule retention or non-natural excretion (NNE), and this happened more often with people with diagnosed cases of Crohn's disease and ischemic bowel disease. However, NNE required surgery in only 1% of all patients, which would have been needed anyway to operate on the disease or abnormality detected. In cases where excessive bleeding occurs, the blood may obscure the source of bleeding, so detecting it would be difficult. Also, some extremely small lesions may be missed since the capsule is constantly moving, taking only 2 frames per second but reviewed by the endoscopist at a rate of 20 frames per second [54].

Another system made by a Japanese team called NORIKA, emerged as they were trying to come up with a design of a camera that can monitor inner body changes of astronauts. Their capsule uses a micro-capsule CCD camera, and measures 9 mm x 23 mm. Much of the pill is covered with a white plastic cover, except for the part that encloses the camera, which is transparent. The main advantage that the NORIKA system has over its rival PillCam™ is that it uses a coil-embedded transmitter vest for power transmission, and therefore it does not operate on batteries, making room for other parts. The DSP chip is also left outside the body, reducing much of the pill's power requirements. Capsule rotation was also implemented in the pill, using 3-pole motor theory with strobe light technology. A table comparing the PillCam™ system and Norika's capsule is shown below [62].

Table 2.1: A comparison between the PillCam™ and the system made by Norika [62]

	PillCam™	Norika
Dimension	11 mm x 26 mm	9 mm x 23 mm
Application	CMOS	CCD
Power Source	Battery	Wireless Power Transition
Frames/s	2 fps	30 fps
Lifetime	6 hours	-
Position Control	No	Yes
Position Detection Inside GI	Yes	No

2.2 Illumination Issues

Figure 2.7 shows the emission spectra of normal, hyperplastic, dysplastic, and adenocarcinoma colon tissue [90]. Figure 2.7(a) shows the spectra that were obtained using focused illumination, and collection through surrounding fibers. Figure 2.7(b) shows the spectra that were obtained using wide-beam illumination.

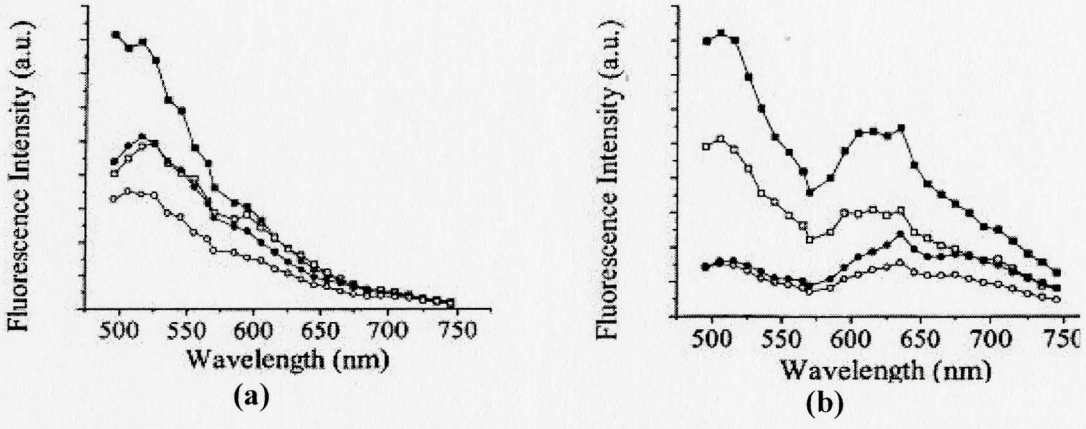

Figure 2.7: The effect of blood absorption on measured *in vivo* autofluorescence spectra (with 442 nm excitation). Spectra corresponding to human colon normal (■), hyperplastic (□), dysplastic (●), and adenocarcinoma (○) tissues were measured in a) point geometry (central delivery and surrounding collection fibers in contact with the tissue surface; and in b) imaging geometry (with wide field illumination of the tissue surface and the spectral measurement made at a central point) [90]

In the case of wide-beam illumination, the detected fluorescence signal has greater contribution from tissues at greater depth than with focused illumination. This is due to the excitation light falling onto the tissue at different incident angles, therefore

reaching multiple depths inside the tissue. The impact of angle of illumination on the collected signal is discussed later in this section. The dips in the spectra in Figure 2.7(b) are due to differential light absorption by submucosal blood vessels. The absence of these dips in Figure 2.7(a) is due to the lack of shallow depth sampling with focused illumination [90]. Moreover, focused illumination is usually used for *in vitro* diagnosis, or in cases in which the location of the diseased tissue is known. However, in the case of capsule endoscopy in which the diseased tissue is yet to be detected, the capsule needs to scan large areas looking for the abnormality. Focused illumination in this case is time consuming and does not provide information on the relative location of the malignancy.

The illumination-collection geometry is considered to have a strong influence on the spatial origin of the detected fluorescence signal; however, devices that implement this idea are not very well understood. Monte Carlo simulations were performed [94] to determine the effect of angled geometry on the spatial origin and intensity of the detected fluorescence. In general, the results showed that the detection of the fluorescence signal can be increased significantly using oblique incidence geometries, and probe fluorophores at depths up to 0.5 mm. This increased detection capability is thought to be due to the overlap of the illumination and collection cones within the tissue, and more importantly, the position of the overlap and its depth within the tissue. In the study, they used variable illumination and collection angles (with respect to normal incidence), and only general light-tissue interactions were investigated, irrespective of the device or optics used.

A homogenous tissue of (5 x 5 x 4) was used for the simulations, and two optical property cases were considered (low attenuating tissue and high attenuating tissue), taking into account the different absorption and scattering coefficients at the two attenuation levels. In Figure 2.8, we see that the normal incidence case (a), fluorescence originating from a range of depths is collected, but when either of the angles is changed (b), the cone overlap volume is limited to a small area close to the surface. As shown in Figure 2.8(c), the incidence and collection angles are measured relative to the normal incidence angle (the line perpendicular to the surface of the tissue) [94].

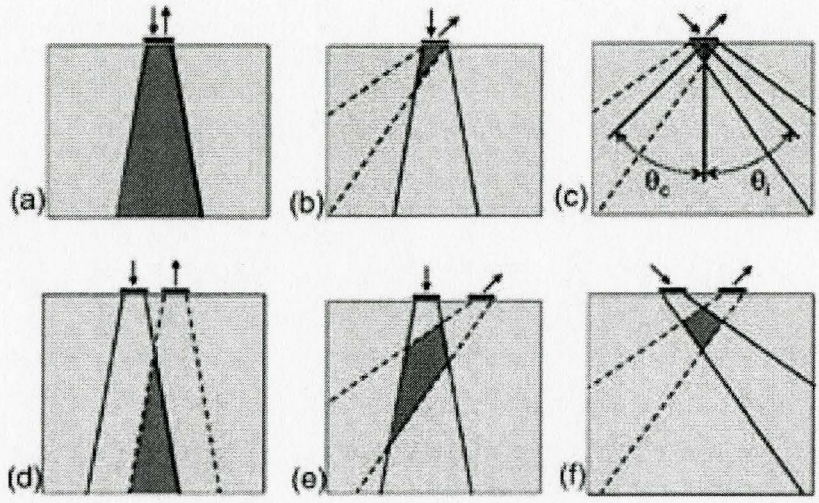

Figure 2.8: The overlap between the excitation and emission rays inside the tissue, at different incident/collection angles, and different distances between the excitation and emission rays [94]

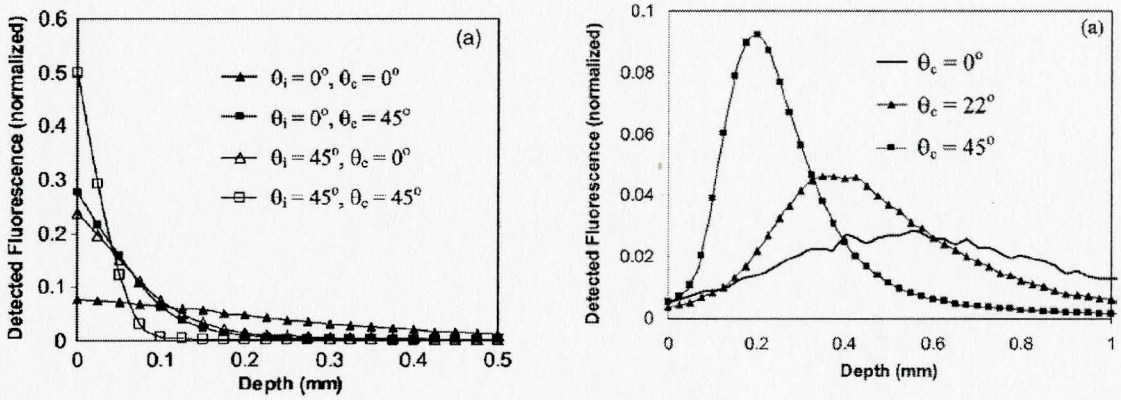

(a) (b)

Figure 2.9: The impact of changing (a) the angles of illumination-collection, and (b) the separation distance between the illumination-collection beams [94]

In Figure 2.9(a), the curves show that changing the incident and collection angles increases the sensitivity in the regions in the top 50-100 μm. Also, it was shown that changing the collection angle has a slightly better effect than changing the incidence angle, which was interpreted as having increased sensitivity at the most superficial regions, and a decreased sensitivity in the deeper regions. This is possibly due to differences in optical properties at the excitation and emission wavelengths. Changing the

separation distance between the incident and collection spots may also vary the size and location of the overlap cone (Figures 2.8(d), (e), (f)). Figure 2.9(b) shows how changing the collection angle impacts the detected fluorescence signal, when the separation between the two beams is 0.1 mm, and the angle of excitation is fixed at 0 degrees [94].

In the general case, as the wavelength of the excitation light increases, so does the penetration depth within the tissue. Therefore, optimal excitation wavelengths may vary between one site and another or one site may have multiple optimal excitation wavelengths. This wavelength dependence arises from the dependence of the penetration depth on the scattering and absorption of the examined tissue [90]. For wavelengths below 600 nm, penetration depth is only hundreds of micrometers up to a few millimeters [95]. In our case, and with an excitation light of 365 – 370 nm, the penetration depth is only 400 μm [91]. Therefore, only the mucosa layer of the colon tissue is investigated. Several other factors can control the penetration depth of the light, such as the carrying collection and illumination beam angles. Bigger angles result in shallower overlaps between the two beams, and therefore giving more information about the more superficial parts of the tissue. The distance between the beams is another factor. Also, varying the numerical aperture ($n\sin\theta$), where n is the refraction index.

On the other hand, the collected spectrum is also distorted by the absorption and scattering properties of the tissue. For example, two different samples with the same intrinsic type and amount of intrinsic fluorophores can give a different spectrum and intensity due to the presence of different amounts of blood. Several techniques have been developed to correct for the correct for the real tissue fluorescence, but the choice of technique depends on the type of measurements being made, and the type of tissue being investigated. It also depends on whether the information being sought on the fluorophore concentrations is relative or absolute. Additionally, the choice also depends on the accuracy of the technique of excitation and emission spectra, and the measurement system itself [96].

2.3 Localization

Despite the current capsules' ability to reach places in the GI tract that conventional endoscopes cannot, it still takes a long time to go through the whole tract, giving no accurate information on its location or orientation at any specific time, and therefore the location of the spots that are found by the capsule cannot be found easily. This problem highlighted the necessity for an actuation and guidance system. The PillCam™ group eventually incorporated a localization module based on a number of antennas placed outside the body, and receiving RF signals from the pill, with the closest antenna at a specific time receiving the strongest signal. The sensors are placed in an ordered manner at specific places around the abdomen, and the detected RF signal levels are compared and an estimate of the capsule's location is made accordingly. The same system that is used to transfer the images is used, and therefore no extra parts are needed [63, 64].

Another proposed method by Given Imaging Ltd., calculates the motility of the pill based on comparing the intensity of a number of successive images or elements of these images, to determine the proximity of the pill to a place of interest. Below is a more detailed description of this method, as described in a patent (# 6,944,316) by Given Imaging Ltd.

In their algorithm, each image P_i is compared to its predecessor image P_{i-1} or some other previous image P_{i-n} to determine the motility of the capsule during the time between the capture of the two images by comparing the similarity of the two images i.e. the more similar two images are, the slower the motility of the capsule, and therefore the smaller the distance traveled in the given time. For instance, if there are no differences between the images, it can be assumed that the capsule did not move at all, whereas if the there are no similarities between the images, it can be assumed that the capsule was moving too fast in the given time.

The images can be compared on a pixel-by-pixel basis, or the images can be divided into several clusters of pixels, and the clusters are compared in turn. For example, a 256 x 256 image can be divided into 1024 clusters of 32 x 32 pixels and then compared.

The resulting motility can either be a number that is relative to specific positions in the GI tract, or an absolute value can be determined. The images are recorded by the capsule and transmitted to the data processor storage unit. Then two successive, but not necessarily adjacent images are compared. The images can be divided into pixel clusters, sections or cells. Taking the 256 x 256 pixel example mentioned before, the images are divided into 1024 clusters $A_i(m,n)$ where m = 32 and n = 32. Then the data processor calculates the average intensity (e.g brightness) $I_{Ai(m,n)}$ for each cluster $A_i(m,n)$ in the two images. The intensity value of a cluster is the average of the brightness values for the pixels in the cluster. A matrix of the intensities of the clusters may be formed for each image. Then the processor determines the value $D_i(m,n)$ which is an absolute number representing the difference between the average intensities of two corresponding clusters from the two images. The value $D_i(m,n)$ can be represented by the following:

$$D_i(m,n) = \left| I_{A_i(m,n)} - I_{A_{i+x}(m,n)} \right| \tag{2.1}$$

A matrix of the absolute values of the differences between all clusters is produced. Afterwards, the average difference between the two images *Diff* is calculated. This can be done using the following formula:

$$Diff = \sum_{m=1,32;n=1,32} \frac{D_i(m,n)}{1024}. \tag{2.2}$$

The number obtained is between 0 and some value U which is an upper limit determined by the input parameters. If this number is low, it indicates that the measured number (e.g brightness) varied little between the two captured frames (low motility), and a large value indicates that the measured value varied significantly (high motility). Then we will have a series of values for every two corresponding frames in the two images. These values can be normalized or decimated to an arbitrary scale. For example, each difference value in the range 0 - U can be normalized (linearly or non-linearly) to a number in the range 0 - 10. The normalized values can later be used to plot a graph of the

relative motility versus time. Specific conditions in the graph, such as indications of low motility, can be labeled using for example different colors or line patterns.

Methods that do not involve image analysis include the use of an accelerometer to determine the instantaneous acceleration of the capsule as it moves through the GI tract, and then this acceleration information can be integrated to find velocity information which can later be used to determine the location of the capsule. Also, a pressure sensor can be attached to the capsule to measure the difference in pressure caused by the peristaltic waves at different times, and a relationship between the pressure and the velocity at which the capsule can move under a specific pressure can be determined, which allows for the calculation of the velocity at different pressure values.

Another group [65] proposed another method that makes use of a magnet that can be enclosed inside the pill. The magnetic permeability of the human body has non-ferromagnetic properties and therefore, has little effect on static magnetic fields. Placing a permanent magnet inside the capsule creates a magnetic field, which would have a specific intensity and direction at different measurement locations. A number of sensors are placed outside the body and determine the magnet's location and orientation by the data measured by these sensors. The mathematical modeling and algorithms are beyond the scope of this chapter, but the method showed superiority over the RF method used by the PillCam™ [65].

Table 2.2 shows the results as obtained by the measurements carried out by the group that came up with the magnetic method [64]. When compared with the RF method, it showed considerable superiority, with some measurements showing average localization and orientation errors as low as 4.6 mm and 4.5% respectively when 16 sensors and 3-axis are used, as opposed to the RF method's 37.7 mm average localization error [65].

Table 2.2: The magnetic method compared to the RF method [64]

	1-axis	2-axis	3-axis
5 sensors	42.7mm; 17.9 %	16.8mm; 16.6%	9.1mm; 8.2%
9 sensors	26.4mm; 27.1%	10.8mm; 9.3%	6.4mm; 6.0%
16 sensors	14.2mm; 15.8%	6.6mm; 5.8%	4.6mm; 4.5%

Chapter 3

SYSTEM DESIGN

In this chapter, the design procedure of the fluorescence imaging prototype is described. The system consists of three separate sub-systems: an optical imaging module, an electronic image acquisition module, and an image processing and wireless communications module, as shown in Figure 3.1. The optical imaging module provides illumination and collection of fluorescence light over the desired spectral wavelength range. The electronics image acquisition module acquires the image using a high-sensitivity charge-coupled device-based (CCD) imager and provides signal conditioning. The wireless transmission module provides data sampling and compression, and then transmits the data using an RF transmitter. Details of the design and implementation of each module are discussed respectively in the sub-sections below including their requirements for power supply.

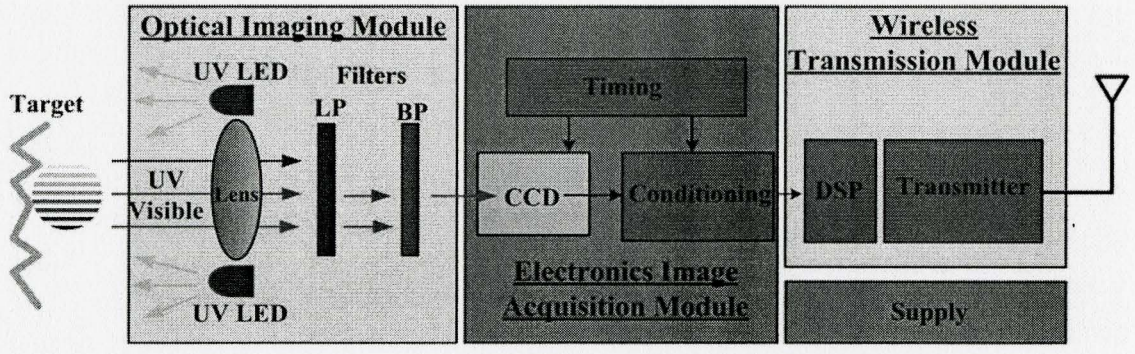

Figure 3.1: Sub-systems of the wireless fluorescence-based diagnostic imaging system

3.1 Design Specifications and Key Considerations

The general design specifications and considerations are discussed below. Firstly, the optimum excitation wavelength for GI tissue is around 365 nm (as mentioned earlier in Chapter 1). This requires a light source that has a peak emission wavelength at 365 nm, with a narrow emission spectral bandwidth. The wavelengths of interest are in the 400 nm – 550 nm range. Therefore the image acquisition module must have high sensitivity in this wavelength. Moreover, enough excitation power should be exposed to the tissue in order to obtain detectable fluorescence signals, while not exceeding the photo-bleaching limit of the cells which is about 10 mW/cm^2.

One of the main objectives of this work is to demonstrate the ability to detect fluorescence signals, and therefore a high sensitivity imager has to be used. Absolute fluorescence intensity yields from human GI tissue were not found, but similar yields from bronchial tissue showed that around 5 pW/μWxnm can be obtained [97]. Table 3.1 shows typical yields at the emission maximum of human bronchial tissue [97]. This shows that imagers that can detect fluorescence signals in the range of a few pico-watts per micro-watt of excitation power per nano-meter of spectral width are needed. If we consider an emission bandwidth of 200 nm (400–600 nm), then we expect a total emission power of 1 nW per 1 μW of excitation power.

Table 3.1:Fluorescence yields from human bronchial tissue[97]

Excitation Wavelength (nm)	Maximum Emission Wavelength (nm)	Fluorescence Yields at the Emission Maximum (pW/μW x nm)
350	460	7.9
365	460	6.9
380	475	4.7
395	480	4.5
405	490	4.2
420	500	4.5
435	515	4.0
450	520	3.5
465	530	3.1
480	550	3.5
495	575	2.3

For wireless transmission of the images, methods of image processing and compression have to be considered. Several license–free bands are allocated for short-range personal communication networks. These are the 902-928 MHz ISM band in North America, and the 433 MHz and 868 MHz ISM bands in Europe [66]. In general, the transmission frequency cannot exceed 1 GHz, otherwise most of the radiation energy is be absorbed by the human body tissue [67]. Table 3.2 summarizes the key system specifications that should be taken into consideration when designing a fluorescence imaging system.

Table 3.2: Key considerations for fluorescence imaging prototypes

Key Considerations	
Size	Typical: 11 mm x 25mm. Keep minimal.
Power Consumption	Minimal
Imager Choice	CCD or CMOS?
Frame Rate	30 frames/second
Optical Intensity	$< 10\ mW/cm^2$
Transmission Frequency	< 1GHz

3.2 The Optical Imaging Module

The optical imaging system was designed to maximize the amount of fluorescence light that reaches the imager at the desired spectral wavelength band.

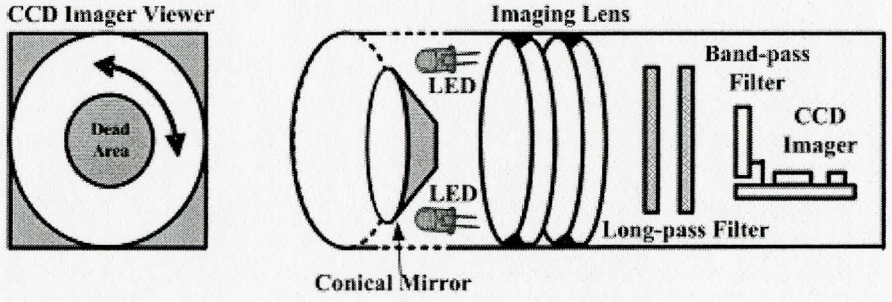

Figure 3.2: Schematic of the optical set-up used. The filters, lenses, LED's and conical mirror are shown in the diagram

The schematic of the optical module that was used in all our tests is shown in Figure 3.2. In this figure, we can see the different parts used, and the way they were placed relative to each other. These parts include (from right to left) the long wavelength pass filters, achromatic lenses, the LEDs and the conical mirror. A set of eight light emitting diodes (LED) arranged in a circle in front of the imaging lenses were used for illumination. Four ultra-violet (UV–365 nm) LEDs were used for fluorescence excitation and the other four were white-light LEDs used for conventional white-light illumination. The illumination light is reflected from a customized conical mirror (shown in Figure 3.3) and projected onto the side wall of the gastrointestinal tract. Auto-fluorescence emission from the tissue is collected by the same mirror and two achromatic imaging lenses and then projected onto a high sensitivity CCD imager. Light perpendicular to the conical surface is reflected off the mirror and through the lenses, which focus a spatially distorted image onto the CCD imager.

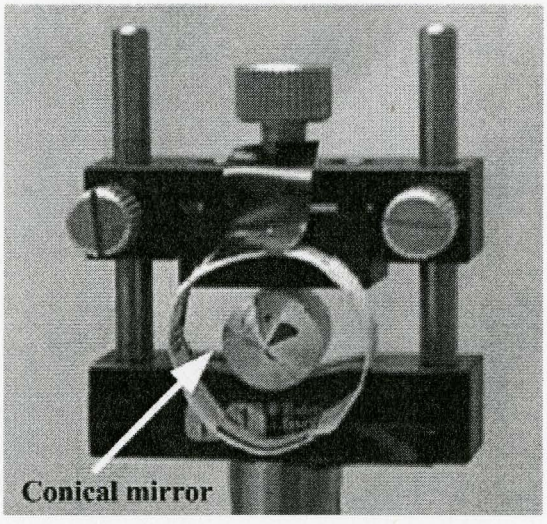

Figure 3.3: The conical mirror used, as seen in the set-up

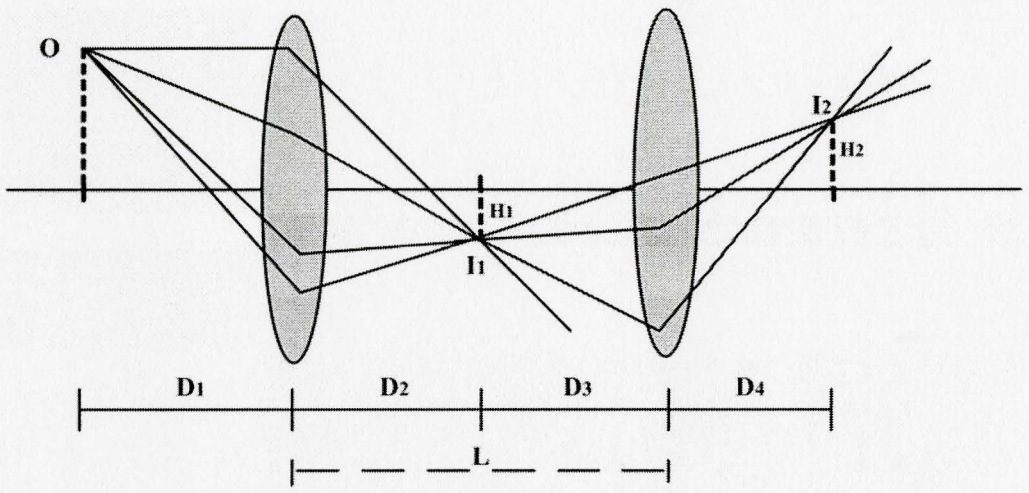

Figure 3.4: Concept of a two-lens system

The advantage of using two lenses is that we get more degrees of freedom to control the aberrations that may arise from the use of only one lens. Aberrations happen due to the lens material having different refractive indexes for different wavelengths, thus focusing the same part of an image over a bigger area. Using two lenses allows for using two different materials that, when combined, can reduce the effect of the aberrations.

Figure 3.4 illustrates the concept of using a two-lens system for focusing the light on the CCD surface. If O is the object being imaged, and L is the distance between the two lenses, then the distance D_2 between the first lens and the first image I_1 can be found using the following:

$$\frac{1}{f_1} = \frac{1}{D_1} + \frac{1}{D_2}, \tag{3.1}$$

where f_1 is the focal length of the first lens. This image is seen by the second lens as an object, and it is in turn imaged behind the second lens at a distance D_4 from the lens, which can be found by using the following:

$$\frac{1}{f_2} = \frac{1}{D_3} + \frac{1}{D_4}, \tag{3.2}$$

where f_2 is the focal length of the second lens. Also, the magnification of the image due to both lenses can be found using:

$$M = \frac{D_2}{D_1}\frac{D_4}{D_3}. \tag{3.3}$$

A 0-2 mm variable diameter aperture was inserted between the two lenses to control the depth-of-field (DOF), which is the amount of distance between the nearest and farthest objects that appear to be in focus. The DOF depends on the object's distance from the lens, the focal length of the lens, and the lens's aperture (or *f*-number). If the aperture is kept constant, increasing the magnification by moving the object closer to the lens or using a lens of greater focal length decreases the DOF. On the other hand, decreasing magnification increases the DOF. Similarly, increasing the aperture size decreases the DOF, and decreasing the aperture size increases DOF. Since the light being autofluoresced is of very weak intensity, it is most likely that a larger aperture will have to be used to allow for enough light to pass through. This might come at the cost of a reduced depth-of-field and image blurring.

One of the design challenges was to find adequate aspherical lenses that can be used once the system undergoes miniaturization. Obtaining customized lenses of such a small diameter may not be financially feasible and hence a switch to regular spherical lenses was required. This adds to any blurring and distortion of the image. Reconstructing the image is the next task in the optics section. Initially, the unwrapping of the image was done on Adobe Photoshop using the Polar to Rectangular Distortion Filter. This filter essentially reads the image as if it were plotted on a polar graph then re-plots each pixel onto a cartesian plane. This was later programmed on Matlab so that it can be done in near real-time.

A 3/1 object-to-image focal length ratio was required to reduce the image to the size of the CCD. Keeping this ratio in mind, the task becomes choosing two lenses with focal lengths that optimize the depth-of-field while remaining relatively short in separation distance. If the focal lengths of the lenses are too short, it is not possible to focus a large radius of the image in one frame, thus reducing the usable image and

leading to possible data loss. If the lenses are too far apart, then they can focus more of the image in a given frame; however the size of the imaging head becomes impractical. The current system uses focal lengths of 60 mm for the object lens and 20 mm for the image lens.

A long wavelength pass filter (WB380, Optima Inc, Tokyo, Japan) is used to block the scattered excitation light from reaching the CCD imager. The spectral bandwidth of the long wavelength pass filter is shown in Figure 3.5. The filter blocks about 80% of all radiation below 380 nm. Table 3.3 is a close-up at the transmittance of the filter around the range at which the LEDs emit UV light looking closely around the range at which the LEDs emit light (365 nm ± 10 nm). At around 360 nm, the transmittance of the filter is only 1.224%, but it jumps up to 22.22% and 53.09% at 370 nm and 380 nm respectively. However, the CCD imager that we chose also has a spectral response that falls below 50% for all radiation below 380 nm. This further ensures that only the fluorescence light is captured by the imager, and only a very minimum amount of UV light is also detected. If LEDs of a wider spectral range were used, this filter would have to be changed.

Table 3.3: Transmittance of the WB380 nm filter around the LED emission wavelength

Wavelength (nm)	310	320	330	**340**	**350**	**360**	**370**	**380**	390	400
Transmittance (%)	0.026	0.024	0.024	**0.026**	**0.026**	**1.224**	**22.220**	**53.090**	71.010	79.660

It is also important to mention that the filter not only blocks the excitation light, but it also modulates the emission signals as well, especially in the range 370 nm – 400 nm. This is not a major problem since the emission signals that we are interested in are well into the 400 nm to 600 nm range. The transmittance of the filter at these wavelengths is shown in Table 3.4.

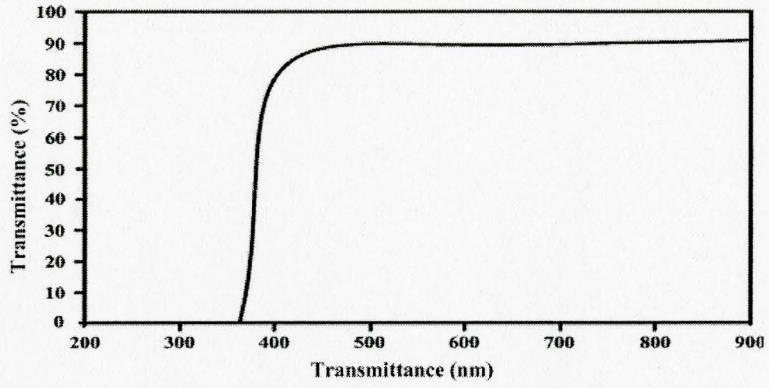

Figure 3.5: Long-pass filter – blocks out 80% of radiation below 380 nm

Table 3.4: Transmittance of the WB380 nm filter in the range of fluorescence emission

Wavelength (nm)	410	420	430	440	450	460	470	480	490	500
Transmittance (%)	83.7	85.9	87.2	87.9	88.5	88.8	89.1	89.3	89.5	89.7
Wavelength (nm)	510	520	530	540	550	560	570	580	590	600
Transmittance (%)	89.8	89.8	89.9	90.1	90.2	90.2	90.3	90.4	90.4	90.4

Spectral selection of the fluorescence light is achieved using a narrow bandwidth band-pass filter at the desired wavelength. The intensity of the excitation light is typically three to four orders of magnitude higher than the emitted fluorescence light. Therefore, one of the main design considerations is to minimize the scattered excitation light from reaching the CCD. This is achieved by positioning both filters as close to the CCD imager as possible, and using low UV transmission glass for the imaging lenses.

A set of low power white-light LEDs with luminous intensity of up to 980 (± 100) mcd were used for conventional video endoscopy (NOTE: 1000 mcd = 1cd = the light intensity of a "standard" candle viewed from a distance of 12 inches. This intensity is approximately equal to the light produced by a small 2 watt standard incandescent bulb). For UV excitation, two types of LEDs were evaluated as fluorescence excitation sources.

1) High power UV LEDs with peak wavelength of 365 (± 5) nm, and optical output power of up to 100 (± 10) mW at 500 mA input current. Their properties are shown in Table 3.5.

2) Low power UV LEDs with the same peak wavelength and optical output power of 2 (± 0.2) mW at 20 mA input current. Their properties are shown in Table 3.6.

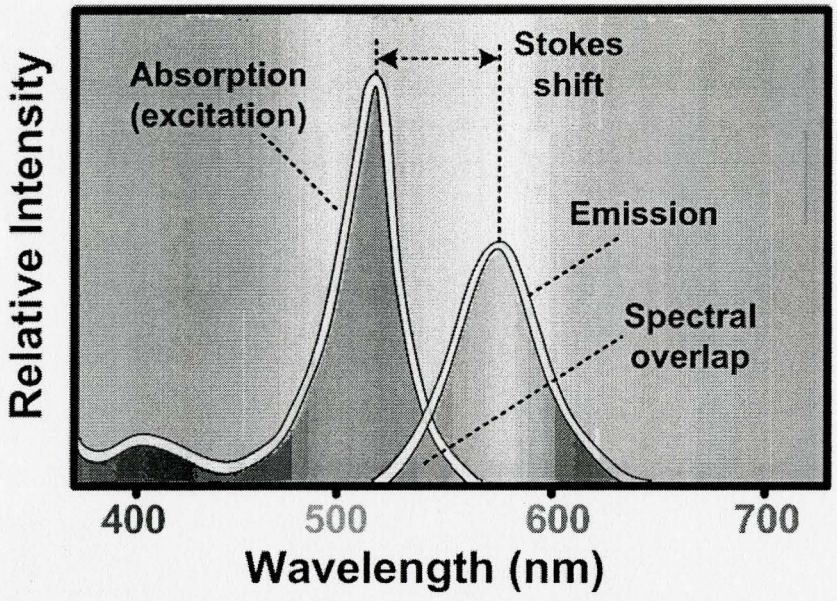

Figure 3.6: Comparison between the excitation and emission spectra and intensities [68]

Table 3.5: Properties of the high-power UV LEDs

	Absolute maximum rating	Unit
Forward Current	700	mA
Pulse Forward Current	1000	mA
Allowable Reverse Current	85	mA
Power Dissipation	3300	mW

Table 3.6: Properties of the low-power UV LEDs

	Absolute maximum rating	Unit
Forward Current	25	mA
Pulse Forward Current	85	mA
Allowable Reverse Current	80	mA
Power Dissipation	100	mW

In the initial tests, the high-power LEDs' power consumption was found to be too high for a wireless device and they also caused excessive heating of the device, thus

prohibiting its use in clinical environments. The low-power LEDs were found to be able to provide sufficient UV excitation to induce fluorescence in our tests while maintaining manageable levels of power consumption as well as heat generation. They were therefore chosen for use in the prototype system where all following tests were performed. Lower intensity illumination, however, results in lower emission intensity, which in turn leads to reduced signal-to-noise levels in the acquired fluorescence images. The white-light LEDs were used to provide white-light images that can be used to help determine the position of the detected abnormality. The fluorescent images can be superimposed over the white-light images, and pseudo-images can later be created for viewing.

3.3 The Electronic Image Acquisition Module

An imaging acquisition module was designed and optimized for high-sensitivity detection. The size of the module and its power consumption were kept as small as possible using off-the-shelf commercial components. A diagonal ¼ inch interline black-and-white CCD image sensor (ICX228AL, Sony, Tokyo, Japan) for EIA monochromatic video cameras was used.

The choice of using a black and white imager rather than a color one was made based on the general requirements on which an application of this type is dependent – high resolution and precise contrast recognition. Color imagers simply focus on isolating color bands, and do not acquire contrast as well as black and white cameras [69]. Moreover, color imagers produce a lot more data that needs to be processed, possibly adding to the size of the imager and its power consumption [69].

In addition to the imager, a 48-pin timing controller (CXD2463R, Sony, Tokyo, Japan), was used to provide the clocking signals for the imager's vertical and horizontal registers. Clocking the timing controller was achieved using a 28.6363 MHz oscillator, and a dip switch was used to change the electronic shutter speed. All the components were mounted on a 2 cm by 8 cm two-layer printed circuit board (PCB) (shown later in this chapter 3). The CCD imager was placed at a 90° angle from the board, pointing forward towards the optical module.

A schematic representation of the signal flow between the CCD imager and the timing controller is shown in Figure 3.7. The timing controller provides all the timing control signals to the CCD imager, including the vertical and horizontal register signals. It also provides the synchronization signal that needs to be added to the output video signal of the CCD that only provides the video signal without any synchronization signal used by the image acquisition modules. It was first necessary to invert the signal, because the signal produced by the imager is the inverse of a standard video signal. Then using a summing amplifier configuration, we added the synchronization signal obtained from the timing controller to the video signal. A dual wideband, low noise, 160 MHz operational amplifier was used for this purpose.

A signal processing IC (CXA1310AQ, Sony) was used to provide basic signal processing. It is customized for the CCD used, and for compact and low power consumption applications. It is important to mention here that another prototype had to be built to accommodate this extra chip that was not included in the initial design. It became essential to add it after analyzing the signals obtained from the first prototype, and realizing that the output signals generated had to comply with video signal standards for us to be able to obtain useful data and proceed with taking useful images. In both prototypes, the final processed analog video signal is then fed out to the wireless image transmission module.

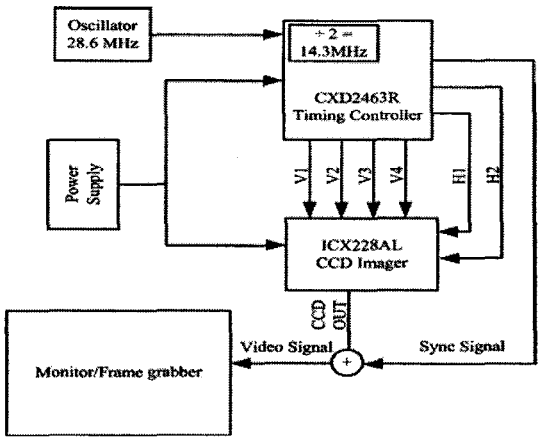

Figure 3.7: Block diagram of the signaling between the timing controller and the imager

3.3.1 Choice of Imager Technology: CCD or CMOS?

Despite the fact that both CCD and CMOS image sensors are manufactured in a silicon foundry, and the equipment and material used (silicon, silicon oxide...etc.) are similar, differences in their architecture and design flexibility have made them rivals in a vast number of applications [70]. Figure 3.8 shows the difference in architecture between CCD and CMOS imagers [67].

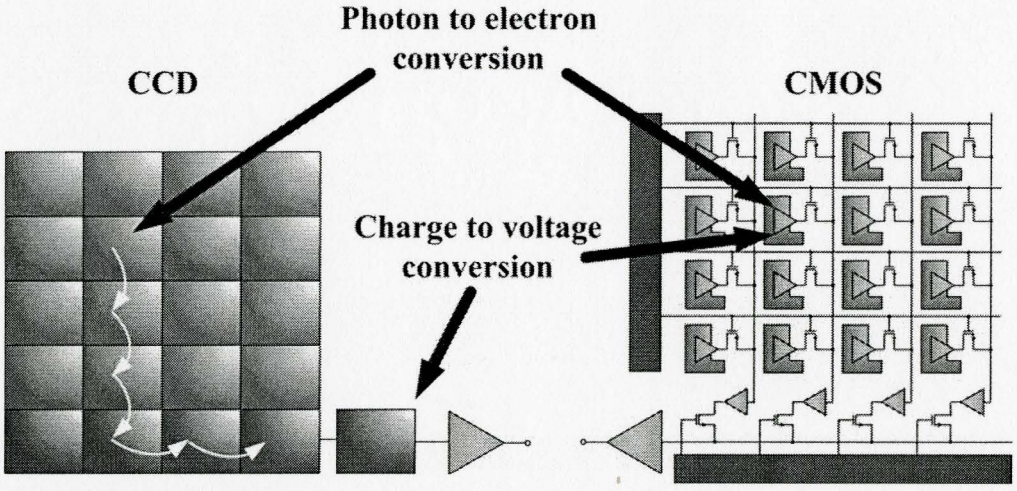

Figure 3.8: The architectures of CCD and CMOS imagers [67]

CCD imagers are made of photodiodes that are usually arranged in a 2D matrix of rows and columns, and the charges are shifted from all the pixels into only one output where they get converted into voltage, leading to a sequential read-out of the data with high uniformity. Also, the fact that all the charge is converted into a voltage in one place gives more area per pixel for light collection, which leads to high sensitivity and high image quality, accompanied by low noise, low dark-current, and high quantum efficiency. Also recently, the operating voltages they require have been falling, leading to less power dissipation, and their companion circuits have become more integrated [70].

CMOS imagers, on the other hand, have struggled to keep up with the CCDs' image quality. Their light-sensing pixels generally require a number of optically insensitive transistors, giving less room for collecting light. However, their charge-to-

voltage conversion at the pixel, along with the advancement in their production lithography and process control, the ability to integrate companion functions on the same die as the image sensor, as well as their reduced imaging system size will soon allow CMOS image quality to rival that of CCDs. They have also continuously maintained an advantage over CCD imagers in terms of power consumption, which can be a critical issue in applications that are powered by short lifetime batteries. Table 3.7 summarizes the main differences between the two types of imagers [71].

Table 3.7: Comparison between CCD and CMOS imagers [71]

Feature	CCD	CMOS
Signal out of pixel	Charge	Voltage
Signal out of chip	Voltage (analog)	Bits (digital)
System complexity	High	Low
Sensor complexity	Low	High
Camera components	Sensor + multiple support chips + lens	Sensor + lens possible, but additional support chips common
Relative R&D cost	Lower	Higher

The decision between whether to use a CCD or a CMOS imager is eventually made after weighing all the tradeoffs. For high quality images, where cost, power consumption, and speed are not of concern, CCD imagers are preferred. On the other hand, CMOS imagers may be a better choice for commercial, low cost mass-produced devices. We selected a CCD imager in our prototype, since we are more concerned in capturing high quality images to prove a concept, and all tests and measurements are performed in a laboratory environment where power consumption and size are not yet a major issue.

3.3.2 The Components Used

The Imager

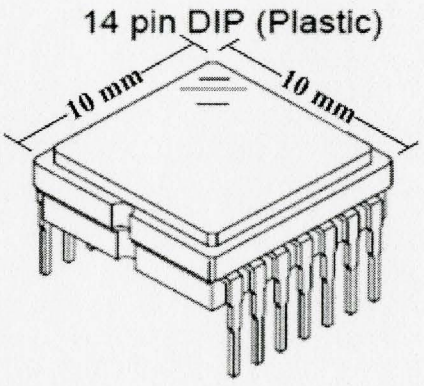

Power dissipation: 42 mW

Figure 3.9: The Sony ICX228AL CCD imager [72]

The image sensor that was chosen (ICX228AL, shown in Figure 3.9 [72]) is capable of taking high speed, high sensitivity (+3dB) video images, with good smear characteristics (-100dB) and low power consumption.

Some of its other features include:

- High saturation signal
- No voltage adjustment
- High resolution
- Excellent anti-blooming characteristics
- Continuous variable-speed shutter
- Chip size: 4.34(H) × 3.69(V) mm^2
- Unit cell size: 4.75(H) × 5.55(V) μm^2
- Substrate material: Silicon
- Optical black:

  Horizontal (H) direction: Front 3 pixels, rear 40 pixels

  Vertical (V) direction: Front 12 pixels, rear 2 pixels
- Number of effective pixels:

  768 (H) × 494 (V) approx. 380K pixels
- Total number of pixels:

  811 (H) × 508 (V) approx. 410K pixels

The selection of the imager was based on its ability to detect with high sensitivity, fluorescence signals that are within the range of 400 nm – 600 nm, while blocking out most of the UV light that might reach the CCD from the LEDs. This range was chosen because the tests we planned to carry out involved fluorescent substances that emit light at wavelengths in the range 400 nm - 600 nm after being excited with UV light. This is similar to the autofluorescence emissions from some of the inherent fluorophores usually found in the GI tract tissue, as we discussed earlier in the introduction. The spectral sensitivity characteristics of the chosen imager are shown in Figure 3.10 [72].

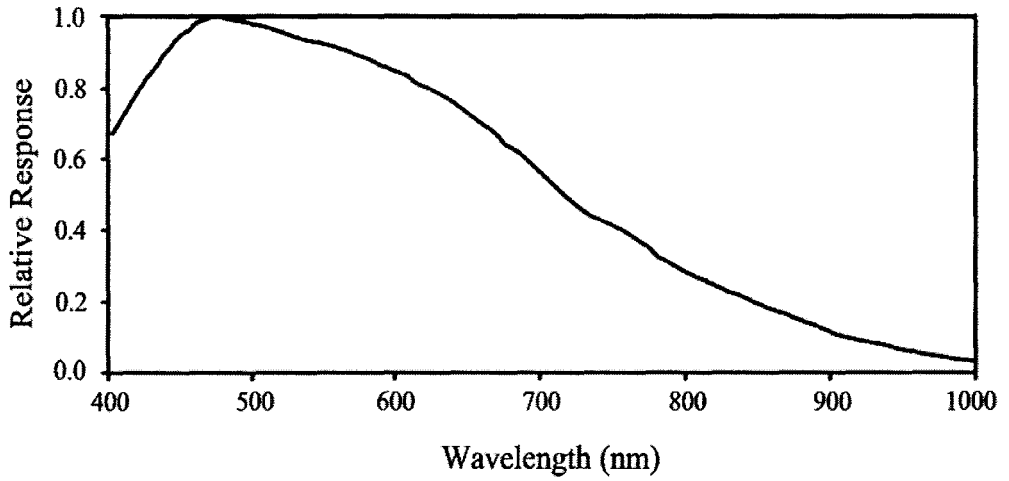

Figure 3.10: Relative spectral response of the Sony ICX228AL CCD imager [72]

The relative response of the imager remains higher than 65% over a wide wavelength range (400 nm – 650 nm), covering our wavelength range quite well and peaking at 480 nm.

The Timing controller

A timing controller (CXD2463R) was required to supply the imager with the necessary timing signals. This timing controller is a polysilicon gate CMOS integrated circuit (IC) that has a built-in synchronization signal generation function, a built-in electronic shutter, and a window pulse output for backlight compensation. It also supports

different external synchronization modes with automatic external synchronization discrimination, a useful feature when used in combination with pulsed excitation light. Some of its other features include:

- Built-in sync signal generation function
- Built-in electronic iris (electronic shutter) function
- Supports low-speed limiter for electronic iris
- Supports external synchronization
- Supports automatic external sync discrimination
- Window pulse output for backlight compensation
- Built-in V driver
- Applications:

  Surveillance camera

  Door phone camera
- Structure:

  Silicon gate CMOS IC

The Signal Processing Chip

A 32-pin chip was used to provide basic processing of the CCD output signal and provides 75 Ω output impedance. It is equipped with a wide variable automatic gain control – AGC (4 to 32dB), built-in operational amplifier, and variable white clip level for wide dynamic range (140 IRE).

The Operational Amplifier

The operational amplifier that was used (LMH6622) is a dual high speed voltage feedback operational amplifier, which is specifically optimized for low noise. It has a voltage noise specification of $1.6\ nV\ /\sqrt{Hz}$, a current noise specification of $1.5\ pA\ /\ Hz$, a bandwidth of 160 MHz, and a harmonic distortion specification that exceeds 90 dBc. It operates from ±2.5V to ±6V in dual supply mode and from +5V to +12V in single supply configuration.

The Oscillator

An oscillator with an internal crystal was used to provide a base oscillation frequency of 28.6363 MHz as required by the timing controller. This frequency is reduced to half once it enters the controller. The 'enable' pin was kept at high bias to make sure the oscillator is always on. The schematic of the oscillator circuitry is shown in Figure 3.11.

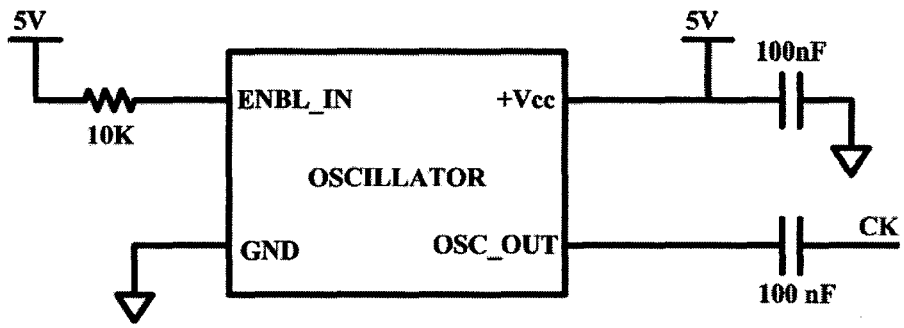

Figure 3.11: The oscillator we used

3.3.3 Circuit Design

Three different voltage regulators were used to supply the CCD, oscillator, timing controller, and signal processing chip with the required biases. Since most of the load appeared to be on the 5 V regulator, a special TO-220 low power loss package was chosen, that can handle up to 1 A of output current, 1.5 W without a heat sink, and 15 W with a heat sink. The -5 V and 12 V regulators did not have to carry much load and therefore a regular TO-92 package, which is much smaller in size than the TO-220, was used.

The CCD takes its vertical register transfer clock signals (V1-V4) and horizontal register transfer clock signals (H1-H2) from the timing controller. These signals determine when the pixels and lines and frames are read. Two biasing voltages were required, V_{CC} at 12 V and V_L at -5 V, with a supply current of about 3.5 mA. The substrate clock (SUB) pin and the reset gate (RG) pin were kept open, because a DC bias is generated inside the CCD. Figure 3.12 shows the pin configuration of the CCD imager.

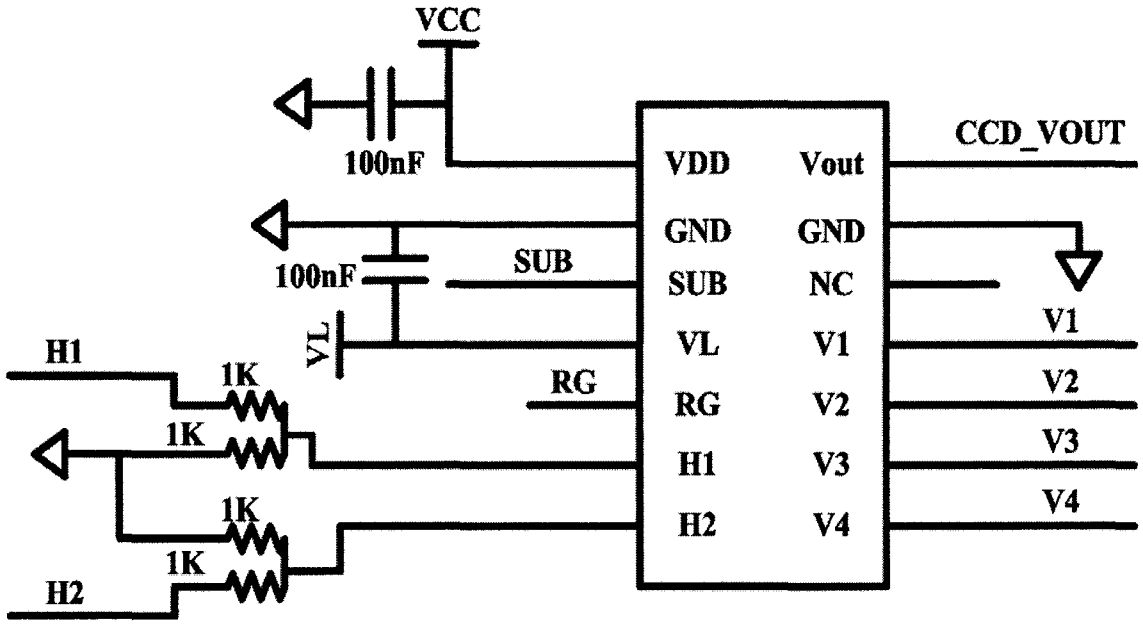

Figure 3.12: The CCD imager pin configuration

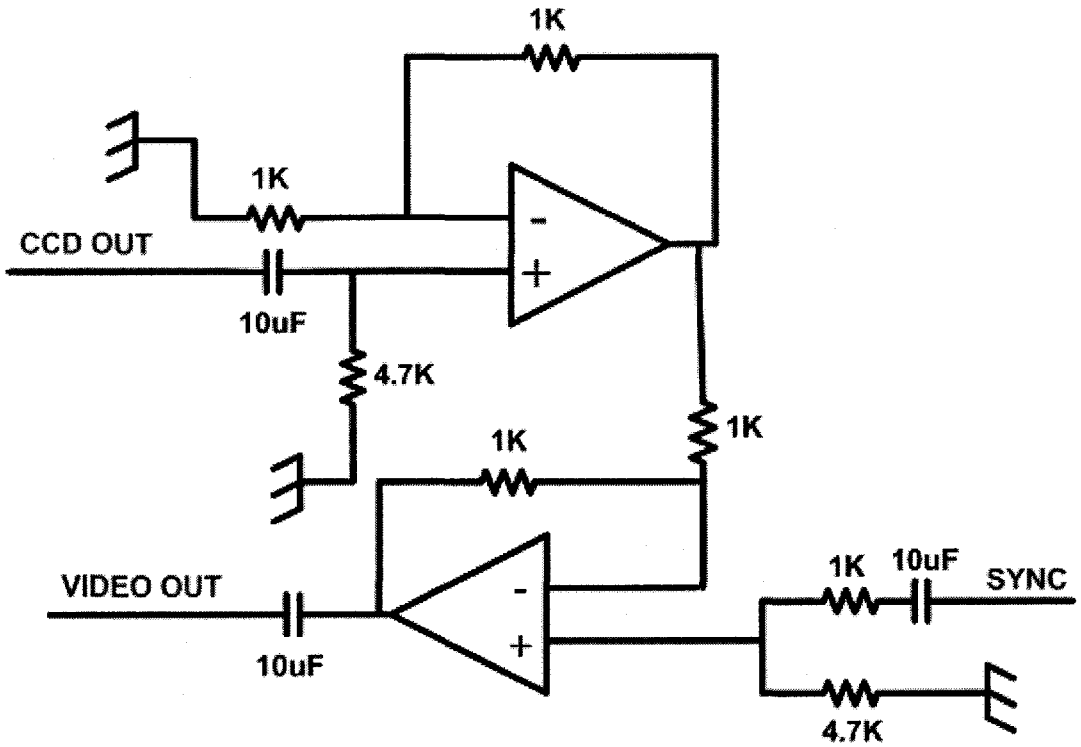

Figure 3.13: Buffer and summer configuration

The weak output signal from the CCD is first buffered through a unity gain amplifier as shown in Figure 3.13, and then later added to the synchronization signal (SYNC) using a difference amplifier configuration as seen in the second op-amp. The output of such a configuration is:

$$V_{out} = (V_2 - V_1)\frac{R_x}{R_y}, \tag{3.1}$$

where V_{out} in our case is the VIDEO OUT signal, V_2 is the synchronization signal SYNC, and V_1 is the CCD output signal, therefore:

$$VIDE_{OUT} = (SYNC - CCD_{OUT})\frac{R_x}{R_y}. \tag{3.2}$$

This means that the synchronization signal is added to the inverse of the CCD output signal. The CCD output signal needed to be inverted as indicated by the CCD data sheet.

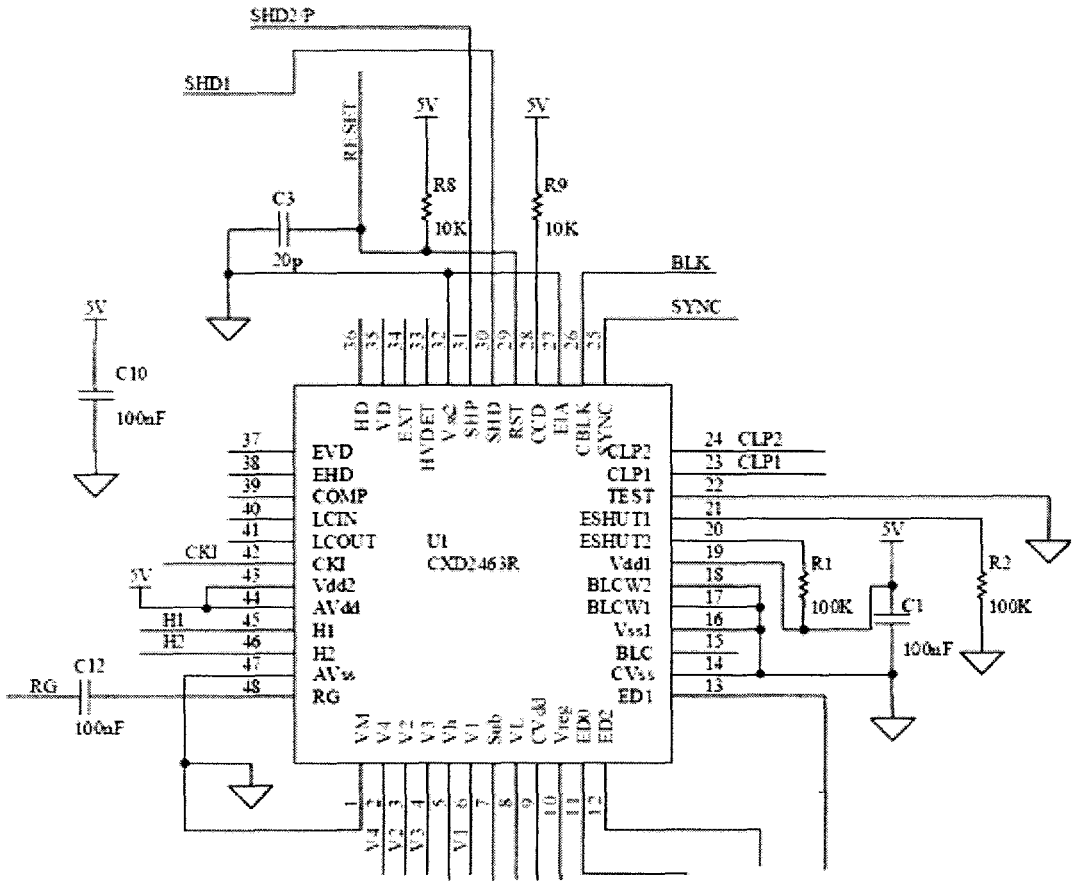

Figure 3.14: The timing controller pin configuration

Figure 3.14 shows the pins V_M and V_H which provide power to the vertical drive, where V_M is connected to ground and V_H is connected to 12 V. Terminals V_1, V_2, V_3, and V_4 are pulse outputs for the CCD register drive. SUB, is also connected to the CCD, and serves as a pulse discharge output. V_L is the negative power supply for the vertical drive, connected to -5 V, and CV_{dd} and CV_{ss} provide positive power supply, and V_{reg} provides bias current supply for the comparator respectively. ED_0, ED_1, and ED_2 are shutter speed controls that can vary between 1/100 and 1/100000 with different high and low combinations, therefore they were connected to a switch between 5 V and ground.

The timing controller also has a function to output the window pulse for backlight compensation. The backlight compensation pulse is output from BLC according to the high/low combination of $BLCW_1$, and $BLCW_2$, and ranges between the following

window types: full-screen photometry, bottom emphasis photometry, center emphasis photometry, and bottom plus center emphasis photometry. The electronic shutter mode was chosen instead of the electronic iris mode by setting $ESHUT_1$ and $ESHUT_2$ to low and high respectively. The clamp pulse outputs, CLP1, CLP2, and the sync and blanking outputs, SYNC, and CBLK, and data sample-and-hold pulse, and pre-charge level sample-and-hold pulse SHD_1 and SHD_2, are all sent to the signal processing chip.

The controller can be set to either EIA or CCIR standards (the B/W standards for the more commonly known NTSC and PAL standards). We set our controller to EIA by setting the EIA pin to low. The clock is provided via the pin CKI which is obtained from the 28.6363 MHz oscillator mentioned before. Finally, H_1 and H_2 provide clock outputs for the CCD horizontal register drive, and are powered via pins AV_{dd} and AV_{ss} which are both connected to 5 V and ground respectively.

3.3.4 PCB Design

The first prototype, which can be seen in Figure 3.15(a), was built on a 2-layer, 2.64 cm x 8.26 cm PCB. The hole on the right hand side was intentionally placed there to be able to hold the board steadily on an optic table. The CCD imager can be seen on the left hand side of the prototype. It was mounted on the PCB using a 90° angle header. Right behind the CCD are the LEDs, as shown in the figure. The signal is fed out via an SMA connector and an extra header was added on the left to be able to access signals of interest during the testing phase. In the center of the board, we can see the switches which were used to control the electronic shutter speed.

The second prototype can be seen in Figure 3.16(a). It was built on a 4-layer, 2.7 cm x 10.1 cm PCB. The 2 extra layers were necessary due to the increased complexity of the layout interconnections with the extra chip that was added. The hole was removed in order to be able to accommodate the new chip and all its circuitry with the minimum increase to the length of the board. The full schematic of the circuit that was implemented on this PCB is shown in Appendix A.

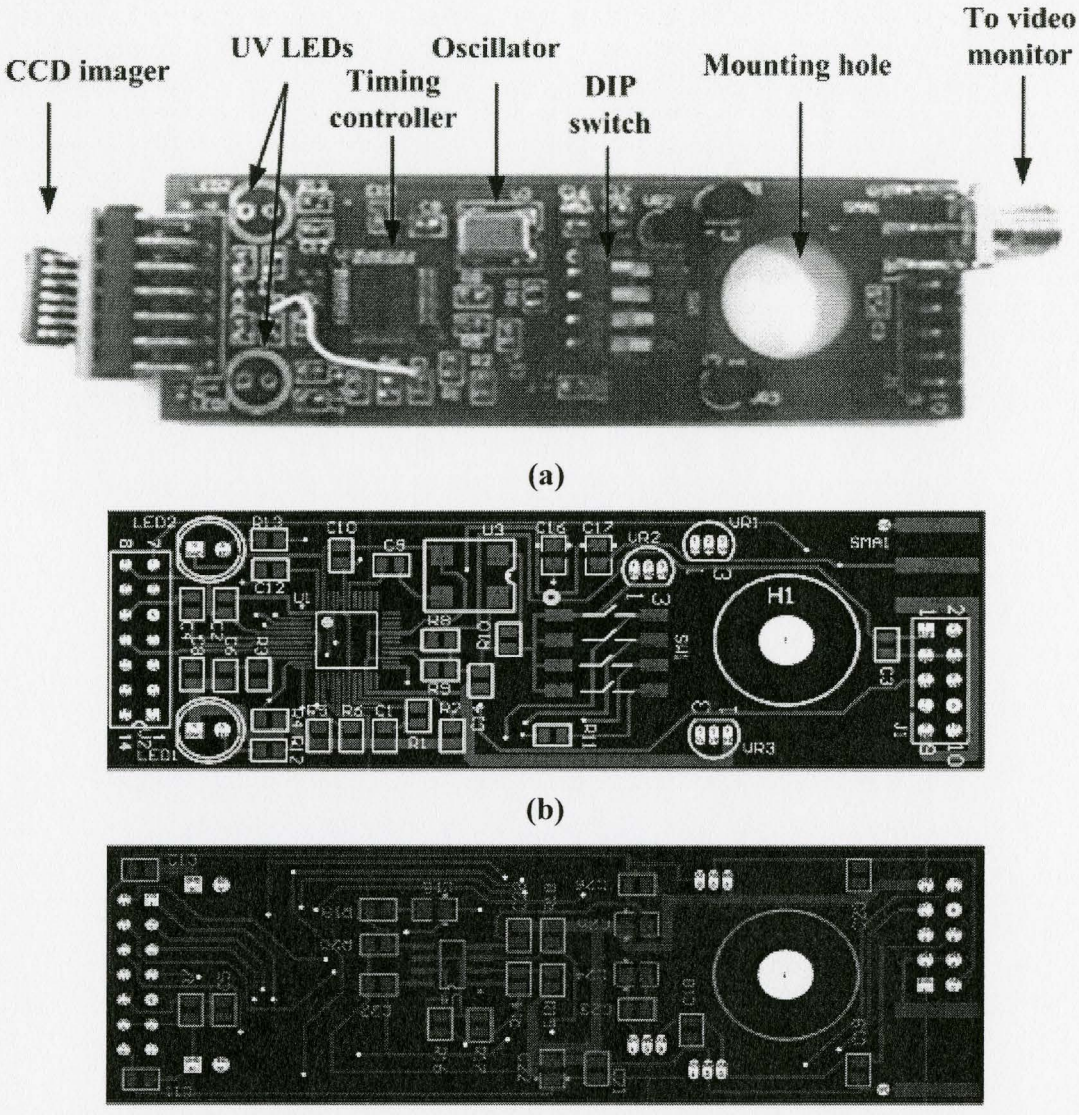

Figure 3.15: a) A picture of the first prototype, showing the main circuit parts used, b) the PCB's top layout layer, c) the PCB's bottom layout layer

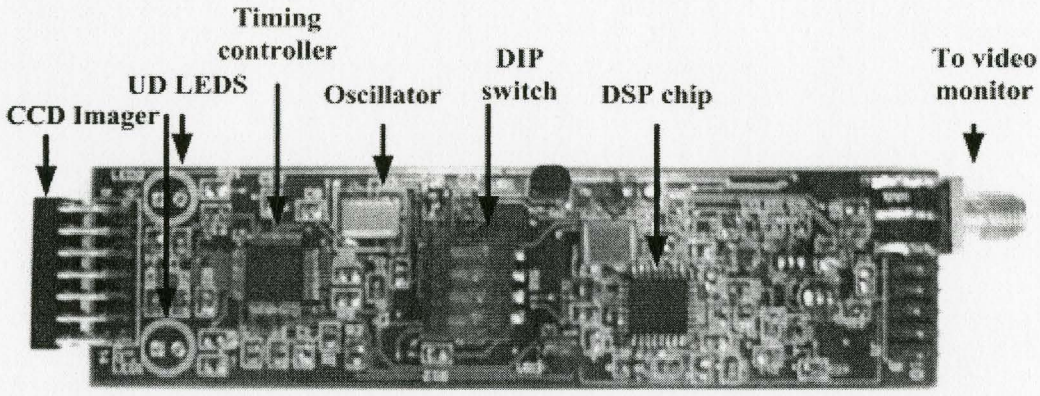

(a)

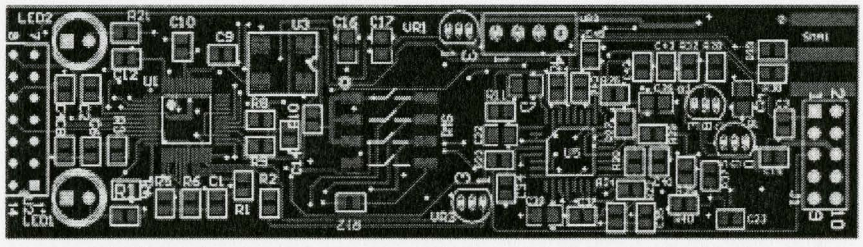

(b)

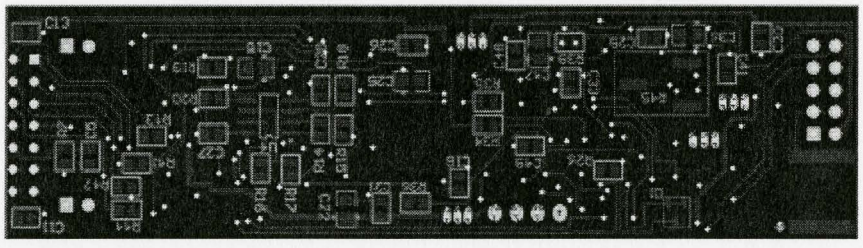

(c)

Figure 3.16: a) A picture of the second prototype, showing the main circuit parts used, b) the PCB's top layout layer, c) the PCB's bottom layout layer

3.4 The Wireless Transmission Module

The wireless transmission module was designed by two of my colleagues, and it is discussed briefly in this thesis for completeness.

Wireless data transmission from endoscopic capsules has several technical challenges. Mismatch in information volumes, restrictions for power consumption and size are the main ones. We have explored several possible solutions to meet these challenges. The radio frequency (RF) wireless transmission system was designed, and a prototype system with off-the-shelf components was fabricated on the same PCB as the image acquisition module. A block diagram of the design is depicted in Figure 3.17. An off-the-shelf RF link (transmitter and receiver) was used for prototyping purposes. The power consumption of the system is sufficiently low such that it can be completely powered by two 1.5 V Li-ion batteries.

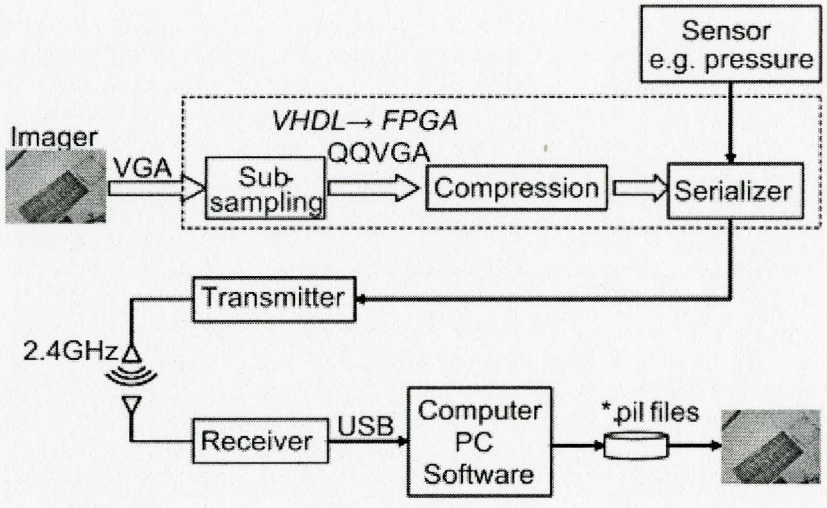

Figure 3.17: Data flow diagram of the wireless imaging/sensing system

Due to the use of the high-resolution CCD imager, the image data volume as acquired by the imager is larger than the current bandwidth constraints for wireless data transfer. For example, a VGA image frame consists of 640 columns x 480 rows, which is equivalent to 307,200 pixels, each corresponding to 2 bytes, resulting in 624,400

bytes/frame or approximately 5Mbit/frame. On the other hand, wide-band wireless communication is limited to 1Mbit/sec, or it will take 5-10 seconds per image frame, if one tries to transmit a VGA image directly by wireless communications. Therefore, as shown by the data flow in Figure 3.17, the VGA images are sub-sampled to QQVGA (quarter-quarter VGA), which reduces the image volume 16 times, and then data compression is applied to achieve additional reduction of 4 times. Thus, the volume of the compressed image frame was reduced to about 10-12 kBytes, allowing us to include correction codes and other useful information but still having a frame data volume below 100 kbits/frame.

The data from the compressed images are combined in the serializer, which feeds the RF transmitter at a rate of 250 kbps, and the RF link forwards the data to a host computer with an acceptable data loss of 10%, which can be recovered in real time using the correction codes mentioned above. All functions in the flow diagram of Figure 3.17 were performed in real time, from image acquisition through compression, transmission, receiving, storing, to decoding and visualization of video stream on the host computer. The power consumption of the module was also sufficiently low that all aforementioned procedures can be operated using battery power. The prototypes for the different modules of the wireless fluorescence imaging system were tested, and they functioned as desired. A custom housing was designed and the entire wireless imaging system including the wireless transmitter was integrated and tested in free space in a setup as shown in Figure 3.18.

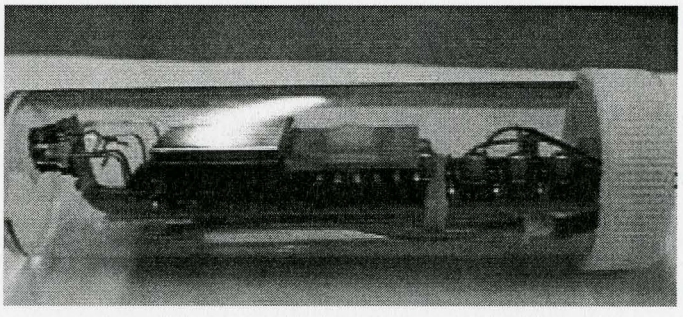

Figure 3.18: The custom housing in which the entire wireless imaging system including the wireless transmitter was integrated and tested

Chapter 4

SET-UP, MEASUREMENT RESULTS, AND ANALYSIS

4.1 General Set-Up

The whole set-up, including the LEDs and the CCD imager and its circuitry, can be encapsulated inside a catheter-looking endoscope. However, for testing and measurement purposes, the set-up was kept uncovered to provide enough flexibility for moving parts around. For instance, spectral selection was implemented using a filter wheel fixed in front of the CCD imager. The LEDs were kept off the PCB and placed in different positions at different distances from the tested samples, although they were accounted for during the design of the prototype and can be installed in place on the PCB at any time. The set-up can be seen in Figure 4.1.

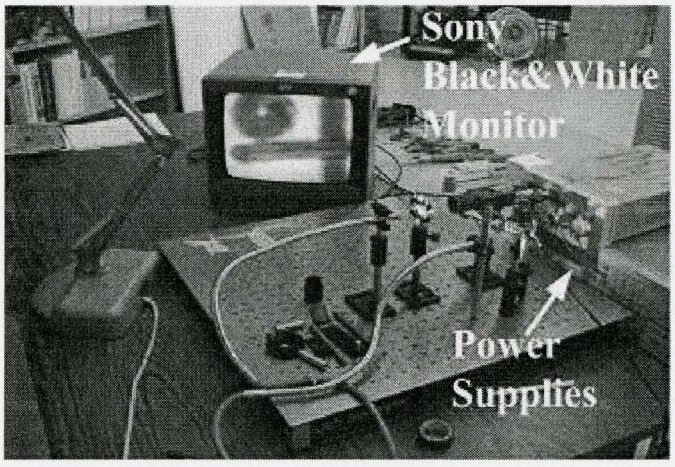

Figure 4.1: Initial testing set-up, showing imager, monitor, and power supplies

Three different power levels were required for the CCD imager, timing controller, and signal processing chips (12 V, 5 V and -5 V) and two external power sources were used for this purpose. For miniaturization purposes, the external power supplies would eventually have to be replaced by internal batteries, or external power coupling, which is becoming a more common alternative nowadays. These powering options will be discussed later in more detail in the future work section.

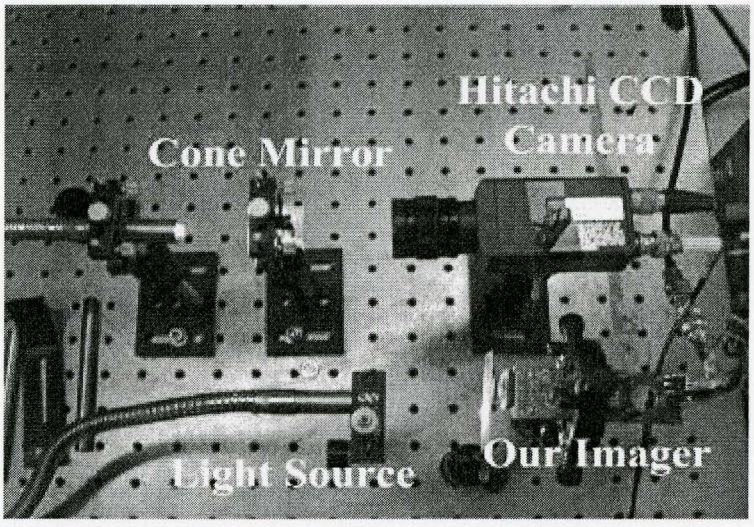

Figure 4.2: Our imager, compared to a Hitachi CCD camera

Figure 4.2 shows the general set-up of the system, including the optical arrangement. A Hitachi CCD imager was used for comparison. Images from the first prototype were captured and saved using an image acquisition board attached to a computer. Due to the video signal not being a standard video signal, we could not obtain clear continuous images using the acquisition board, which triggered the addition of the signal processing chip; this problem is further discussed in detail later in this chapter. After integrating the optical system and the electronic imaging modules, proof-of-concept tests were conducted on the completed endoscopic fluorescence imaging system using fluorescent phantoms.

The set-up was placed on an optical table in a specially designed dark room. That exposes the sensor to the least amount of radiation, and minimizes the amount of ambient

light reaching the sensor. Different tests were performed to demonstrate the effectiveness of our "proof-of-concept" prototype. Some tests involved regular white paper with certain markings or patterns drawn on them, or fluorescence phantoms consisting of white paper samples or porcine skin with fluorescent dyes administered to them.

Porcine tissue was used because the pig is one of the animals that are considered to be one of the most common models for investigations related to medical diagnostics of human tissues. Differences in the intensity and form of the fluorescence signals of pork tissue are believed to be due to the different concentrations of inherent fluorophores and the different geometrical nature of the skin tissue. Pork skin contains melanin in the dermis and haemoglobin in the epidermis, which absorb light in the 330 nm – 400 nm range, which covers the excitation wavelength we are using in our measurements (365 nm). It also contains NAD, NADH and collagen which are also found in the human GI tissue [98].

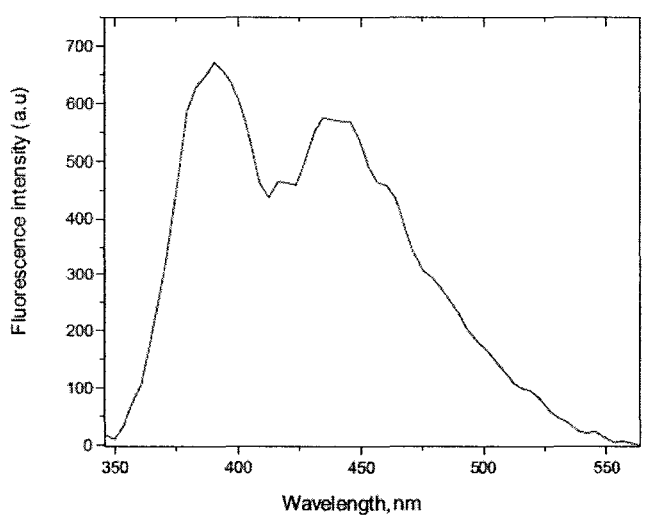

Figure 4.3: The fluorescence spectra of porcine skin samples [98]

Figure 4.3 shows the LIF (light induced fluorescence) spectra of a porcine skin samples [98]. The results shown are similar to those observed from GI tissue. The fluorescence observed falls in the range 400 nm – 600 nm, with peaks at 390 nm, 430 nm, and 460 nm. The 390 nm and 460 nm peaks were related to the collagen cross-links and

NADH. In our experiments, the porcine tissue's fluorescence response was enhanced using two fluorescence dyes that emit light in the red and green regions when excited by UV light, to mimic a real case scenario, in which certain regions emit stronger fluorescence signals than others, depending on whether the tissue is healthy or malignant.

4.2 Test Results

A series of tests and experiments were performed on the prototype at different stages. The LEDs' spectral characteristics and output power were tested to ensure their capability of exciting the tissue. The validity of the video signals obtained from the CCD images as standard video signals was also tested, and the system's image contrast and dynamic range were investigated. The results are presented in the following subsections.

4.2.1 The LEDs

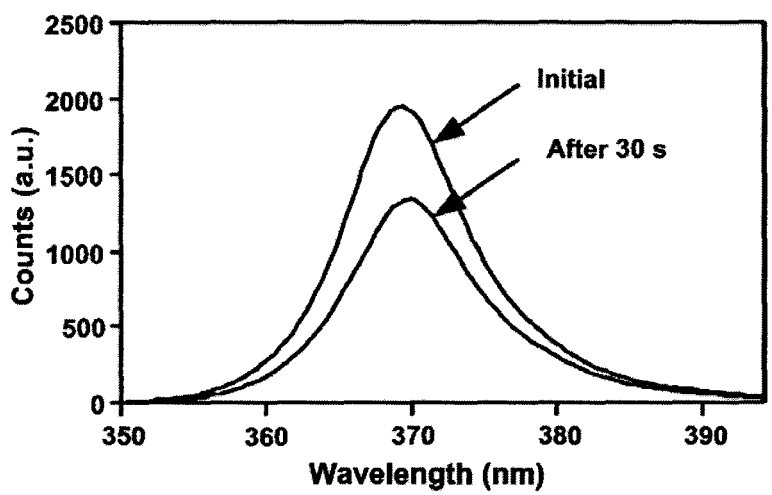

Figure 4.4: Emission spectra of the UV LEDs

The emission spectral features and output power of the UV LEDs were first characterized. The emission spectra were measured by a calibrated fiber optics spectrometer (OSM400, Newport, Irvin, CA). As shown in Figure 4.4, the LEDs exhibited a symmetrical Gaussian-like profile peaking around 370 nm with a full-width-half-maximum (FWHM) bandwidth of ~10 nm. It was noticed that the output intensity

decreases considerably soon after powering-on the device and then stabilizes after 30 seconds, most likely influenced by the device's thermal stability. When the experiment was repeated to determine how the radiant power of the LEDs stabilizes over time, and how that changes with different currents, the data in Figure 4.5 was obtained. As we can see in the figure, with higher currents, it takes the LEDs longer to stabilize, and the drop in the radiant power is steeper. This is mainly due to the increase in the LEDs' temperature with time. The radiant power of an LED decreases as a function of increasing temperature, and variations of the order of - 1%/°C are typical for both direct and indirect band-gap materials [99].

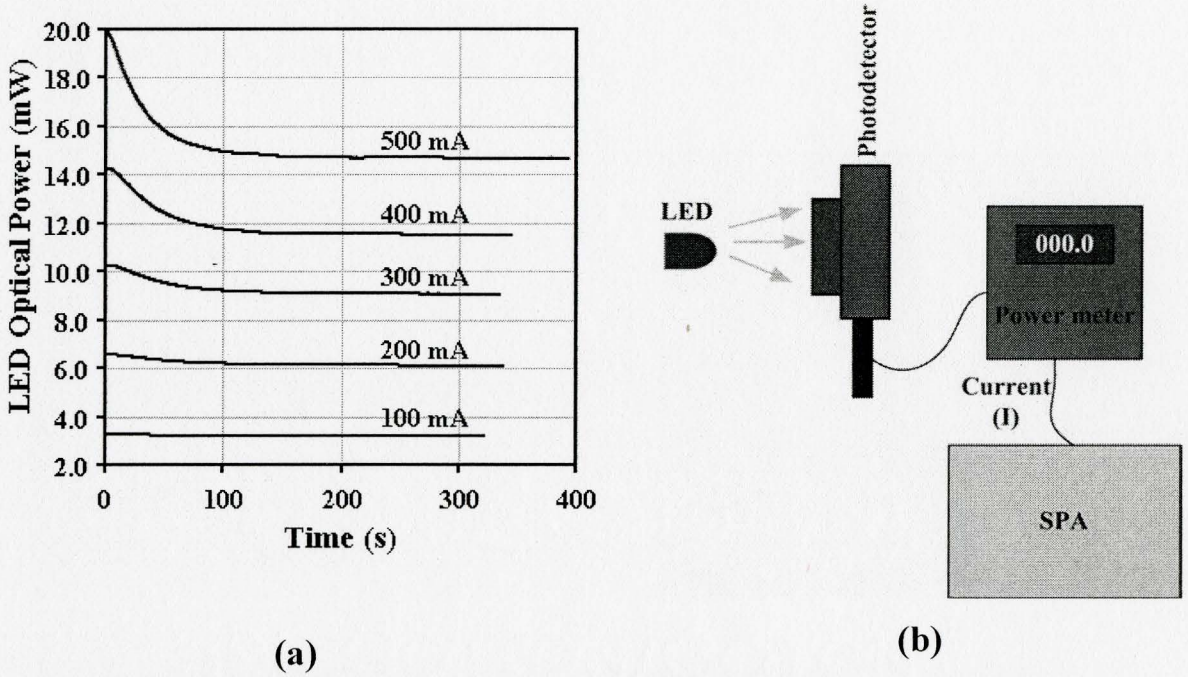

Figure 4.5: (a) The drop in LED optical power with time, (b) Schematic of the measurement setup

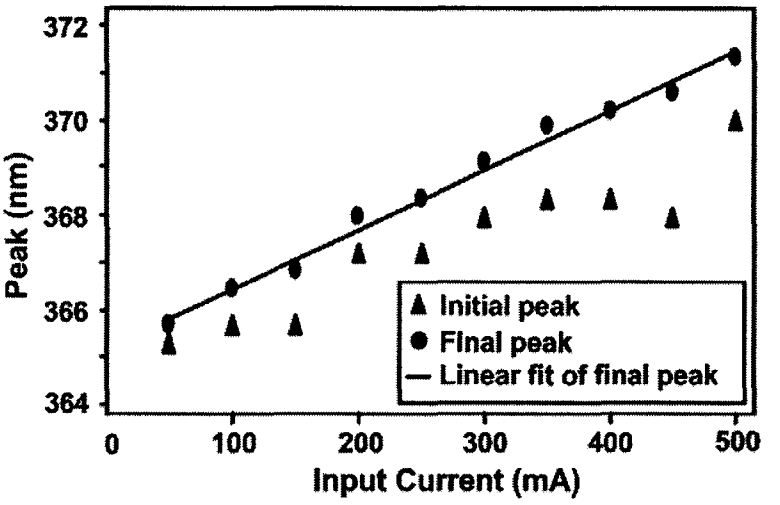

Figure 4.6: Spectral peak vs. input current of the UV LEDs

There were observable variations in the emission spectrum as well as the spectral bandwidth at different input current settings. As shown in Figure 4.6, the peak of the emission spectrum displayed significant red-shift as the intensity was higher. Similarly, the bandwidth of the emission spectrum also increases slightly from 8 nm to 11 nm as the current/intensity increases as shown in Figure 4.7.

The changes in spectral emission features may be attributed to the changes of the materials' characteristics with the rise of temperature accompanying the increase in input current. The energy band-gaps in both direct and indirect semiconductors tend to become smaller when the temperature increases, which causes an increase in the emitted peak wavelength. For direct gap emitters, the increase is an estimated 0.2 nm/°C [99]. Overall, these changes are minor compared with the relatively broad absorption band of the typical tissue fluorescence components such as collagen and lipids. However, they should be considered while choosing an appropriate long wavelength pass filter to suppress backscattered excitation light. In our system, a 380 nm cutoff filter was chosen to reduce the transmission of the excitation light at low current, which corresponds to a 360 nm peak. For high current use, e.g. at the 370 nm emission peak, a 400 nm long-pass filter may be required to sufficiently suppress the backscattered excitation light.

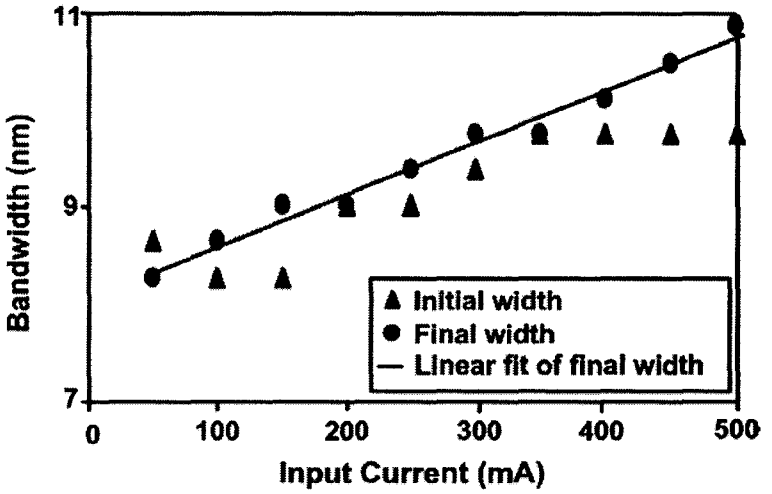

Figure 4.7: Spectral bandwidth vs. input current of the UV LEDs

The output power was measured using an optical power meter (1830C, Newport) with a visible detector head (818-SL/CM, Newport). The measurements were performed 60 seconds after the LED was powered on to make sure they were thermally stabilized. It is shown in Figure 4.8 that the output power increases linearly with the input current between 0 mA and 500 mA, the manufacturer specified maximum operating current.

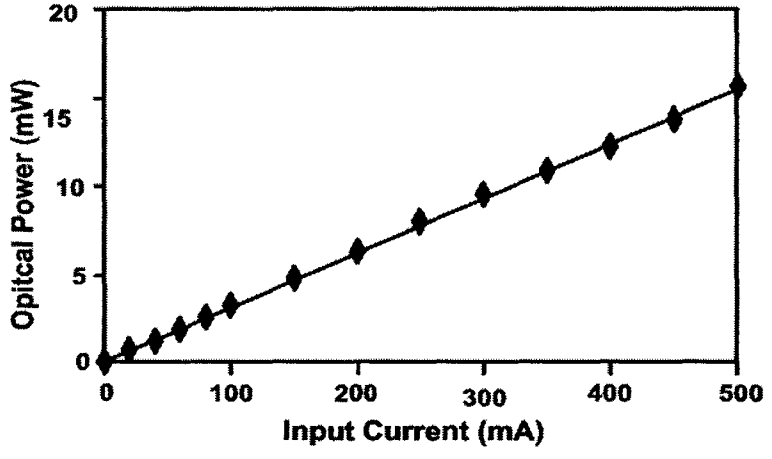

Figure 4.8: Optical power vs. input current of the UV LEDs

4.2.2 The Filters

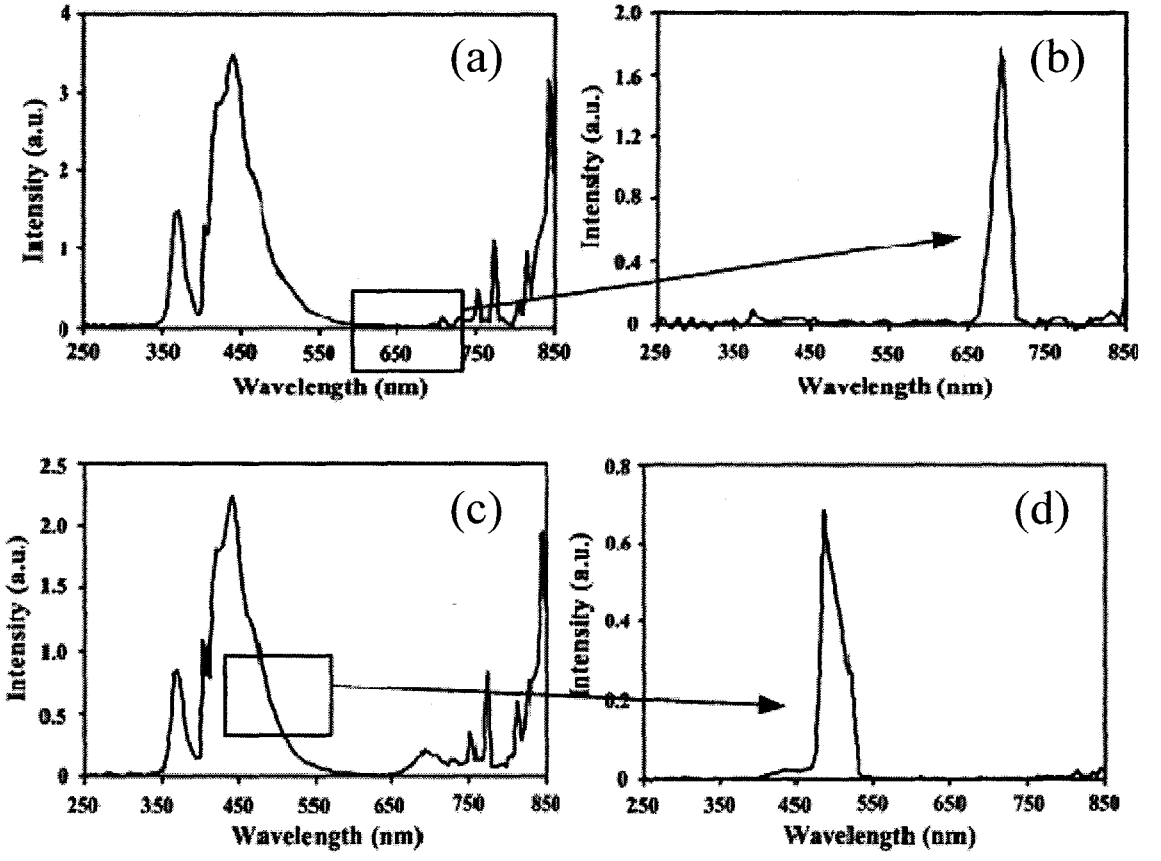

Figure 4.9: The measurement results of the emission spectra of a) the red dye with no filter, b) the red dye with filter, c) the green dye no filter, d) the green dye with filter

Two band-pass filters with different spectral ranges (red and green) were used in the testing phase to demonstrate spectral selectivity in the prototype. These filters were chosen because, as we saw in Figure 2.1(b) in Chapter 2, which illustrates the fluorescence emission spectra of colon tissue, we can see that the emitted fluorescence signal of the normal tissue peaks at two particular wavelengths, around 510 nm (green) and 635 nm (red). Both of these peaks are significantly modulated in the case of moderate dysplasia. This was the reason we chose the green and red filters. We wanted to investigate the imager's ability to detect fluorescence signals at these wavelengths, and

prove that we can emulate a real-world scenario by paying particular attention to these wavelengths.

The filters' effectiveness and the dyes' emission spectra were tested first. The red and green dyes were placed on paper, and UV light was used to induce fluorescence. The emission spectra were measured using a spectrometer, and the results are shown in Figure 4.9. Figure 4.9(a) shows the emission spectrum of the red dye before the filter was placed. The strongest and most significant peak is seen around 450 nm which indicates that visible light dominated. When the red filter was inserted between the sample and the spectrometer head, the peak shifted to around 690 nm as seen in Figure 4.9(b). This demonstrates that all other wavelengths can be significantly suppressed while allowing the wavelength of interest to pass through. Figure 4.9(c) shows the emission spectrum of the green dye before the green filter was inserted. Again, the surrounding visible light dominated, but when the green filter was inserted, the peak shifted to 485 nm, while all other peaks became relatively insignificant (Figure 4.9(d)).

4.2.3 The Imager Problem

When the first prototype was completed, clear video images were obtained when the images were viewed on a Sony video monitor. However, when an image acquisition board was used, thin black vertical lines were seen all across the images. Figure 4.10 shows a comparison between an image that was captured using the acquisition board (left) and an image that was captured using the Sony monitor (right).

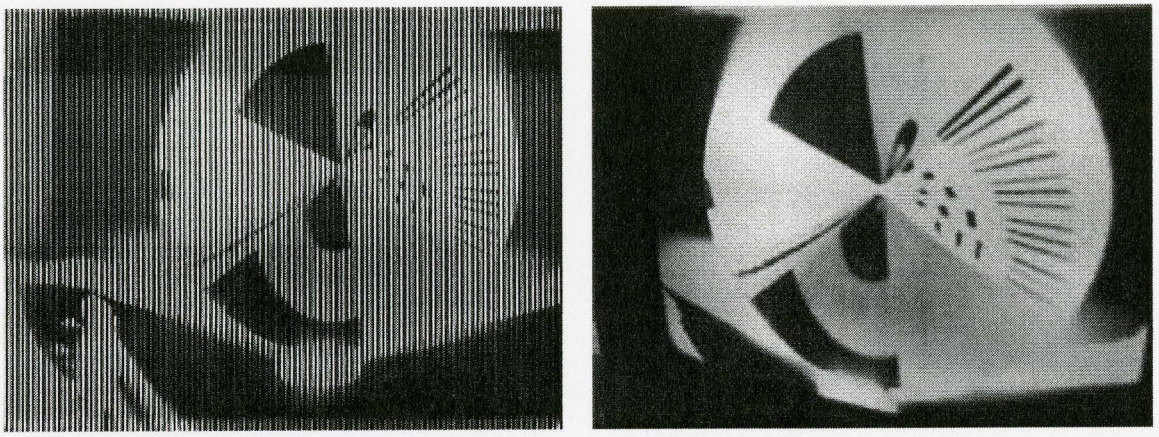

Figure 4.10: Image captured using the acquisition board (left) and image captured using the Sony monitor (right)

An initial attempt to solve the problem involved extra filtering of the output video signal from jitter with frequency equal to that of the oscillator signal, which was thought to be propagating through the PCB into the output signal. However, even after this jitter was significantly reduced, the black lines did not disappear. To trace the problem, output signals were obtained from a CCD camera and were compared with our imager. Both signals can be seen in Figure 4.11, where the top signal is the one obtained from the CCD camera, and the bottom is the one obtained from our CDD imager. Two main differences can be observed; the signal in the interval between one horizontal pulse and another is more jittery in our imager (as explained earlier), and the horizontal pulses in

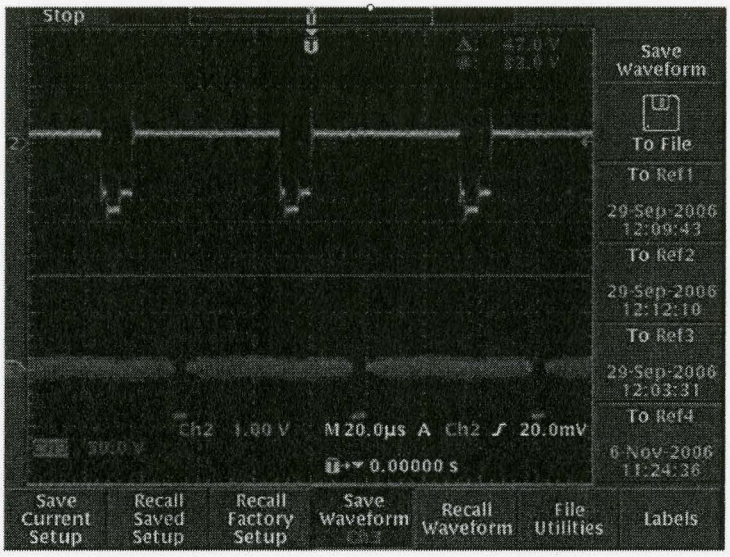

Figure 4.11: The horizontal pulse signal of the CCD camera (top) and our imager (bottom)

our imager consist of only one step, whereas those from the CCD imager consist of two steps. Figure 4.12(a) shows a close-up on an interval between two horizontal pulses, where the frequency is 14.3 MHz as mentioned earlier, and Figure 4.12(b) is a zoom out that captured one vertical pulse. As can be seen, after the downward step, the signal goes up to a higher level than it was before and that was also suspected as a possible cause of the problem. Figure 4.12(c) is a zoom out capturing a series of horizontal pulses, and Figure 4.12(d) is a zoom out capturing a series of vertical pulses. After all filtering attempts were exhausted, and after contacting National Instruments from which the image acquisition board was obtained, we came to the conclusion that the image acquisition board would only be able to display video signals that come in the standard format, and therefore the extra step had to be introduced (Figure 4.11).

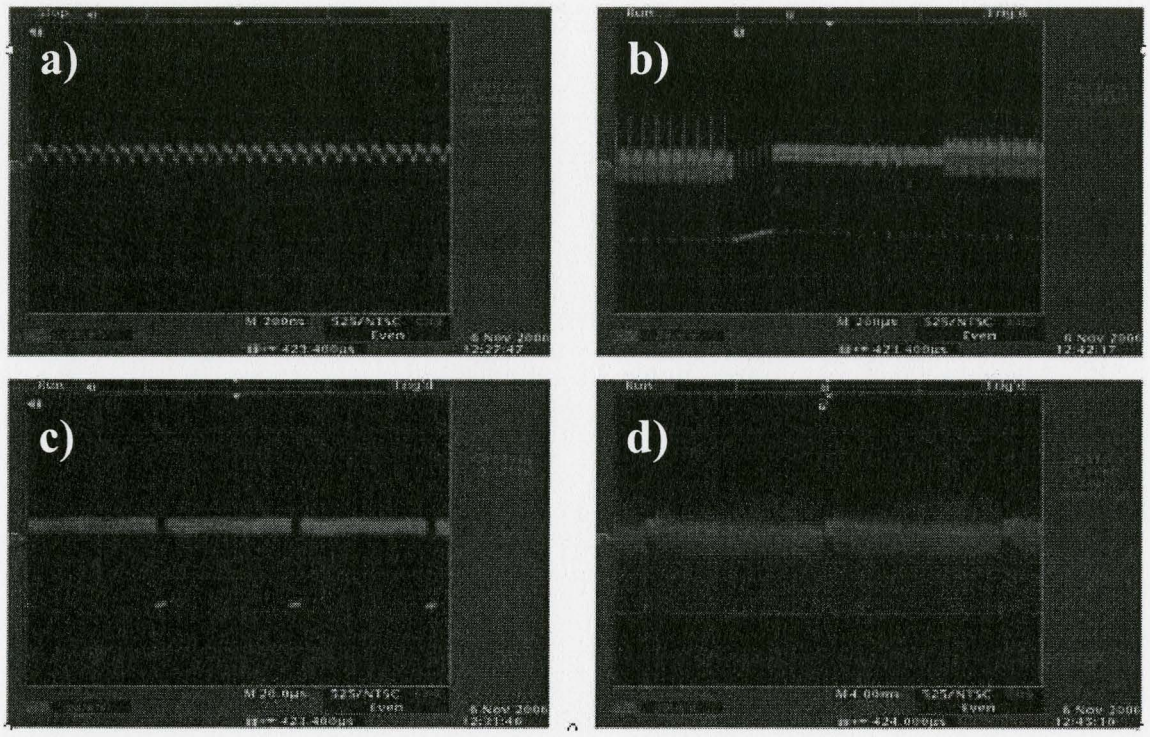

Figure 4.12: a) Interval between two horizontal pulses, b) Interval between two vertical pulses, c) zoom out capturing a series of horizontal pulses, d) zoom out capturing a series of vertical pulses.

The signal processing chip was suggested by Sony, the manufacturer of the imager and the timing controller chips. The extra chip was integrated in the second prototype, and the problem was solved. Figure 4.13 shows the timing and step levels of the signals that are fed to the signal processing chip (DATA and SYNC), and the output signal of the chip that represents a standard video signal. After the DATA signal is inverted, the level of the horizontal pulse is brought down to the same level as that of the SYNC signal, thus clearly defining the blanking level of the signal.

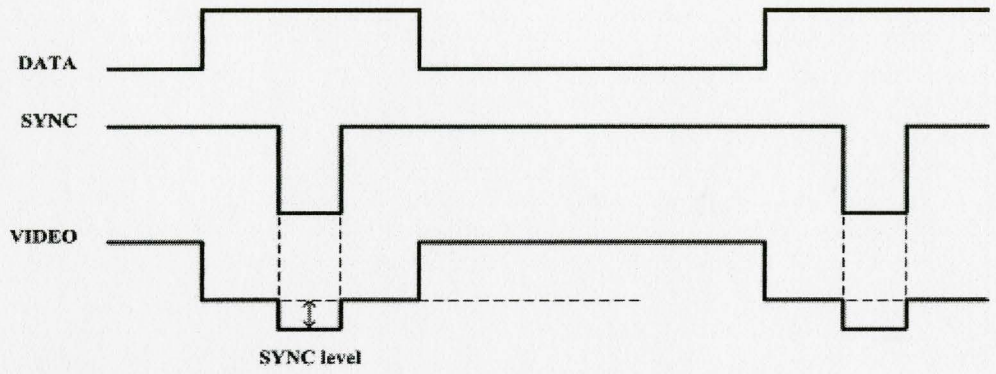

Figure 4.13: Timing diagram of the DATA, SYNC, and VIDEO signals

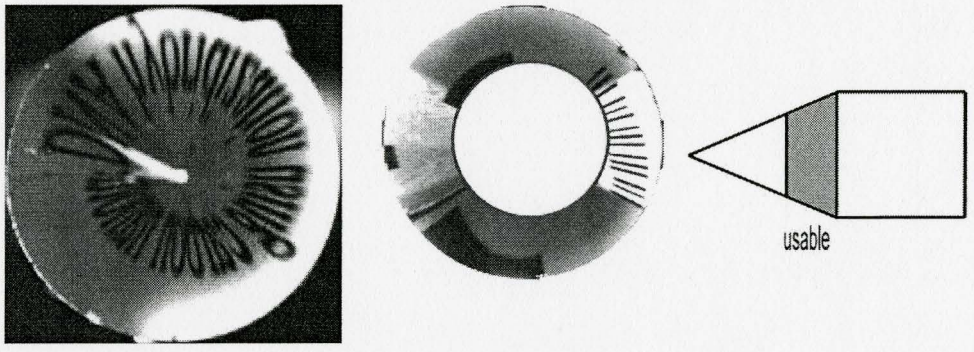

Figure 4.14: The images taken by the conical mirror

The cone mirror was also tested by capturing images off a paper with text printed in black ink and wrapped around the cone mirror at a distance. This was necessary to emulate the outline of the GI tract where the pill would be expected to detect irregularities around the image sensor and not just in front of it. The acquired image is spatially distorted by the conical mirror, as shown in Figure 4.14. The spatial resolution of the distorted image becomes worse when regions closer to the apex of the cone were used. Therefore, only the outer region of the image may be used and the apex of the conical mirror can be removed and the area it occupies can be reserved for a future forward imaging channel. The distorted image was subsequently unwrapped by using a polar-to-rectangular distortion filter. This filter reads the image as if it was plotted on a polar coordinates system, then re-plots each pixel onto a cartesian plane. Later, a Matlab code was written to provide better unwrapping and to demonstrate our ability to provide image unwrapping in real-time. The code is shown in appendix B. The initial distorted

image is shown in Figure 4.14 (left) and the unwrapped image using the Matlab code is shown in Figure 4.15.

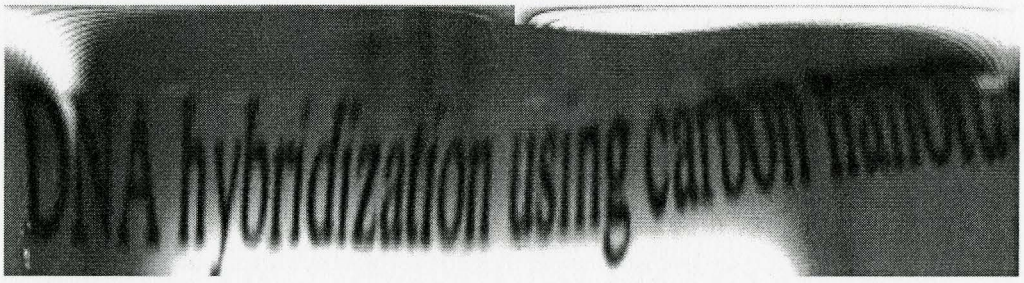

Figure 4.15: The unwrapping of the images taken by the conical mirror

4.3 Measurement Results and Data Analysis

In the following measurements and analysis, a target consisting of white paper was used, with a pattern resembling a chess board printed on it in black ink. The goal behind this analysis is to determine the imager's ability to differentiate between the levels of gray of white and black pixels. We made sure that the black spots on the target occupy the same area as the white spots, and the same target was used throughout the different experiments, thus keeping the target's optical properties constant.

Optical Power at CCD

First, a number of measurements were carried out to determine the losses in optical power during the propagation of the light signal through the optics, and to determine what part of the optical set-up is mostly responsible for these losses. The power measurements were taken using an optical power meter with a photo-detector that operates in the visible-light region. The current through the LEDs was swept between 2 mA and 200 mA, and the power was measured at the surface of the CCD imager. This measurement was repeated 2 times: once with a green color filter, the lenses, and a UV filter placed between the target and the CCD, and a second time with only the lenses and the UV filter in front of the CCD. The results are presented next.

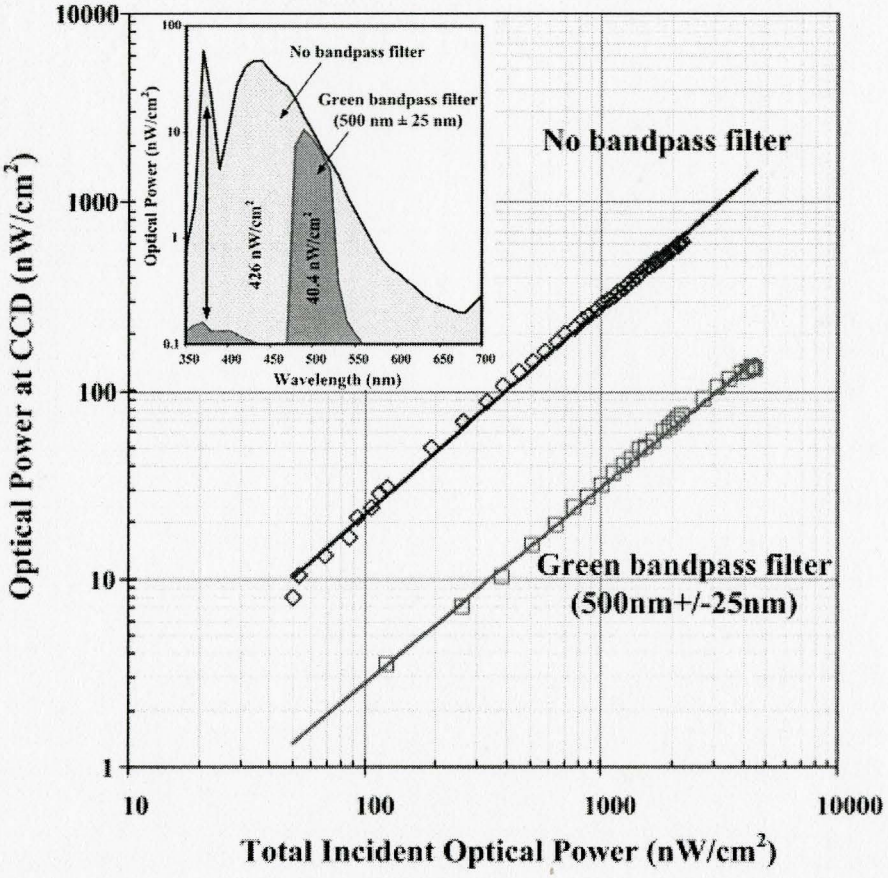
Optical Power at CCD (nW/cm²)
Total Incident Optical Power (nW/cm²)
No bandpass filter
Green bandpass filter
(500nm+/-25nm)
Optical Power (nW/cm²)
Wavelength (nm)
No bandpass filter
Green bandpass filter
(500 nm ± 25 nm)
426 nW/cm²
40.4 nW/cm²

(a)

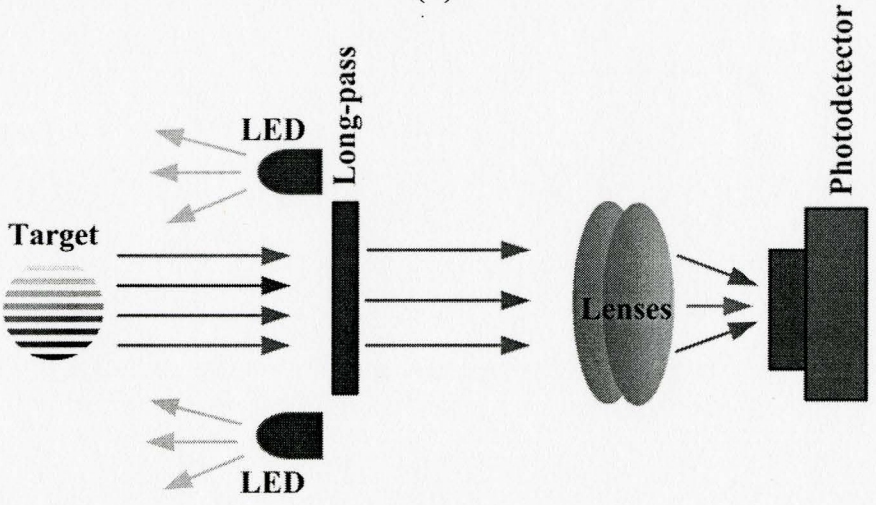
LED
Long-pass
Photodetector
Target
Lenses
LED

(b)

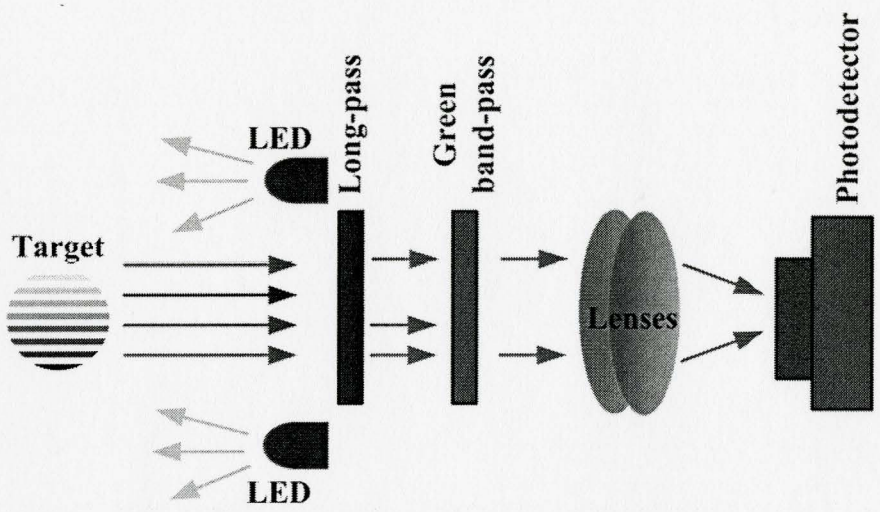

Figure 4.16: Optical power at the surface of the CCD imager

Figure 4.16 shows the optical power at the surface of the imager. The horizontal axis is the optical power obtained from the target and incident to the optical system. The diamonds represent the optical power at the surface of the imager when no band-pass filter is used (Figure 4.16 (b)), and the squares represent the optical power at the surface of the imager when a green band-pass filter is inserted between the target and the rest of the optical system (Figure 4.16 (c)). When the band-pass filter was inserted, the total incident power on the CCD decreased 10 times. As an example, when the total optical power incident on the whole system is 100 nW/cm^2, the optical power incident on the CCD surface when the green band-pass filter is not inserted is 20 nW/cm^2, but when the green-band-pass filter is inserted, the optical power at the CCD surface is only 2 nW/cm^2, The reason is that only portion of the spectrum reaches the CCD when the band-pass filter is inserted. This is illustrated in the inset, which shows the power distribution over the wavelength. Without the band-pass filter the optical power is high, peaking at a shorter wavelength (blue colour).

The band-pass filter efficiently blocked the UV, blue, and red lights, allowing through almost without any loss, the portion of the spectrum around 500 nm (as desired). The ratio of the areas of the two spectrums is also 10:1, which causes the 10 times power

decrease mentioned above during the characterization of the imager. This is because the green band-pass filter cuts out the whole spectrum outside the green region, which means that the optical power in that region is blocked. This does not mean that the green band-pass filter reduces the power in the green region, because as the inset shows, the peak of the signal in the green region with the filter is the same as the peak of the signal in the same region without the filter. Note that in both cases, the power at the surface of the imager is a linear function of the incident power to the optical system. In addition, the peak of the UV light from the light emitting diodes, which managed to escape the long-pass filter, was also efficiently further attenuated by the green band-pass filter around 100 times.

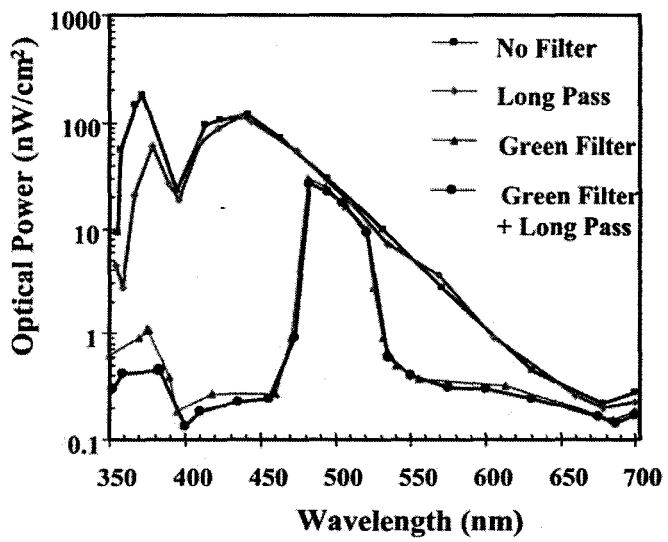

Figure 4.17: Performance of the long-pass and band-pass filters

Another experiment was carried out, and this time the spectrum of the light reaching the photo-detector was examined to determine the significance of using a long-pass filter in addition to the band-pass green filter to further suppress the UV light that might be reflected onto the CCD imager. Figure 4.17 shows the spectra obtained for the 4 different cases: with no filter in front of the optics, with only a green filter, with only a long-pass filter, and with both filters. The results showed that in the values closer to 350

nm, the long –pass filter managed to suppress the UV light only around 3 times, with or without the green filter. It also showed that the green band-pass filter had the bigger role in suppressing the UV light. However, we can clearly see that having a long-pass filter does help in suppressing the UV light even further, but another long-pass filter might be needed in the future with better blocking capabilities in the 350 – 400 nm region. The ratios of the signal at around 370 nm with the different filter combinations as compared to the signal when no filters were used are as follows:

- With long-pass filter: 3.3:1
- With green-pass filter: 200:1
- With long-pass filter and green-pass filter: 500:1

The long-pass filter transmittance data is shown in Figure 4.18. The graph is in semi-log scale. We can see that at 380 nm, the transmittance is still 50%, and at 370 nm (which falls under the FWHM bandwidth of the UV LEDs), almost 30% of the UV light is still transmitted past the long-pass filter.

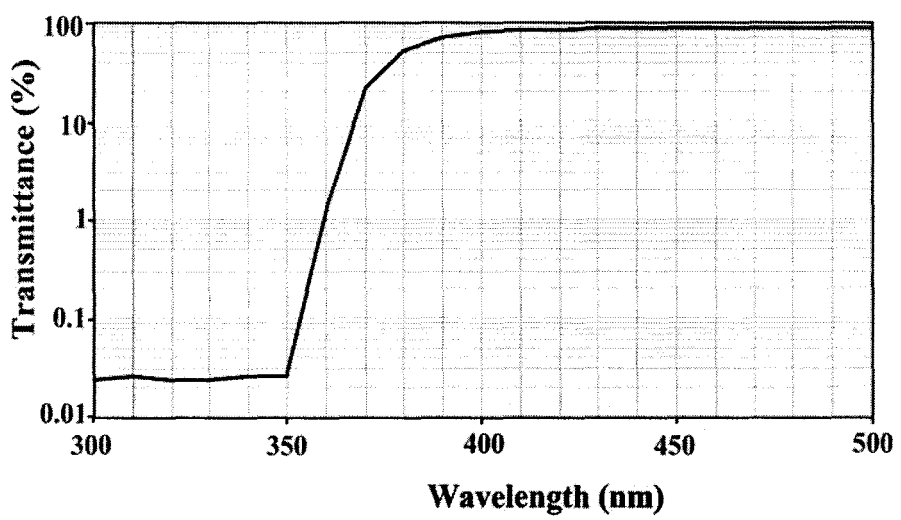

Figure 4.18: Transmittance of the long-pass filter

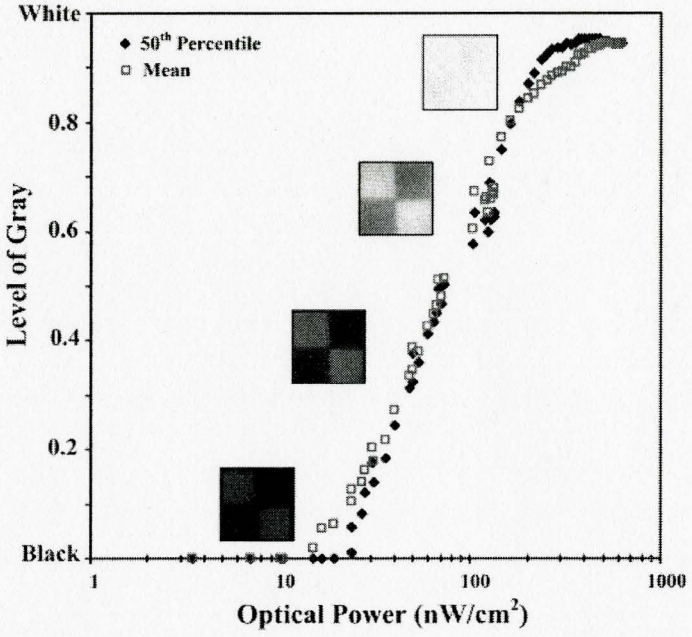

Figure 4.19: The mean and 50th percentile of the pixels in terms of level of gray

Sensitivity

Figure 4.19 shows the brightness of the pixels in the acquired images vs. the optical power incident to the surface of the imager. When the power is low (e.g. < 10 nW/cm^2), the image is dark, and most of the pixels are with gray level close to the level 0 of black. As we increase the incident power above 12 nW/cm^2, the average level of gray, shown as open squares in the figure, starts increasing above 0, and the image itself becomes brighter. The overall brightness of the image can also be characterized by the median of the distribution of the pixels, over the level of gray. The median is the 50th percentile of the distribution, and it is shown in the figure in solid diamonds. In the range for gray level from 0.2 to 0.8, the median and the mean overlap which is expected, since the target contains black and white squares of equal size. At high optical power, the imager saturates and all the pixels become close to level 1 (white). In the regions below 0.2 and above 0.8 where there is a difference between the mean and median, the images fade into black or white, respectively. Therefore, the difference between the mean and the median can be used as the criterion for controlling the electronic shutter speed or

illumination level such that the image is brought to the region within which the imager provides the best contrast.

An important observation is that the behavior of the level of gray as a function of the optical power is independent of the spectrum of light. The data points in the figure were obtained from two experiments carried out with and without a green band-pass filter, (see again the inset in Figure 4.16) and the data from these experiments overlap so well, such that the different experiments cannot be distinguished. This is advantageous for fluorescence imaging, in which spectral separation is essential.

From Figure 4.19, we observe that the saturation of the white level occurs at illumination about 220 nW/cm^2. The gain in the signal path from the CCD to the output of the imaging system is 8.25 at high signals, and the saturation voltage at the output of the imaging system is around 700 mV. Therefore, the maximum output signal from the CCD before saturation is around 85 mV. The sensitivity of the CCD imager as provided by the manufacturer's datasheet is 450 mV. It was measured using a pattern box as a subject (luminance: 706cd/m^2), and using a testing standard lens as an IR cut filter and image at F8 (the ratio between the lens focal length and the diameter of the entrance pupil on a log scale). The luminous intensity to the sensor receiving surface at this point is defined as the standard sensitivity testing luminous intensity. The electronic shutter speed was set to 1/250 seconds, and the signal output at the center of the screen was measured, and substituted in the formula:

$$S = V_s \times \frac{250}{60} \text{mV} \tag{4.1}$$

It is not clear how this figure represents sensitivity, which is normally represented in mV/nWcm^{-2}. However, the sensitivity of this CCD was measured by a Russian group [100] and given as 57 mV/lx. But 1 lx is equivalent to 150 nW/cm^2; this means that the sensitivity in mV/nWcm^{-2} is 0.38 mV/nWcm^{-2}. They also reported that the minimum detectable signal of the CCD is 0.0138 lx (or 2.07 nW/cm^2), and the maximum detectable signal was also calculated to be 13.8 lx (or 2070 nW/cm^2) [100]. This means that the dynamic range (DR) of the CCD is 1000, or 60 dB. The minimum detected signal with our complete system at the given distances and optical system specifications was around

10 nW/cm^2. Taking the uncertainty in the calculated number reported in [100], and the noise in the output signal of the CCD, the two numbers (2.07 and 10 nW/cm^2) are in the same order. Using the reported sensitivity of the CCD, we see that the saturation optical power is 85 mV/(0.38 mV/nWcm^{-2}) ~ 223 nW/cm^2, which agrees with the aforementioned observed saturation of 220 nW/cm^2. Targeting sensitivity at low illumination levels by adding the gain of 8.25 resulted in that the bottom tenth of the full dynamic range of the CCD is being used in the imaging system, to allow for better detection of the small signals, at the expense of losing the upper part at high illumination intensities. Additional details about the dependence of the level of gray as a function of the optical power are provided in the next figure.

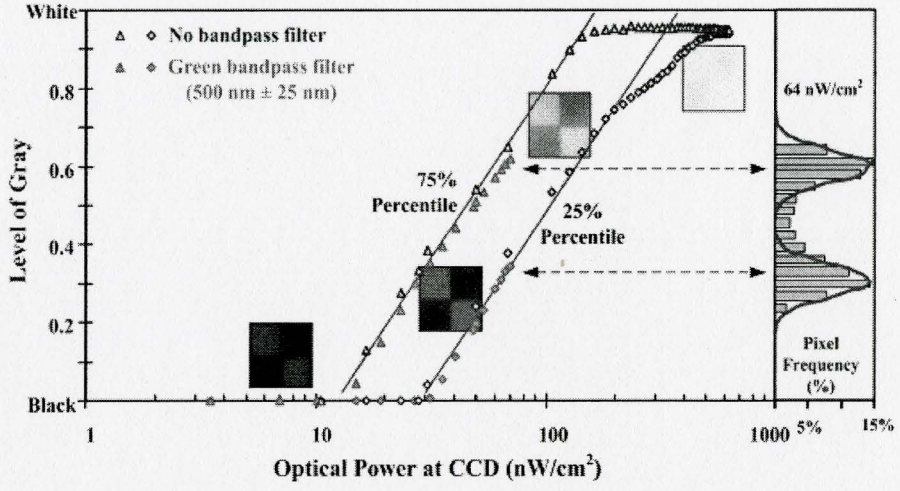

Figure 4.20: Distribution of pixels within the image in terms of level of gray

Figure 4.20 shows the distribution of pixels vs. the optical power incident to the CCD, in terms of the 25th and 75th percentiles. The histogram on the right shows that the 25th percentile is related to the dark pixels in the image, while the 75th percentile is related to the bright pixels in the image. The lines in this histogram represent fitted normal distributions with averages equal to the percentile values. The histogram is for the distribution of the level of gray of the pixels (left hand axis) at optical power 64 nW/cm^2, when the green band-pass filter is used. The measured standard deviation of the normal distribution is σ_m = 4.2%, which can be attributed to dispersion of the levels of gray, both

from the target and fixed pattern noise, and random noise from the imager. By specification [72], the CCD imager has flicker noise of σ_f = 4%, when one tenth of the dynamic range of the imager is used. The quantization noise from the A/D converter of the image acquisition board can be calculated from the signal-to-noise ratio (*SNR*), given by:

$$SNR = 1.76 + 6.02n\,, \tag{4.1}$$

where *SNR* is in dB, and n is the number of bits of the A/D converter. We have used an 8-bit A/D converter, and since the range of the levels of gray R=1–0=1, then, using equation (4.1), the quantization noise σ_q is:

$$\sigma_q = R \times 10^{\left(-\frac{1.76dB+6.02n}{20dB}\right)} = 1 \times 10^{\left(-\frac{1.76+6.02\times 8}{20}\right)} = 0.3\%\,. \tag{4.2}$$

Therefore, the standard deviation σ, excluding the fixed pattern noise and random noise from the imager and from quantization, is:

$$\sigma = \sqrt{\sigma_m^2 - \sigma_q^2 - \sigma_f^2} = \sqrt{4.2^2 - 0.3^2 - 4^2} = 1.25\%\,. \tag{4.3}$$

The value of σ can be associated with pattern noise in the target and electrical noise. This value is less than the flicker noise from the imager, which suggests that the majority of the noise is due to the CCD imager, and this is because we are only using the bottom tenth of the full range of the CCD, by adding electrical gain in order to increase the sensitivity at low illumination levels. It would be preferable to use another CCD model, which has a higher sensitivity, but not as high a dynamic range. The other sources of noise which resulted in σ = 1.25% perhaps include: pattern noise in the target since it was printed using a laser printer; the placement of the UV filter after the focusing lens; and possible differential non-linearities in the acquisition board used. Further investigations are needed to identify the exact contribution from each of these noise sources.

Taking a closer look at the captured images of the target, some of which are shown in Figure 4.20, one can see a close relation between the contrast and clarity of the image and the evolution of the 25th and 75th percentiles. When the difference in the gray levels of the percentiles is large, then one can clearly distinguish between the white and black areas. However, when the difference in the gray levels of the percentiles is small, either at low optical power or at high optical power, the objects in the images disappear (towards black at low optical power and white at high optical powers). Note that the presence of the green band-pass filter does not change the difference between the percentiles. In other words, it does not affect the ability to distinguish between two different levels of gray, which means that the autofluorescence from the objects, which falls in the spectrum of the green band-pass filter, will be distinguished reliably. For this particular CCD, the average optical power from the targets should be in the range between 30 and 130 nW/cm^2 at the imager surface, in order to maintain a constant difference between the percentiles.

The Measured Dynamic Range of the CCD

The dynamic range of the CCD was measured at the chip, before the signal goes into the signal processing chip and the image acquisition board. However, due to high read-out noise in the pixels, (which is later removed by the signal processing chip), it was hard to distinguish the actual signal from the noise, and estimates had to be made. The lowest signal that was measured at the chip was close to 4 nW/cm^2, and the illumination was changed gradually until it became very hard to distinguish the signal from the read-out noise, and reasonable estimates of the signal could not be made. The illumination level at which there was still a change in the signal voltage was around 500 nW/cm^2. This puts the measured dynamic range of the CCD at $=\left(20\log\frac{500}{4}\right)=$ 42 dB. Another limitation in this measurement was the availability of an illumination source capable of achieving illumination levels at the target higher than 1000 nW/cm^2, and therefore no readings were taken there. The measurement data is shown in Figure 4.21.

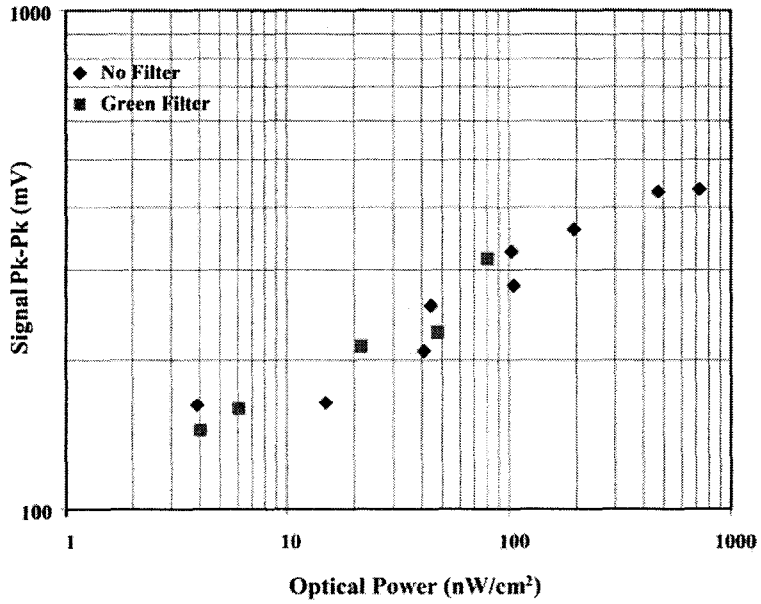

Figure 4.21: The measured dynamic range of the CCD

Modulation Transfer Function

The modulation transfer function (MTF) of the system was also measured. MTF is a spatial frequency parameter, and is defined as the ratio of the contrast of an image to the contrast of the target itself. This contrast is represented by the following formula:

$$Contrast = \frac{L_{\max} - L_{\min}}{L_{\max} + L_{\min}}, \tag{4.4}$$

where L_{max} and L_{min} are the maximum and minimum measured intensities of an image respectively. Contrast is also sometimes referred to as the modulation (M) of the image or target. Therefore if the image modulation is M_i and the target modulation is M_o, then the modulation transfer function would be [101]:

$$MTF = \frac{M_i}{M_o}. \tag{4.5}$$

In our measurement, the sinusoidal pattern target that was used is shown in Figure 4.22. The target contains 15 different spatial frequencies (line pairs per mm).

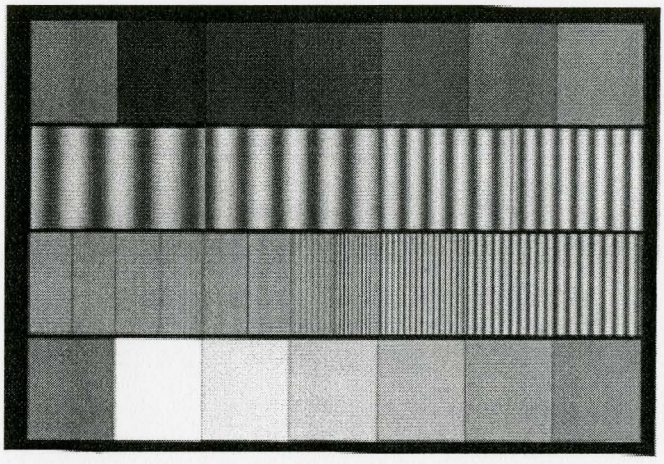

Figure 4.22: Sinusoidal MTF pattern chart

Table 4.1 shows these spatial frequencies and the target's corresponding M_o at the different frequencies [101]. The measurements were carried out under constant illumination conditions. The distance of the target from the imager was adjusted such that the target covers the whole image, and the image was saved. A Matlab code was developed to calculate the average sinusoidal profiles of the pixel intensities at the different frequency regions, and the minima and maxima of these profiles were used in equation 4.4 to calculate the contrast in every region. The contrasts were plugged into equation 4.5 to calculate the modulation transfer function. The same procedure was repeated for different illumination levels, and the results are shown in Figure 4.23

Table 4.1: The spatial frequencies of the 16 different regions in the sinusoidal MTF chart

	Spatial frequency (lp/mm)	M_o		Spatial frequency (lp/mm)	M_o
1.	0.1875	0.446	**9.**	3	0.117
2.	0.25	0.433	**10.**	4	0.081
3.	0.375	0.449	**11.**	5	0.077
4.	0.5	0.433	**12.**	6	0.103
5.	0.75	0.395	**13.**	8	0.0591
6.	1	0.377	**14.**	10	0.053
7.	1.5	0.305	**15.**	12	0.046
8.	2	0.252			

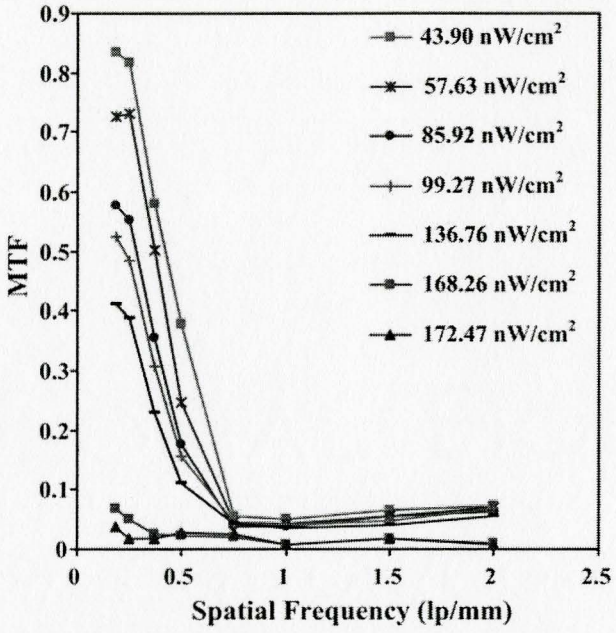

Figure 4.23: Modulation transfer function at different illumination levels

Two observations can be made by looking at Figure 4.23. The modulation transfer function decreases when the illumination level is increased due to a decrease in the contrast level between black and white as the light intensity on the target is increased. However, the modulation transfer function under all illumination levels decreased significantly between 0.25 lp/mm and 2 lp/mm, after which the data becomes not reliable enough to be considered. High experimental error in this experiment arises from the quality of the target pattern, which was printed out on regular paper using a regular laser printer. When the modulation in the printed target was compared to that of the original image (Figure 4.24), it was obvious that much of the contrast was lost in the printing. This is why in Figure 4.23 all the points converge rapidly to the same MTF value for different power levels, indicating a limitation imposed by the printing quality. In the future, it is recommended to use a reflection card with the same pattern on it (Edmund Scientific, No. 54-804) [101]. Also, once the standard target is obtained and the measurement is repeated, it is recommended to obtain the MTF of the unwrapped images in the same manner, and to study the deterioration of the spatial resolution of the

unwrapped images as we move closer towards of the apex of the mirror. In the future, this may lead to using the area for a forward imaging channel.

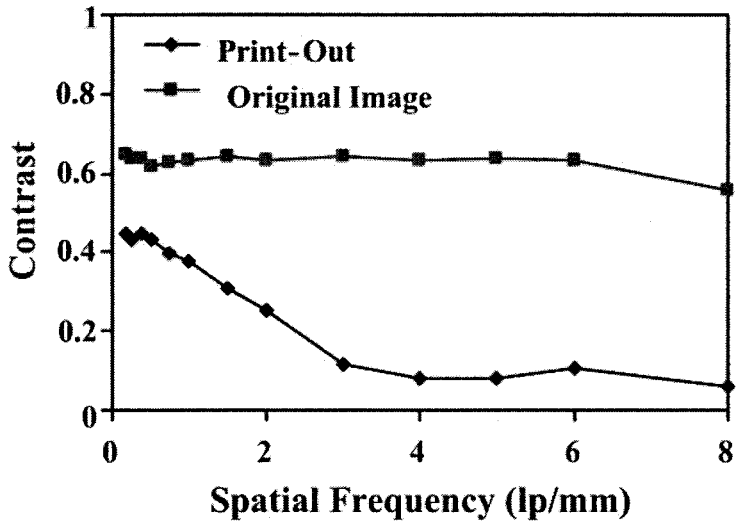

Figure 4.24: Contrast in the printed-out target

Quantum Efficiency (QE) and Charge Transfer Efficiency (CTE)

The quantum efficiency (QE) is an important characteristic of imaging devices. It is a measure of the device's electrical sensitivity to light. It is measured over a range of wavelengths to determine the device's efficiency at different photon energies. This quantity can be obtained in absolute numbers if the photocurrent I of the device can be measured. The following formula can be used:

$$\eta = \frac{I \times h \times c}{P \times q \times \lambda}, \tag{4.6}$$

where h is Planck's constant, c is the speed of light, P is the optical power, and q is the electron charge. In our CCD, the only output is an analog voltage signal, which has undergone multiplexing and amplification at unknown levels, since the internal architecture of the CCD was not provided by the manufacturer. However, from the relative responsivity R of the CCD (which is given in Figure 3.10), we can calculate the relative quantum efficiency η according to the following formula:

$$\eta = \frac{R \times h \times c}{q \times \lambda} \tag{4.7}$$

Another important characteristic is the charge transfer efficiency, which is a measure of the amount of charge that is transferred between the pixels of the CCD. When the image is taken, the charge is transferred onto a horizontal row, and then the pixels are transferred along the horizontal row towards the output node, where they are digitized and transferred to the outside of the CCD. As the charge is being transferred, some electrons will be left behind in the pixel wells, and this causes a drop in the charge. A CTE of 0.99995 is typical. Having no access to the pixel wells, and no information from the manufacturer about this, measuring the CTE was also not possible.

Proof-of-Concept Tests

Proof-of-concept tests were also conducted on the completed endoscopic fluorescence imaging system using fluorescent phantoms; however, visible light images were taken first to prove the functionality of the imager as a regular black and white video camera. Figure 4.25 shows two screen shots of small text found on Canadian money bills.

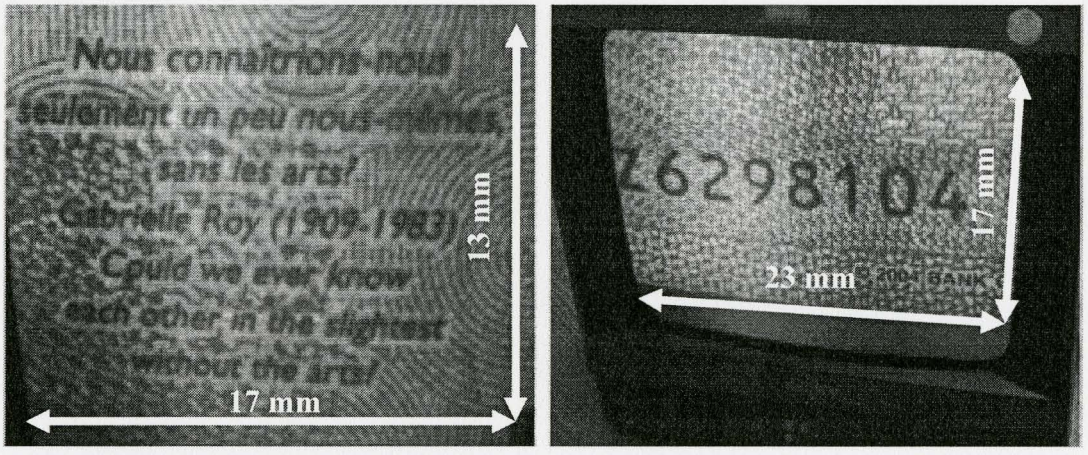

Figure 4.25: White light video images captured by our imager

Figure 4.26 shows pictures of fluorescence due to fluorescent dyes administered to regular paper. These pictures were taken using the second prototype with the extra

chip, and captured using the acquisition board, and we can see that the vertical black lines are much less significant than they appeared in the picture taken with the old prototype when the signal processing chip was not there. The left series is of a red dye spot administered to a piece of paper, with a red filter in between the paper and the imager. The right series is of a green dye spot with a green filter instead. Both series were captured while moving the paper slowly under the imager. As we can see, different areas of the spots were captured with high sensitivity and high contrast, indicating that the device would still be able to detect natural autofluorescence signals from diseased tissue. It is also important to point out that the dark areas are areas that do not have a fluorescent dye administered to them, and are completely blocked out by the imager.

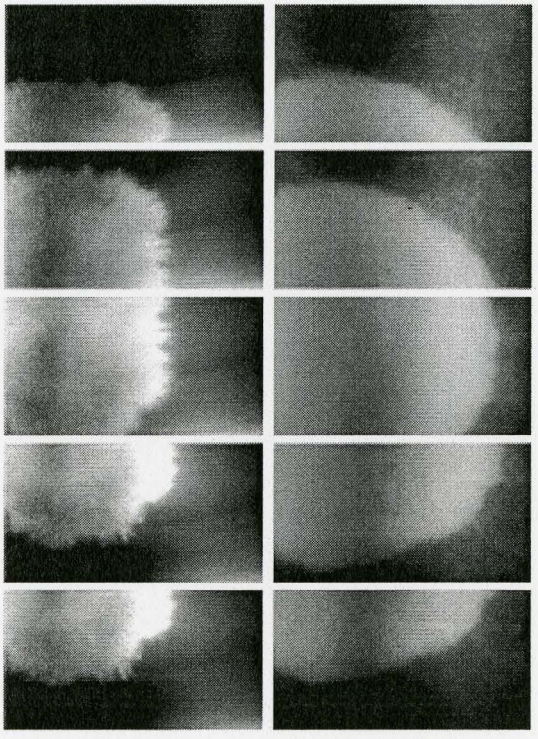

Figure 4.26: Red dye spots (left) and green dye spots (right) captured using our imager and the image acquisition board

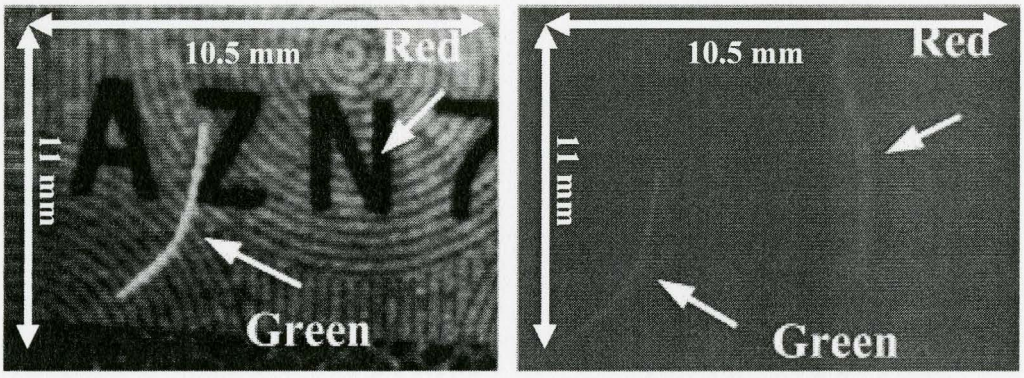

Figure 4.27: On the left, only the green line is visible under white light, but the red line is not. On the right, we can see that under UV excitation, and through a green band-pass filter, both lines are clearly visible. This demonstrates spectral selectivity.

Another experiment conducted on Canadian money bills containing text printed in black ink and two fluorescent lines (one green, one red). As shown in Figure 4.27 (left), when first illuminated by the white light without a bandwidth filter in front of the CCD, both the printed text and the green fluorescence mark were visible in the acquired image. When the UV LEDs were used as the illumination source along with a band-pass filter (600±40 nm), both the green and red fluorescence marks are visible, while the printed text is not, as shown in 4.26 (right). This test simulated lesions that are not visible under regular white-light endoscopic imaging, but can be detected using UV illumination and spectrally selected imaging i.e. blocking out the non-fluorescing areas.

Later on, a series of experiments were conducted and more images were captured. The experiments are detailed below:

Experiment 1: White light/red dye/no filter: A small piece of white paper was marked with the letter 'R' and a small amount of red dye was placed on top of the mark. White light was used for illumination first with no band-pass filter placed between the paper and the imager. Upon illumination, the reflection from the dye was obvious to the bare eye. The paper was viewed

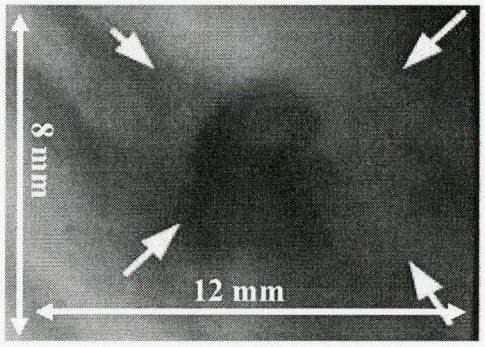

Figure 4.28: White light/red dye/no filter/pig skin

with the CCD imager, and a picture was taken (Figure 4.28).

Experiment 2: UV excitation/red dye/red filter: A red band-pass filter (Brightline 692 nm) was placed in between, and the white light was replaced with UV light using UV LEDs. When the UV LEDs were turned on, red light fluorescence was obvious to the bare eye, and bright fluorescence was detected on the CCD imager. A picture was taken (Figure 4.29).

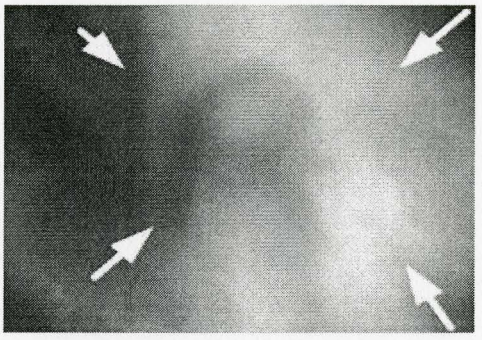

Figure 4.29: UV excitation/red dye/red filter/pig skin

Experiment 3: White light/green dye/no filter: A small piece of white paper was marked with the letter 'G' and a small amount of green dye was placed beside the mark. White light was used for illumination first with no band-pass filter placed between the paper and the imager. Upon illumination, the reflection from the dye was obvious to the bare eye. The paper was viewed with the CCD imager, and a picture was taken (Figure 4.30).

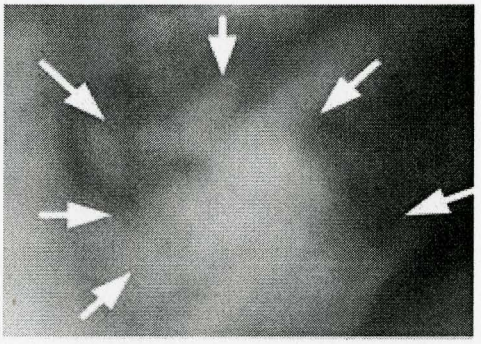

Figure 4.30: White light/green dye/no filter/pig skin

Experiment 4: UV excitation/green dye/green filter: A green band-pass filter (Thorlabs 500-40 nm) was placed in between, and the white light was replaced with UV light using UV LEDs. When the UV LEDs were turned on, green light fluorescence was obvious to the bare eye, and bright fluorescence was detected on the CCD imager. A picture was taken (Figure 4.31).

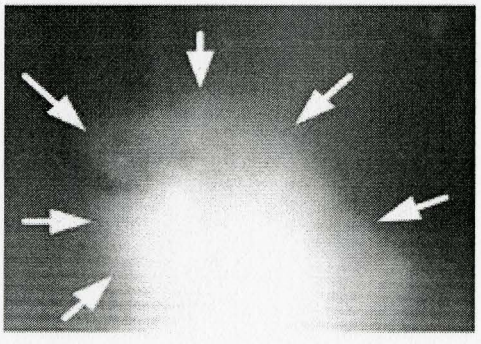

Figure 4.31: UV excitation/green dye/green filter/pig skin

Experiment 5: White light/red dye/no filter: A small amount of red dye was placed on a small pig skin sample. White light was used for illumination first with no band-pass filter placed between the skin and the imager. Upon illumination, the reflection from the dye was obvious to the bare eye. The paper was viewed with the CCD imager, and a picture was taken (Figure 4.32).

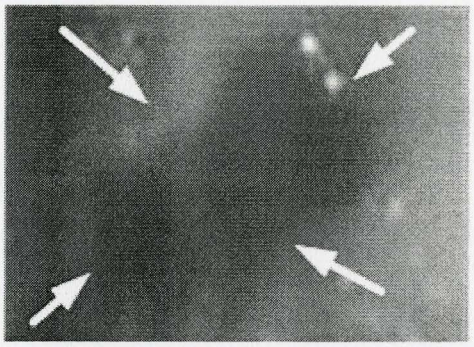

Figure 4.32: White light/red dye/no filter

Experiment 6: UV excitation/red dye/red filter: A red band-pass filter (Brightline 692 nm) was placed in between, and the white light was replaced with UV light using UV LEDs. When the UV LEDs were turned on, red light fluorescence was obvious to the bare eye, and bright fluorescence was detected on the CCD imager. A picture was taken (Figure 4.33).

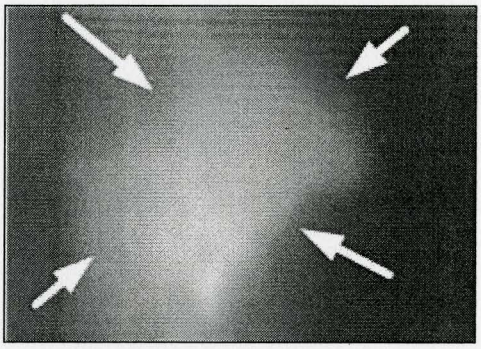

Figure 4.33: UV excitation/red dye/red filter

Experiment 7: White light/green dye/no filter: A small amount of green dye was placed on a small pig skin sample. White light was used for illumination first with no band-pass filter placed between the skin and the imager. Upon illumination, the reflection from the dye was obvious to the bare eye. The skin sample was viewed with the CCD imager, and a picture was taken (Figure 4.34).

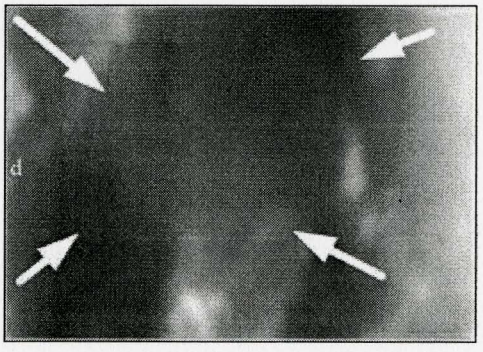

Figure 4.34: White light/green dye/no filter

Experiment 8: UV excitation/green dye/green filter: A green band-pass filter (Thorlabs 500-40 nm) was placed in between, and the white light was replaced with UV light using UV LEDs. When the UV LEDs was turned on, green light fluorescence was obvious to the bare eye. However, the fluorescence was barely detected by the CCD imager even though green fluorescence could be viewed clearly with the bare eye. This could be due to the use of the wrong filter. Different filters with different spectra should be used, and the spectrum of the used filter should be verified. A picture was taken (Figure 4.35).

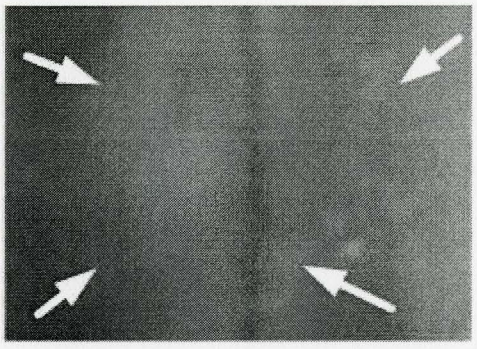

Figure 4.35: UV excitation/green dye/green filter

The last 4 experiments demonstrate that this system can selectively detect features that are only available in a particular spectral band. Note that in the pictures of excited tissue before the filters were inserted, you can see all the details of the tissue around the fluorescent spot, whereas the pictures showing the same excited tissue after the filters were inserted do not show the details around the fluorescent spots, and the only parts that are visible are the areas that are stained with fluorescent dyes.

4.4 Time-Resolved Measurement Limitations of the System

This experiment was carried out to show the limitations of our CCD for measurements that require high time resolving capabilities. A light pulse of 500 μs with a duty cycle of 50% was used to illuminate the target. The shutter speed of the CCD was set to 1/5000, or 200 μs, and the offset between the two signals (the light pulse and the shutter window) was varied. Figure 4.36 shows the time offset between the two pulses on the x-axis, and the total overlap time between the pulses on the y-axis.

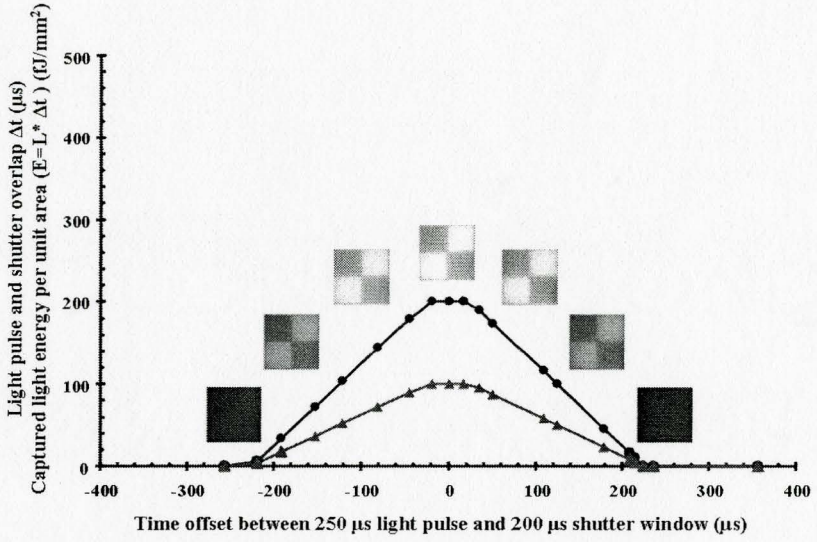

Figure 4.36: Speed limitation of the imaging system

At the time when the offset between the two pulses is zero, the overlap is at a maximum, which is limited by the smaller pulse (in this case it is the shutter speed 200 μs). As the offset increases, the overlap remains constant for a period equal to half the difference between the two pulses, and then starts dropping linearly until the offset is equal to 225 μs. What is interesting to notice in this graph is that the overlap drops linearly with the offset, and not until about 210μs does the overlap deviate from that linearity. This is the time at which the shutter is being turned on or off, which is usually the time that is taken by the reset signals and the discharge of the capacitors. The other line in the graph shows the total amount of energy captured by the CCD for different offsets. This curve follows the other curve closely, and shows that the CCD can resolve down to one tenth of the maximum energy it can resolve. In other words, the peak of that curve is at 100 fJ/mm^2, and the minimum amount of energy the CCD can still resolve when the overlap is at a minimum is less than 10 fJ/mm^2.

Despite the fact that these results show that the CCD is limited by its shutter speed, or more precisely by the time it takes the shutter to be completely opened or closed (10μs), this limitation appears only in the range below a few tens of microseconds.

For applications in which we are not only interested in the localization of specific fluorophores, but also in the local fluorophore environment, time-domain technologies

such as fluorescence lifetime imaging (FLIM) can be used. This technology provides high sensitivity information about the contrast between different types of states of biological tissues. It is also relatively insensitive to intensity artifact such as variations in fluorophore concentrations and or excitation intensities or variations in fluorescence collection efficiency [102]. The fluorescence lifetime can be measured in the frequency domain by measuring the phase shift in the fluorescence signal due to the excitation by a high-frequency pulsed source, or it can be measured in the time-domain using time correlated single photon counting (TCSPC) for point-scanning applications, or time-gated imaging for wide-field applications such as endoscopy [103].

The time-gated wide-field applications utilize high-speed gated multichannel plate photomultipliers (MCP-PMT) and intensified charge-coupled device (ICCD) cameras. These high-speed devices are capable of resolving fluorescence lifetimes in the order of a few hundred picoseconds, and up to a few milliseconds [104]. ICCDs for example, use a photocathode, a micro-channel plate and a phosphor screen, all mounted in front of the CCD to accelerate and multiply photoelectrons towards the phosphor screen which reproduces photons that are guided towards the CCD. If the control voltage between the photocathode and the micro-channel plate is reversed, the acceleration of the electrons stops, and therefore no photons reach the CCD. This, conveniently, acts as a shutter, which can have very high speeds, sometimes in the order of a 200 picoseconds.

Though implemented endoscopicly, the incorporation of such devices in a pill-based system is still difficult, due to the size-limitation within a pill. PMT-MCPs have shown limitations in terms of size, robustness, and power consumption. ICCD on the other hand, though more promising, have also shown limitations in terms of cost, heat generation, and bulkiness and until now are still not suited for capsule-based applications [105].

4.5 The Wireless Transmission Module Results

The wireless transmission module was tested and proved to be working as expected. The restrictions on device size and power consumption were at the focus of the experiments. These restrictions require innovative approaches for image compression and

wide-band short-range RF transmission in order to overcome several downsides. In order to transmit the images in real time, data compression has to be performed. However, it is well established that image compression by a factor larger than 2 would result in significant loss of image quality [73]. Compression algorithms also require extensive computation usually accompanied with increased power consumption [74], which is not desirable for a wireless device. To gain insight for the trade-off between compression and quality, we have employed differential variable length coding in the image compression, and then, we changed the image targets so that the effective level of compression also changes. The results are shown in Figure 4.37. It is interesting to observe that the trend shown in Figure 4.36 is the opposite of what one would naturally expect. In particular, the image quality decreases when the data compression is lower and the average length of the code word is longer, whereas the quality increases when the code words are shorter and the data compression rate is higher. Intuitively, one may expect the opposite: low quality at high compression and vice versa.

The compression scheme used relies on the differences between consecutive pixels to calculate the average bit length per byte, and therefore the amount of compression differs between images depending on the uniformity (or non-uniformity) of the image. Images of high uniformity yield a smaller bit length per byte. In that case, the fact that less data is available for transmission reduces the losses in the RF link that are due to the overwriting of some data when the RF link is sending at a slower rate than its buffers are receiving. For non-uniform images, the bit length per compression byte is larger, sending larger amounts of data to the RF link, causing more overwriting of data and therefore larger losses. It is important to note here that the RF link's bit error rate during transmission is only $< 0.1\%$, and that should not be confused with the losses in the RF link before transmission. Therefore, we conclude that this inverse relation we experience is due to losses in the RF link before transmission, due to varying compression rates.

This inverse dependence between transmitted image quality and data compression rate is a typical artifact for wireless image systems, in which the data transfer rate is

limited by the RF link. Thus, the image compression in these systems is chosen such that the RF link would not be overloaded. In commercial systems, compression schemes were chosen after a tough decision in the trade-off between image quality, power consumption and loss of information in the RF link. Due to scattering of both excitation and emission photons, wide-field fluorescence imaging on the tissue level usually has relatively low spatial resolution compared to conventional imaging. Therefore, on-chip hardware binning of the imager pixels may significantly reduce the requirement for data compression. Further investigation via *in vitro* testing on phantoms or on *ex vivo* tissue are therefore required to quantitatively determine these tradeoffs.

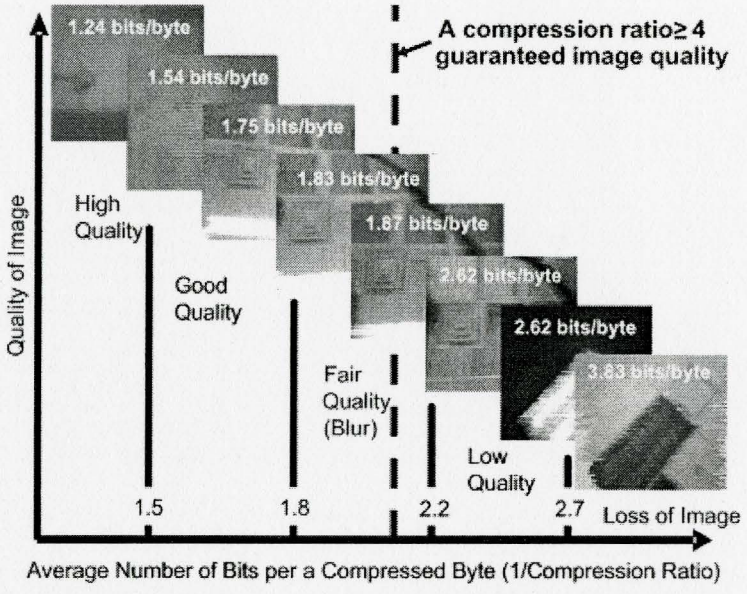

Figure 4.37: Dependence of image quality on the average length of the code words used in image compression. The tradeoff between compression and image quality is reversed in wireless systems with limited bandwidth

Chapter 5

CONCLUSIONS AND RECOMMENDATIONS

5.1 Conclusions

Fluorescence-imaging-based wireless endoscopy has two main advantages over current catheter-based techniques for screening and diagnostic applications in the gastrointestinal tract. Firstly, it is non-invasive and does not need to be administrated by a specialist. Secondly, the functional diagnostic information provided by a fluorescence signal may enable automated artificial intelligence programs to process the large amount of images acquired during the 7-8 hour period.

In this thesis work, we developed a diagnostic fluorescence imaging system prototype for non-invasive wireless encapsulated GI endoscopy. The prototype contains three modules which were first developed and tested individually and then tested together. Off-the-shelf components were used to build the electronic imaging system based on a CCD imager, and capable of feeding out a standard (EIA) video signal at a resolution of 768 x 494 pixels, and a frame rate of 30 frames/s, with the imager, timing controller, and signal processing chips dissipating around 200 mW combined. The system was designed and assembled on a small (25 mm x 11 mm) PCB board to demonstrate the capability of miniaturization.

The optical set-up was also designed using off-the-shelf components, including a pair of focusing lenses (3/1 object-to-image focal length, 0-2 mm variable diameter aperture), a UV filter (380 nm), colour filters, and a cone mirror. The use of the cone mirror was so that the areas surrounding the device can also be viewed to complement forward channel imaging. The images obtained with such a technique are usually spatially distorted, but can be unwrapped and this has also been demonstrated. A number

of high power UV LEDs (365 nm) were used as illumination sources, and their performance in terms of optical power was characterized.

The optical and electronic imaging modules were later combined, and initial characterization and proof-of-principle testing on fluorescent phantoms have demonstrated that even at low illumination levels, the device is capable of acquiring and analyzing fluorescence images at different spectral bands, with little decrease in optical intensity due to the insertion of colour filters. This is particularly important in diagnostic devices, since different diseases or even the same disease at different stages can have different fluorescence behaviors. The system also targets low level illumination signals, amplifying the signal obtained from the CCD, thus utilizing the bottom tenth of the dynamic range of the CCD for better detection of small signals, and performing best in the range between 30 nW/cm^2 and 130 nW/cm^2.

As for the wireless transmitter module, it was demonstrated that the images can be reduced to about 10-12 kBytes, allowing for the addition of correction codes and other useful information while keeping the data volume under 100 Kbits/frame. The data from the compressed images are combined, and then the data is fed to the RF transmitter at a rate of 250 kbps, and the RF link forwards the data to a host computer with an acceptable data loss of 10%, which can be recovered. The power consumption of the module was also sufficiently low, allowing it to operate fully using two 1.5 V batteries.

Although it is a compact system (~ 2.5 cm in diameter and ~ 11 cm in length), the integrated prototype is still too large to be practical. Further miniaturization towards a practical prototype may be achieved through the use of customized electrical components, such as integrated imaging acquisition and wireless communication ICs. As for the optical module, miniaturization of the individual components as well as the overall system size can be more challenging.

Despite the limitations that accompany this design, it is nevertheless the result of a tremendous effort towards the design of a miniaturized, capsule-based, minimally-invasive device with fluorescence imaging capabilities. Moreover, we were able to identify a number of issues and areas of research that must be considered for the

realization of a small-size fluorescence imaging capsule, and a number of them are discussed next. This work resulted in a publication in the IEEE Journal of Selected Topics in Quantum Electronics (January/February 2008) [75].

5.2 Recommendations and Future Work

The acquisition of spectrally resolved fluorescence images requires complex and usually bulky optical and electronic instrumentation. To design a wireless system that can be used for GI tract diagnosis, the main challenges include the miniaturization of both optical and electronic components as well as the minimization of power consumption. All of the optical and electronic parts that were used to build the prototype are commercially-available, off-the-shelf components.

5.2.1 Confocal Microscopy

Research has to be conducted in many areas in support of the concept of endoscopic imaging. Recently, confocal imaging is being considered for such applications. This technique utilizes a laser that is focused to a single point in a microscopic field-of-view. The light is focused through a pinhole onto a detector. The name refers to the pinhole and the point of illumination being 'confocal' with each other. This technique is useful for diminutive lesions or microscopic abnormalities in the middle of a large area of diffuse disease. Any other light coming from the areas that are not focused onto the pinhole is rejected, while the focused spot traverses a line rapidly from left to right, and the line is swept top to bottom across a microscopic field. The signals are digitized and the result is a set of two-dimensional microscopic images, or "optical sections", each representing a focal plane within the specimen [76].

A plan has been outlined to miniaturize confocal microscopes to be able to perform this technique *in vivo*, but so far limited performance has been demonstrated, mainly due to technical limitations related to the miniaturization approaches that were considered. Confocal microscopy can provide images with high resolution and contrast, sufficient to distinguish pit architecture as well as cellular and sub-cellular structures during examination. It is now possible to perform high-resolution, point-scanning

fluorescence confocal microscopy of the human GI tract by using a device that also meets the requirements for the conventional upper- and lower-GI endoscopy [76].

5.2.2 Spectral Imaging Techniques

Another hot area of research is spectral selectivity. Efficient tunable spectral selection for the whole field is highly desired, but would be very difficult to miniaturize for the current band-pass filter based system. Therefore, advanced multi-spectral imaging technologies need to be investigated such as acousto-optic tunable (AOTF) filters and/or liquid crystal tunable filters. An AOTF device is a solid-state electro-optic device that operates on the principle of acousto-optic diffraction in an anisotropic medium. It consists of a bifringent crystal onto which a piezoelectric transducer (PZT) is bonded. When an RF signal is applied to the PZT, an acoustic wave travels across the crystal and interacts with the incident optical beam. At a fixed RF frequency, only a narrow band of optical wavelengths is diffracted. This achieves high spectral resolution, fast response time, and variable filtering efficiency. Interest in AOTF for multi-spectral imaging is more recent [77]. Diffracted light is spatially separated from any non-diffracted light. The low signal-to-noise ratio, allows better detection of extremely low fluorescence signals. Efficiency and bandwidth of the filter can be dynamically tuned, allowing active gain and bandwidth adjustment as a function of wavelength or fluorescence intensity. Multiple filtering windows can also be opened simultaneously when emissions from different wavelength bands are summed directly on the image detector.

5.2.3 Imaging Options

In our current design, a CCD imager was chosen for its superior sensitivity and dynamic range. However, since only one tenth of the dynamic range of our imager was used, the future choice of imager should consider the use of a higher sensitivity imager, such as the TC-241, manufactured by Texas Instruments Inc. which has higher sensitivity with a narrower dynamic range. Also, in future development, CMOS imagers, which consume significantly less power than CCD imagers, may become an inevitable alternative. CMOS technology has significant advantages over CCD technology in its

ability to accommodate amplifiers, and noise-correction and digitization circuits, such that the chip has direct digital outputs, reducing the need for off-chip circuitry and the overall device size and power consumption. Additionally, CMOS imaging devices have a separate charge-to-voltage conversion node for every pixel, adding to the pixels' flexibility, but coming at the expense of losing chip area for light capture, and therefore inferior quality when compared to CCD imagers. In an active-pixel sensor based imaging system, a major problem is that they cannot simultaneously offer high sensitivity or a high signal-to-noise ratio (SNR) and high speed. This is an important issue, especially when dealing with incident light power of $1nW/cm^2$ or less, where integration times in the order of seconds may be required. For applications such as fluorescence endoscopy, where high sensitivity and high speed are required, alternative solutions should be developed. Colleagues in our team are proposing avalanche photodiodes (APDs) [78] in an array format as an alternative, and are planning to fabricate an APD with its periphery circuits in 0.18μm CMOS. They are also making an array of DC level mode active pixel sensors [79, 80]. The array will be 16 × 16, with 40 μm × 40 μm pixels and a fill-factor of 45%. These can be viable solutions for low-light-level imaging systems.

5.2.4 Image Processing

On another level, particular attention should be devoted to data acquisition and image recognition algorithms for "smart diagnosis". With the rapid advancement of capsule endoscopy, it is crucial to find new methods to perform image compression to limit the bandwidth needed to transfer the video images to the outside of the body, since traditional compression techniques are not suitable for such applications. A number of compression methods have been proposed since, one of which will be discussed below. Several issues have to be kept in mind in regards to any compression technique proposed or used. Power consumption should be kept at a minimum, and that can be guaranteed by adopting techniques that rely on the minimum amount of calculations. Also, clock frequency should follow pixel read frequency, keeping it as slow as acceptable, and keeping its driving voltage at a minimum. The compression should also meet the requirements of maximum transmission bandwidth allowed, and the amount of memory

available for the compression, since size is a big issue in capsule endoscopes. For example, 8-bit images can easily produce images in the range of 2.45 x 10^6 bits per image, and with data transmitters having a transmission rate of 1 Mb/s, an image that size would take up to 2 seconds to be transferred. However, if we want to transfer 10 images per second, to make the flow of images as close as possible to video, then a compression ratio of 20 is desired. Moreover, the compression should be kept flexible such that a trade-off between the number of transmitted images and image quality can be made as desired, allowing the physician to save power compressing images from areas that are not under investigation [81].

It was reported that endoscopists can tolerate significant compression of endoscopic images without loss of clinical image quality [81]. Based on a compression experiments performed on 24-bit color JPEG images, it was found that images can be compressed to between 31 to 99 times without significant loss of clinical image quality [81].

An image compression algorithm that is suitable for wireless capsule endoscopy was proposed by [83]. Image data de-correlation in the proposed algorithm is performed by the integer version of discrete cosine transform (DCT) [83, 84].

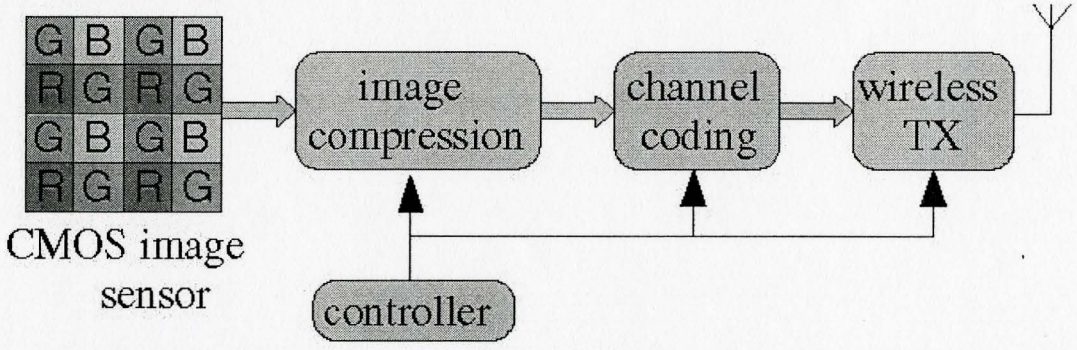

Figure 5.1: A simplified block diagram of a wireless endoscopy capsule data processing system [81]

The advantage of using this algorithm is that it requires the use of low complexity hardware, consumes little power, and can provide loss-less compression as well as high

quality lossy compression. Figure 5.1 shows a simplified block diagram of a wireless endoscopy capsule data processing system [81]. The output image data are transferred to the outside of the body using a wireless transceiver after compression and channel coding, and then they are stored and decompressed for diagnosis. The control over compression is provided by the control unit in the capsule, according to the commands it receives from the outer controller.

5.2.5 Miniaturization and Other Considerations

The realization of a miniaturized system has to start through the use of customized electrical components, using custom-designed integrated circuits in the electronic image acquisition and wireless transmission modules, which can be both combined into one chip [75].

However, miniaturization that can be applied to electronics cannot be applied in the same manner to optical imaging systems. This is mainly due to the fact that the spot size of an imaging system does not scale linearly with the size of the system. This imposes limitations on the maximum number of transmitted image pixels making them useless for many applications. The typical size of an optical imaging system in a micro-camera is usually 5 x 5 x 5 mm^3 which is still large compared to the imager sensor chip. The most promising approach nowadays is a combination of single lens systems forming a complete image by spatial or electronic superposition. This type of system is known as 'cluster' cameras [106]

Other problems that one may face on the path to miniaturization include the development of miniaturized power sources that can last for up to 7-8 hours or even longer. Internal light reflections within the dome of the capsule may also become a problem, generating too much heat over a smaller area, affecting the thermal stability of other components such as the electronic imaging components [107].

Eventually, different technologies have to be combined. However, simply putting several technologies together into one system makes the system very complex. The trick is to simplify and melt two parts that are in close proximity together into one, for example as we mentioned before with combining the electronic imaging system with the

wireless transmission system. But shrinking everything into smaller size and putting them together only adds to the complexity of the system [108].

The current device can be run on battery power. In practice, coupling power wirelessly from outside the body will most likely be required. Research on multimodality embedded sensor modules, such as temperature, pH, and ion-selective sensors, is also currently ongoing. In our group, methods of accurately locating the pill inside the GI tract remain to be a challenge in the field of capsule endoscopy [85], as well as innovative wireless transceiver designs that are custom designed for low power applications. Moreover, fabrication technologies for the practice of biomedical applications and environmental monitoring should be considered, as well as issues related to fabrication, integration, and manufacturability. Figure 5.2 is an illustration of what a future encapsulated fluorescence-based endoscopic spectrometer may look like.

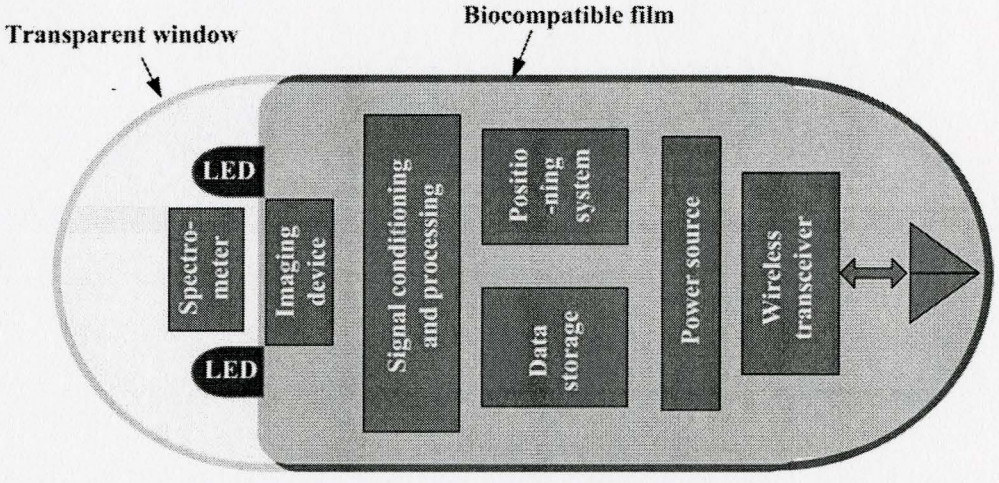

Figure 5.2: Concept of a miniaturized, multi-wavelength, fluorescence-based system

References

[1] http://www.answers.com/topic/gastrointestinal-cancer?cat=health

[2] M. B. Wallace, V. L. Durkalski, J. Vaughan, Y. Y. Palesch, E. D. Libby, P. S. Jowell, N. J. Nickl, S. M. Schutz, J. W. Leung, P. B. Cotton, "Age and alarm symptoms do not predict endoscopic findings among patients with dyspepsia: a multi-centre database study," *Gut* , 49:29-34, 2001.

[3] http://ntroi.stanford.edu/research/invivo.html

[4] http://www.temple.edu/temple_times/5-5-5/gidisorders.html

[5] M. Yu, "M2A(TM) capsule endoscopy: A breakthrough diagnostic tool for small intestine imaging," *Gastr. Nurs.* , 25(1):24-27, 2002.

[6] D. S. Mishkin, R. Chuttani, J. Croffie , J. DiSario, J. Liu, R. Shah, L. Somogyi, W. Tierney, L. M. Wong Kee Song and B. T. Petersen, "ASGE technology status evaluation report: wireless capsule endoscopy," *Gastrointestinal Endoscopy*, 63(4): 539-545 2006.

[7] K. Arshak, E. Jafer, G. Lyons, D. Morris, O. Korostynska, "A review of low-power wireless sensor microsystems for biomedical capsule diagnosis," *Microelec. Int.* 21(3): 8–19, 2004.

[8] E. A. Johannessen, L. Wang, C. Wyse, D. R. S. Cumming, and J. Cooper, "Biocompatibility of a lab-on-a-pill sensor in artificial gastrointestinal environments," *IEEE Trans. Biomed. Eng.*, 53(11): 2333-2340, 2006.

[9] C. Arens, T. Dreyer, H. Glanz and K. Malzahn, "Indirect autofluorescence laryngoscopy in the diagnosis of laryngeal cancer and its precursor lesions," European Archives of Oto-Rhino-Laryngology, 261(2): 71-76, 2004.

[10] B. Chwirot, S. Chwirot, W. Jedrzejczyk, M. Jackowski, A. Raczynska, J. Winczakiewicz, and J. Dobber, "Ultraviolet laser-induced fluorescence of human stomach tissues: Detection of cancer tissues by imaging techniques," *Lasers Surg. Med.*, vol. 21, pp. 149–158, 1998

[11] P. J. M. George, "Fluorescence bronchoscopy for the early detection of lung cancer," *Thorax*, 54:180-183, 1999.

[12] A. Bogaards, A. Varma, S. P. Collens, A. Lin, A. Giles, V. Yang, J. M. Bilbao, L. D. Lilge, P. J. Muller, and B. C. Wilson, "Increased brain tumor resection using fluorescence image guidance in a preclinical model," *Lasers. Surg. Med.* 35: 181-190, 2004.

[13] R. Richards-Kortum, E. Sevick-Muraca, "Quantitative Optical Spectroscopy for tissue diagnosis," *Annu. Rev. Phys. Chem.*, 47: 555-606, 1996.

[14] B. Jaggi, M. J. Deen and B. Palcic, "Solid State Microscope," *Canadian Patent* Serial Number 1,304,612 (7 July 1992).

[15] H. Zeng, A. Weiss, R. Cline and C. E. MacAulay, "Real-time endoscopic fluorescence imaging for early cancer detection in the gastrointestinal tract," *Bioimaging,* 6:151–165, 1998.

[16] H. Zeng, C. MacAulay, S. Lam and B. Palcic, "Light Induced Fluorescence Endoscopy (LIFE) Imaging System for Early Cancer Detection," Proc. *SPIE* vol. 3863.

[17] http://www.massgeneral.org/cancer/crr/types/gi/eso_gi.asp

[18] J. David Castle, "Digestive System 1: The Gastrointestinal Tract," Physiology/CTS, March 13, 2006

[19] R. R. Seeley, T. B. Stephens, P. Tate, "Anatomy and Physiology," McGraw-Hill High Education, New York 2006. ISBN-13: 978-0-07-250747-8

[20] http://www.healthatoz.com/healthatoz/Atoz/common/standard/transform.jsp?requestURI =/healthatoz/Atoz/ency/colon_cancer.jsp

[21] http://emice.nci.nih.gov/mouse_models/organ_models/gastro_models

[22] http://en.wikipedia.org/wiki/Stokes_shift

[23] E. A. Johannessen, L. Wang, C. Wyse, D. R. S. Cumming, and J. Cooper, "Biocompatibility of a lab-on-a-pill sensor in artificial gastrointestinal environments," *IEEE Trans. Biomed. Eng.*, 53(11): 2333-2340, 2006.

[24] Zeng H, Weiss A, MacKinnon N, Cline R and MacAulay C 1996 *In vivo* fluorescence spectroscopy of gastrointestinal tract under multiple wavelength excitation *Proc. SPIE* 2926 4–10.

[25] Vo-Dinh, "Biomedical Photonics," CRC Press 2003. ISBN 0-8493-1116-0

[26] B. Mayinger, M. Jordan, T. Horbach, P. Horner, C. Gerlach, S. Mueller, W. Hohenberger, E. Hahn, "Evaluation of in vivo endoscopic autofluorescence spectroscopy in gastric cancer," Gastrointestinal Endoscopy, Volume 59, Issue 2, Pages 191-198

[27] W. Triadifilopoulos, "G. Autofluorescence imaging: have we finally seen the light," *Gastrointest Endosc* 2005; 61:686-8

[28] G. A.Wagnieres, W. M. Star, B. C. Wilson, "In vivo fluorescence spectroscopy and imaging for oncological applications," *Photochem Photobiol* 1998; 68: 603– 632

[29] V. Betz, H. Schneckenburger, H. P. Alleroeder, et al., "Evaluation of changes in the NADH level between carcinogenic and normal tissue samples by use of fluorescence spectroscopy," *SPIE* 1994; 2324: 284– 291

[30] H. Tajiri, M. Kobayashi, K. Izuishi, S. Yoshida, "Fluorescence endoscopy in the gastrointestinal tract," *Dig. Endosc.* 2000; 12 (Suppl.): S28–31

[31] M. Zellweger, D. Goujon, R. Conde, M. Forrer, H. Vander Bergh, and G. Res, "Absolute autofluorescence spectra of human healthy, metaplastic, and early cancerous bronchial tissue in vivo," *Appl. Opt.* 40:3784–3791 (2001)

[32] J. Haringsma, G. N. Tytgat, H. Yano, H. Iishl, M. Tatsuta, T. Ogihara, H. Watanabe, N. Sato, N. Marcon, B. C. Wilson, R.W. Cline, "Autofluorescence endoscopy: feasibility of

detection of GI neoplasms unapparent to white light endoscopy with an evolving technology," *Gastrolntest Endosc* 2001; 53:642-650

[33] S. Anderssonengels, C. Afklinteberg, K. Svanberg, and S. Svanberg, "*In vivo* fluorescence imaging for tissue diagnostics," *Phys. Med. Biol.*, 42: 815–824, 1997. L. W. K. Song, B. C. Wilson, "Endoscopic detection of early upper GI cancers," *Best Pract Res Clin Gastroenterol* 2005; 19:833–856.

[34] K. C. B. Lee, J. Siegel, S. E.D.Webb, S. Leveque-Fort, M. J. Cole, R. Jones, K. Dowling, M. J. Lever and P. M.W. French, "Application of the stretched exponential function to fluorescence lifetime imaging," *Biophys. J.*, 2001, 81, 1265–1274

[35] J. Siegel, D. S. Elson, S. E. D. Webb, K. C. B. Lee, A. Vlandas, G. L. Gambaruto, S. Leveque-Fort, M. J. Lever, P. J. Tadrous and G.W. H. Stamp, "Studying biological tissue with fluorescence lifetime imaging: microscopy, endoscopy and complex decay profiles," *Appl. Opt.*, 2003, 42, 2995–3004

[36] H. Tajir, M. Kobayashi, K. Izuishi, S. Yoshida, "Fluorescence endoscopy in the gastrointestinal tract," *Dig. Endosc.* 2000; 12 (Suppl.): S28–31

[37] H. Tajir, M. Kobayashi, K. Izuishi, S. Yoshida, "Fluorescence endoscopy in the gastrointestinal tract," *Dig. Endosc.* 2000; 12 (Suppl.): S28–31

[38] http://www.endomed.de/gfx/combo.gif

[39] S. Anderssonengels, C. Afklinteberg, K. Svanberg, and S. Svanberg, "*In vivo* fluorescence imaging for tissue diagnostics," *Phys. Med. Biol.*, 42: 815–824, 1997.

[40] M. Hahne, H. E. Adamek, D. Schilling D, J. F. Riemann, "Wireless capsule endoscopy in a patient with obscure occult bleeding," *Endoscopy* 2002; 34:588–590.

[41] D. S. Mishkin, R. Chuttani, J. Croffie et al, "ASGE Technology Status Evaluation Report: wireless capsule endoscopy," Technology Assessment Committee ASGE. *Gastrointest Endosc* 2006; 63: 539–545.

[42] A. Ali, J. M. Santisi, J. Vargo, "Video capsule endoscopy: a voyage beyond the end of the scope," *Clevel Clin J Med* 2004; 71:415–25.

[43] T. Rabenstein, N. Krauss, E. Hahn, P. Konturek, L. Spano, F. Pereira, et al, "Wireless capsule endoscopy: beyond the frontiers of flexible gastrointestinal endoscopy [review]," *Med Sci Monit* 2002; 8:RA128-32.

[44] Q. H. Meng, T. Mei, J. Pu, et al. 2004, "Wireless robotic capsule endoscopy: state-of-the-art and challenges," *In Proc 5th World Congress on Intelligent Control and Automation*, June 2004, Hang Zhou, China, p. 5561–5.

[45] G. Gay, M. Delvaux, J. F. Rey, "The role of video capsule endoscopy in the diagnosis of digestive diseases: a review of current possibilities," *Endoscopy* 2004; 36:913-20.

[46] H. Zeng, A Weiss, N. MacKinnon, R. Cline and C. MacAulay 1996, "*In vivo* fluorescence spectroscopy of gastrointestinal tract under multiple wavelength excitation," *Proc. SPIE* 2926 4–10.

[47] H. Stepp, R. Sroka, and R. Baumgartner, "Fluorescence endoscopy of gastrointestinal diseases: basic principles, techniques, and clinical experience," *Endoscopy* 30, 41, 379–386, 1998

[48] K. Izuishi, H. Tajiri, T. Fuji et al., "The histological basis of detection of adenoma and cancer in the colon by autofluorescence endoscopic imaging," *Endoscopy* 1999, 31:511-16

[49] N. Nakaniwa, A. Namihisa, T. Ogihara, "Newly developed autofluorescence imaging videoscope system for the detection of colonic neoplasms," *Dig. Endosc,* 2005.

[50] G. D. Meron, "The development of the swallowable video capsule (M2A)," *Gastrointest Endosc* 2000; 52:817–819.

[51] G. Gay, M. Delvaux, J. F. Rey, "The role of video capsule endoscopy in the diagnosis of digestive diseases: a review of current possibilities," *Endoscopy* 2004; 36:913-20.

[52] G. Iddan, G. Meron, A. Glukhovsky, P. Swain, "Wireless capsule endoscopy," *Nature* 2000; 405: 417.

[53] M. Yu, "M2A capsule endoscopy. A breakthrough diagnostic tool for small intestine imaging." *Gastroenterol Nurs* 2002; 25: 24–27.

[54] J. Kolars, "Capsule enteroscopy," *Chin J Dig Dis* 2003; 4:49–52.

[55] B. S. Lewis, P. Swain, "Capsule endoscopy in the evaluation of patients with suspected small intestinal bleeding: results of a pilot study," *Gastrointest Endosc* 2002; 56: 349–353.

[56] E. Scapa, H. J. Jacob, S. Lewkowicz, M. Migdal, D. Gat D, A. Glukhovsky, N. Guttman, Z. Fireman, "Initial experience of wireless capsule endoscopy for evaluating occult gastrointestinal bleeding and suspected small bowel pathology," *Amer J Gastroenterol* 2002; 97:2776-2779.

[57] C. Ell, S. Remke, A. May, L. Helou, R. Henrich, G. Mayer, "The first prospective controlled trial comparing wireless capsule endoscopy with push enteroscopy in chronic gastrointestinal bleeding," *Endoscopy* 2002; 34: 685-689.

[58] L. C. Saurin, M. Delvaux, J. L. Gaudin, I. Fassler, J. Villarejo, K. Vahedi, A. Bitoun, J. M. Canard, J. C. Souquet, T. Ponchon, C. Florent, G. Gay, "Diagnostic value of endoscopic capsule in patients with obscure digestive bleeding: Blinded comparison with video pushenteroscopy," *Endoscopy* 2003; 35: 576-584.

[59] R. Eliakim, D. Fischer, A. Suissa, K. Yassin, D. Katz, M. Migdal, N. Guttman, "Wireless capsule video endoscopy is a superior diagnostic tool compared to barium follow through and CT in patients with suspected Crohn's disease," *Europ J Gastroenterol Hepatol* 2003; 15: 363-367.

[60] Z. Fireman, E. Mahajna, E. Broude, M. Shapiro, L. Fich, A. Sternberg, Y. Kopelman, E. Scapa, "Diagnosing small bowel Crohn's disease with wireless capsule endoscopy," *Gut* 2003; 52: 390-392.

[61] J. M. Herrerias, A. Caunedo, M. Rodriguez-Tellez, F. Pellicer, J. M. Herrerias, "Capsule endoscopy in patients with suspected Crohn's disease in negative endoscopy," *Endoscopy* 2003; 35: 1-5.

[62] K. Arshak, E. Jafer, G. Lyons, D. Morris, O. Korostynska, 2004, "A review of low-power wireless sensor microsystems for biomedical capsule diagnosis," In: *Microelectronics International, Emerald Group Publishing Limited*, Vol. 21, No. (3), pp. 8–19.

[63] E. A. Johannessen, L. Wang, C. Wyse, D. R. S. Cumming, and J. Cooper, "Biocompatibility of a lab-on-a-pill sensor in artificial gastrointestinal environments," *IEEE Trans. Biomed. Eng.*, 53(11): 2333-2340, 2006

[64] D. Fischer, R. Schreiber, D. Levi, and R. Eliakim, "Capsule endoscopy: the localization system", *Gastrointestinal Endoscopy Clinics of North America*, 14(2004), pp.25~31.

[65] W. Weitschies, J. Wedmeyer, R. Stehr, and L. Trahms, "Magnetic Markers as a noninvasive tool to monitor gastrointestinal transit", *IEEE Trans on Biomedical Engineering*, vol.41, no.2, 1994, pp.192~195.

[66] S. Abdelsayed, "Power amplifiers and antennas for implantable biomedical transceivers," *M.A.Sc. Thesis* - April 2006.

[67] Chan Y, Meng M Q-H and Wang X 2005, "A prototype design of wireless capsule endoscope," *Proc. IEEE Int. Conf. on Mechatronics & Automation* pp 400–3

[68] N. Faramarzpour, M. M. El-Desouki, M.J. Deen, Q. Fang, S. Shirani, and L.W.C. Liu, "CMOS Imaging for Biomedical Applications," submitted to IEEE Potentials, Nov. 2007

[69] http://www.coemfg.com/downloads/resources/newsletters/2005/0405_News.pdf

[70] D. Litwiller, "CCD vs. CMOS: Maturing Technologies, Maturing Markets," *Photonics Spectra*, August 2005.

[71] http://www.dalsa.com/markets/ccd_vs_cmos.asp

[72] ICX228AL Datasheet – Sony

[73] A. Shoham and J. Bier, "Introduction to Video Compression," *Berkeley Design Technology, Inc. (BDTI)*.

[74] X. Xie, G. Li, X. Chen, X. Li, and Z. Wang , "A Low-Power Digital IC Design Inside the Wireless Endoscopic Capsule," *IEEE Journal of Solid-State Circuit*, 41(11): 2390-2400, 2006.

[75] M. Kfouri, O. Marinov, P. Quevedo, N. Faramarzpour, S. Shirani, L. W-C. Liu, Q. Fang and M. J. Deen, "Toward a Miniaturized Wireless Fluorescence-Based Diagnostic Imaging System," *IEEE Journal of Selected Topics in Quantum Electronics (Special Issue on Biophotonics)*, vol. 14, no. 1, January/February 2008. (Accepted 22 October 2007).

[76] A. L. Polglase, W. J. McLaren, S. A. Skinner et al, "A fluorescence confocal endomicroscope for in vivo microscopy of the upper– and the lower–GI tract," *Gastrointest Endosc* 2005; 62: 686±695.

[77] http://www.olympusfluoview.com/theory/aotfintro.html

[78] N. Faramarzpour, M. J. Deen, S. Shirani and Q. Fang, "Fully Integrated Single Photon Avalanche Diode Detector in Standard CMOS 0.18μm Technology," *IEEE Transactions on Electron Devices*, Vol. 53(3), 8 pages (March 2008).

[79] N. Faramarzpour, M. J. Deen, S. Shirani, Q. Fang, L. W. C. Liu, F. Campos and J.W. Swart, "CMOS Based Active Pixel for Low-Light-Level Detection: Analysis and Measurements," *IEEE Transactions on Electron Devices*, Vol. 54(12), pp. 3229-3237 (December 2007).

[80] N. Faramarzpour, M. J. Deen and S. Shirani, "An Approach to Improve the Signal-to-Noise Ratio of Active Pixel Sensor for Low-Light-Level Applications," *IEEE Transactions on Electron Devices*, Vol. 53(9), pp. 2384-2391 (September 2006).

[81] D. Turgis, R. Puers, "Image compression in video radio transmission for capsule endoscopy", *Sensors and Actuators A: Physical*, vol. 123-124, 23 September 2005, pp. 129-136.

[82] P. Turcza, M. Duplaga, "Low-power image compression for wireless capsule endoscopy," *IEEE IST 2007*, Krakow, Poland, 4–5 May 2007.

[83] H. S. Malvar, A. Hallapuro, M. Karczewicz, L. Kerofsky, "Low- Complexity Transform and Quantization in H.264/AVC," *IEEE Trans. on Circuits and Systems for Video Tech.*, vol. 13, no. 7, July 2003.

[84] ITU-T Rec. H.264 / ISO/IEC 11496-10, "Advanced Video Coding", *Final Committee Draft, Document JVTF100*, December 2002.

[85] M. H. Bakr, K. Wang, M. J. Deen, "Accuracy Improvement of Magnetic Tracking Systems Using ANNs and Space Mapping Modeling," *ACES Conference*, Niagara Falls, March 2008.

[86] N. Faramarzpour, M. J. Deen, and S. Shirani, "Signal and Noise Modeling and Analysis of CMOS Active Pixel Sensors," *Journal of Vacuum Science and Technology A (Special Issue for CSTC 2005)*, Vol. 24(3), pp. 879–882 (May/June 2006).

[87] Y. Ardeshirpour, M. J. Deen and S. Shirani, "Evaluation of CMOS Based Photodetectors for Low-level Light Detection," *Journal of Vacuum Science and Technology A (Special Issue for CSTC 2005)*, Vol. A24 (3), pp. 860–865 (May/June 2006).

[88] http://www.cancerbackup.org.uk/Aboutcancer/Whatiscancer/Whatiscancer/related_faqsQAs/502

[89] N. Ramanujam, "Fluorescence spectroscopy of neoplastic and non-neoplastic tissues," *Neoplasia*. 2000 January; 2(1–2): 89–117

[90] Ralph DaCosta, "Mechanisms of fluorescence endoscopy of the human colon," *M.A.Sc. Thesis*, 2000

[91] G. I. Zonios, R. M. Cothren, J. T. Arendt, J. Wu, J. Van Dam, J. M. Crawford, R. Manoharan, M. S . Feld, "Morphological model of human colon tissue fluorescence," *IEEE Transactions on biomedical engineering*, vol. 43, no. 2, February 1996

[92] http://ezinearticles.com/?Colon-Cancer-Causes-and-Risk-Factors&id=583302

[93] R. Eliakim, "PillCam Colon capsule endoscopy for the detection of colonic pathology," *Endoscopy* 2006; 38: 963-970

[94] T. J. Pfefer, A. Agrawal, R. A. Drezek, "Oblique-incidence illumination and collection for depth-selective fluorescence spectroscopy" *Journal of Biomedical Optics* -- July/August 2005 -- Volume 10, Issue 4

[95] T. Vo-Dinh, "Biomedical photonics handbook," *CRC Press LLC* 2003, ISBN 0-8493-1116-0

[96] R. S. Bradley, M. S. Thorniley, "A review of attenuation correction techniques for tissue fluorescence," *Journal of the Royal Society*, Volume 3, Number 6 / February 22, 2006

[97] M. Zellweger, D. Goujon, R. Conde, M. Forrer, H. van den Bergh, G. Wagnieres, "Absolute autofluorescence spectra of human healthy, metaplastic, and early cancerous bronchial tissue *in vivo*," *Applied Optics*, Vol. 40, No. 22, 1 August 2001

[98] E. Drakaki, M. Makropoulou, A. A. Serafetinides, "In vitro fluorescence measurements in Monte Carlo simulation of laser irradiation propagation in porcine skin tissue," *Lasers in Medical Science*, 2007

[99] J. Mroczka, "Temperature stabilisation of light-emitting diode radiation," *J. Phys. E: Sci. Instrum.* 21 (1988) 306-309

[100] A. T. Buzian, "Optimization of Data for Energy Calculations of Opto-Electronic Systems Based on CCD Matrices", *Proc. of the 3rd Int. Conf.* "Optics-2003", pp. 149-150, St. Petersburg, Russia, 2003. (In Russian).

[101] M. E. Bravo-Zanoguera, J. Rivera-Castillo, M. Vera-Pérez and M. A. R. Carranza, "Use of the Modulation Transfer Function to Measure Quality of Digital Cameras," *Proceedings of the 16th IEEE International Conference on Electronics*

[102] D. Elson, J. Requejo-Isdiro, I. Munro, F. Reavell, J. Siegel, K. Suhling, P. Tadrous, R. Benninger, P. Lanigan, J. McGinty, C. Talbot, B. Treanor, S. Webb, A. Sansidon, A. Wallace, D. Davis, J. Lever, M. Neil, D. Phllips, G. Stamp, P. French, "Time-domain fluorescence lifetime imaging applied to biological tissue," *Photochem. Photobiol. Sci.*, 2004, **3**, 795 – 801

[103] J. Requejo-Isdiro, J. McGinty I. Munro, D. S. Elson, N. P. Galletly, M. J. lever, M. A. A. Neil, G. W. H. Stamp, P. M. W. French, P. A Kellett, J. D. Hares, A. K. L. Dymoke-Bradshaw "High-speed wide-field time—grated endoscopic fluorescence-lifetime imaging," *Optics Letters*, October 1, 2004,/ Vol. 29, No. 19

[104] Q. Fang, T. Papioannou, J. A. Jo, R. Vaitha, K. Shastry, "Time-domain laser-induced fluorescence spectroscopy apparatus for clinical diagnostics," *Review of Scientific Instruments*, Vol. 75, No. 1, Jan. 2004

[105] S. Bellis, J. C. Jackson and A. Mathewson, "Towards a disposable in vivo miniature implantable fluorescence detector," *Proc. of SPIE: Optical Fibers and Sensors for Medical Diagnostics and Treatment Applications VI*, Vol. 6083, 2006

[106] W. A. Qureshi, "Current and future applications of the capsule camera," *Nat Rev Drug Discov* 2004, 3(5), 447–450

[107] R. Volkel, M. Eisner, K.J. Weible, "Miniaturized imaging systems," *Microelectronic Engineering*, 67–68 (2003) 461–472

[108] J. Kling, "Moving diagnostics from the bench to the bedside," *Nature Biotechnology*, vol. 24, no. 8 AUGUST 2006

Appendix A

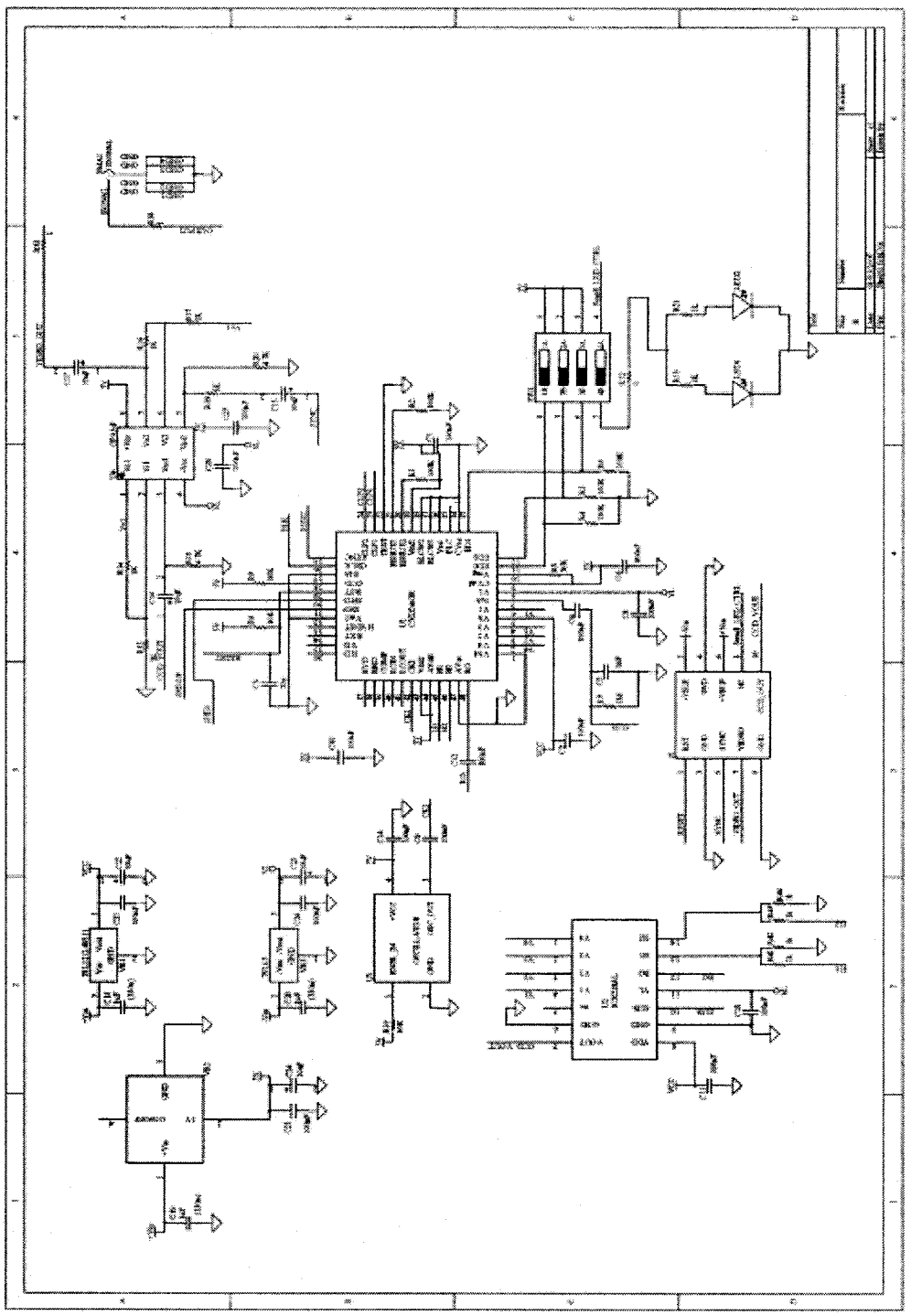

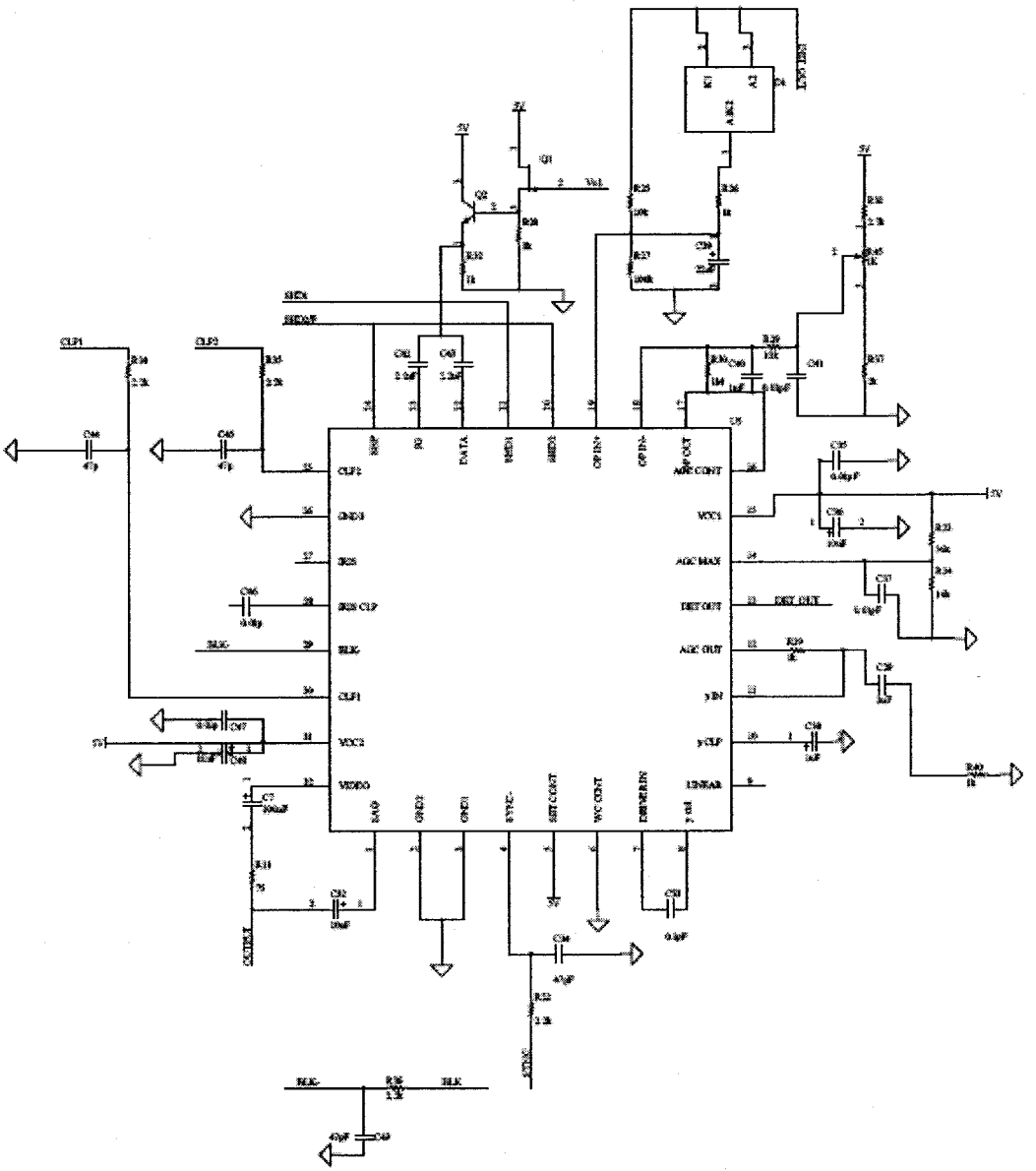

Appendix B

```
%*Converting a circular image to a rectangular image***********
%* Written by: Naser Faramarzpour *********************************
%*Oct. 2007 ***************************************
clc; clear;
%*Getting the image*********************************
P_In = imread('Image2.jpg', 'JPG');
P = P_In;
MN = size(P);
M = MN(1);
N = MN(2);
%*Defining parameters*********************************
A = 1701; %Size of the final image
B = round(A/3.12); %Size of the final image
ShiftX = round(A/4); %Shift in the final image
Cx = 206; %Center of the original image
Cy = 214; %Center of the original image
R = 195; %Radious of decoding in the original image
%*Doing the conversion*********************************
for x = 1 : A
   for y = 1 : B
      % For every point in the final image, find the corresponding
      % point in the original image and export the value
      tetha = (x / A) * 2 * pi;
      r = (y / B) * R;
      xx = r * cos(tetha) + Cx;
      yy = r * sin(tetha) + Cy;
```

```
    NewIm(A - x + 1, y) = (xx-floor(xx)) * (yy - floor(yy)) * P(floor(xx), floor(yy)) +
(xx-floor(xx)) * (ceil(yy) - yy ) * P(floor(xx), ceil(yy)) + (ceil(xx) -xx) * (yy - floor(yy))
* P(ceil(xx), floor(yy)) + (ceil(xx) -xx) * (ceil(yy) - yy ) * P(ceil(xx), ceil(yy));
  end
end
NewIm = NewIm'; %Traspose the final image
%*Perform the shift*********************************
TempIm = NewIm; %Shift the final image
NewIm = [TempIm(:, ShiftX + 1 : A) , TempIm(:, 1 : ShiftX)];
%*Display and write to disk*************************
figure(1); image(P/3); colormap(gray);
figure(2); image(NewIm/3); colormap(gray);
imwrite(NewIm, 'Conv1.bmp', 'bmp');
```